

SPECTROSCOPIC INVESTIGATIONS OF  
METAL CLUSTERS AND METAL CARBONYLS  
IN RARE GAS MATRICES

By

STEPHAN BRUNO HEINRICH BACH

A DISSERTATION PRESENTED TO THE GRADUATE SCHOOL  
OF THE UNIVERSITY OF FLORIDA  
IN PARTIAL FULFILLMENT OF THE REQUIREMENTS FOR  
THE DEGREE OF DOCTOR OF PHILOSOPHY

UNIVERSITY OF FLORIDA

1987

TO MY PARENTS

#### ACKNOWLEDGEMENTS

The author wishes to extend his deepest thanks and appreciation to Professor William Weltner, Jr., whose patience, understanding, encouragement, and professional guidance have made all of this possible. Thanks are also due to Professor Bruce Ault for the initial opportunity to do matrix work and the encouragement to continue on to do graduate work in the field. Thanks need also be given to Professor Weltner's research group, specifically to Dr. Richard Van Zee, whose help and guidance were invaluable in completing this work.

The author also wishes to acknowledge the assistance of the electronics, machine, and glass shops within the Department of Chemistry. They kept the equipment functioning, and fabricated new pieces of apparatus when necessary making it possible to perform the desired experiments. Thanks are also due to Larry Chamusco for many enlightening conversations regarding the present work and also for his help in preparing this work for publication. Thanks are also due to Ngai Wong for his assistance in preparing the final version of this publication.

The author also wishes to acknowledge the support of the National Science Foundation (NSF) for this work as well as Division of Sponsored Research for support in completing the work for this project.

# TABLE OF CONTENTS

	page
ACKNOWLEDGEMENTS .....	iii
LIST OF TABLES .....	vii
LIST OF FIGURES .....	ix
ABSTRACT .....	xiii
CHAPTERS	
I INTRODUCTION .....	1
Matrix Isolation .....	1
Theory of Cluster Formation .....	19
ESR Theory .....	30
The Hyperfine Splitting Effect .....	34
Doublet Sigma Molecules .....	40
The spin Hamiltonian .....	40
The g tensor .....	42
The A tensor .....	46
Randomly oriented molecules .....	49
Molecular parameters and the observed spectrum .....	51
Spin densities .....	56
Quartet Sigma Molecules ( $S=3/2$ ) .....	58
The spin Hamiltonian .....	59
Sextet Sigma Molecules .....	66
The spin Hamiltonian .....	66
Infrared Spectroscopy .....	67
Theory .....	70
Fourier Transform IR Spectroscopy ..	76
II METAL CARBONYLS .....	79
ESR of $VCO_n$ Molecules .....	79
Introduction .....	79
Experimental .....	80
ESR Spectra .....	81
VCO .....	81
$^{51}VCO(A)$ and $^{51}VCO(a)$ in argon ...	81
$^{51}V^{13}CO(A)$ and $^{51}V^{13}CO(a)$ in argon	82
$^{51}VCO(A)$ in neon .....	82
$^{51}VCO(a)$ in krypton .....	88
$^{51}V(^{12}CO)_2$ and $^{51}V(^{13}CO)_2$ in neon	89
$^{51}V(^{12}CO)_3$ and $^{51}V(^{13}CO)_3$ in neon	89

	page
Analysis .....	96
VCO, (A) and (a) .....	96
V(CO) <sub>2</sub> .....	98
V(CO) <sub>3</sub> .....	98
Discussion .....	100
VCO .....	100
V(CO) <sub>2</sub> .....	106
V(CO) <sub>3</sub> .....	107
Conclusion .....	108
Infrared Spectroscopy of First Row	
Transition Metal Carbonyls .....	109
Introduction .....	109
Experimental .....	109
Spectra .....	110
Discussion .....	115
Conclusion .....	119
III    ESR STUDY OF A SILVER SEPTAMER .....	121
Introduction .....	121
Experimental .....	122
ESR Spectra .....	123
Analysis and Discussion .....	129
IV     ESR OF METAL SILICIDES .....	137
ESR of AgSi and MnSi .....	137
Introduction .....	137
Experimental .....	137
ESR Spectra .....	138
AgSi .....	138
MnSi .....	139
Analysis and Discussion .....	139
AgSi .....	139
MnSi .....	145
ESR of Hydrogen-Containing Scandium-	
Silicon Clusters .....	148
Introduction .....	148
Experimental .....	149
ESR Spectra .....	150
HScSiH <sub>n</sub> .....	150
H <sub>2</sub> ScSiH <sub>n</sub> .....	156
Analysis and Discussion .....	157
HScSiH <sub>n</sub> .....	157
H <sub>2</sub> ScSiH <sub>n</sub> .....	166

	page
V CONCLUSION.....	172
REFERENCES .....	178
BIOGRAPHICAL SKETCH .....	187

# LIST OF TABLES

Table	Page
II-1. Observed and calculated line positions (in G) for VCO ( $X^6\Sigma$ ) in conformation (A) in argon at 4 K. $\nu = 9.5596$ GHz.....	83
II-2. Observed and calculated line positions (in G) for VCO ( $X^6\Sigma$ ) in conformation (a) in argon at 4 K. $\nu = 9.5596$ GHz.....	84
II-3. Observed line positions (in G) for VCO ( $X^6\Sigma$ ) in conformation (A) in neon at 4 K. $\nu = 9.5560$ GHz.....	90
II-4. Observed and calculated line positions (in G) for V(CO) <sub>2</sub> ( $X^4\Sigma_g$ ) isolated in neon at 4 K. $\nu = 9.5560$ GHz.....	91
II-5. Calculated and observed line positions and magnetic parameters of the V(CO) <sub>3</sub> molecule in neon matrix at 4 K. $\nu = 9.55498$ GHz.....	92
II-6. Carbonyl Stretching Frequencies for the First Row Transition Metal Carbonyls.....	112
III-1. Calculated and observed ESR lines of <sup>109</sup> Ag <sub>7</sub> in solid neon at 4 K ( $\nu = 9.5338$ GHz) See Figure III-3.....	125
III-2. Magnetic parameters and s-electron spin densities for <sup>109</sup> Ag <sub>7</sub> cluster in its <sup>2</sup> A <sub>2</sub> ground state. (a) .....	131
III-3. Comparison of the magnetic parameters of <sup>107</sup> Ag <sub>7</sub> (this work) with those of Howard, et al.'s <sup>107</sup> Ag <sub>5</sub> cluster.....	135
III-4. Spin densities (s-electron) compared for the <sup>2</sup> A <sub>2</sub> ground states of the Na <sub>7</sub> , K <sub>7</sub> , and Ag <sub>7</sub> .....	136
IV-1. Observed and Calculated Line Positions (in Gauss) for AgSi in argon at 14 K. ( $\nu = 9.380$ GHz).....	140
IV-2. Observed and Calculated Line Positions (in Gauss) for MnSi in argon at 14 K. ( $\nu = 9.380$ GHz).....	141
IV-3. Hyperfine parameters and calculated spin densities for MnSi in argon at 14 K. ( $\nu = 9.380$ GHz).....	147

IV-4.	Observed and calculated line positions (in Gauss) for $\text{HScSiH}_n$ in argon at 14 K. ( $\nu = 9.380$ GHz)...	151
IV-5.	Hyperfine parameters and calculated spin densities for $\text{HScSiH}_n$ in argon at 14 K. ( $\nu = 9.380$ GHz)...	152
IV-6.	Observed and Calculated Line Positions (in Gauss) for $\text{H}_2\text{ScSiH}_n$ , the (A) site, in argon at 14 K. ( $\nu = 9.380$ GHz).....	158
IV-7.	Hyperfine parameters and calculated spin densities for $\text{H}_2\text{ScSiH}_n$ , site (A), in argon at 14 K. ( $\nu = 9.380$ GHz).....	159
IV-8.	Observed and Calculated Line Positions (in Gauss) for $\text{H}_2\text{ScSiH}_n$ , the (a) site, in argon at 14 K. ( $\nu = 9.380$ GHz).....	160
IV-9.	Hyperfine parameters and calculated spin densities for $\text{H}_2\text{ScSiH}_n$ , site (a), in argon at 14 K. ( $\nu = 9.380$ GHz).....	161



# LIST OF FIGURES

Figure	Page
I-1. The furnace flange with copper electrodes and a tantalum cell attached.....	10
I-2. The EPR cavity and deposition surface within the vacuum vessel. The apparatus is capable of cooling the rod to 4 K, because of the liquid helium transfer device (Heli-Tran) on the top.....	11
I-3. The ESR cavity and deposition surface within the vacuum vessel. The apparatus is capable of cooling to 12 K because of the closed cycle helium refrigeration device (Displex) on the top.....	12
I-4. The vacuum vessel, deposition surface, Displex, and furnace assembly for infrared experiments...	13
I-5. Zeeman energy levels of an electron interacting with a spin 1/2 nucleus.....	52
I-6. (a) Absorption and (b) first derivative line-shapes of randomly oriented molecules with axial symmetry and $g_{\perp} < g_{\parallel}$ ; (c) first derivative lineshape of randomly oriented, axially symmetric molecules ( $g_{\perp} < g_{\parallel}$ ), including hyperfine interaction with a spin 1/2 nucleus ( $A_{\perp} < A_{\parallel}$ ).....	53
I-7. Energy levels for a $^4\Sigma$ molecule in a magnetic field; field perpendicular to molecular axis....	63
I-8. Energy levels for a $^4\Sigma$ molecule in a magnetic field; field parallel to molecular axis.....	64
I-9. Resonant fields of a $^4\Sigma$ molecule as a function of the zero field splitting.....	65
I-10. Energy levels for a $^6\Sigma$ molecule in a magnetic field for $\theta = 0^\circ, 30^\circ, 60^\circ$ , and $90^\circ$ .....	68
I-11. Resonant fields of a $^6\Sigma$ molecule as a function of the zero field splitting.....	69

- II-1. ESR spectrum of an unannealed matrix at 4 K containing  $^{51}\text{VCO(A)}$ , with hfs of about 100 G, and  $^{51}\text{VCO(a)}$ , with hfs of about 60 G. For the conformation (A) two perpendicular lines and an off principle axis line are shown.  $\nu = 9.5585 \text{ GHz}$ ..... 85
- II-2. ESR spectrum of an annealed argon matrix at 4 K containing only  $^{51}\text{VCO}$  in conformation (a). Two perpendicular lines and off principal axis line are shown.  $\nu = 9.5585 \text{ GHz}$ ..... 86
- II-3. ESR spectrum of the perpendicular  $xy_1$  line of  $^{51}\text{V}^{13}\text{CO}$  in conformation (a) in an argon matrix at 4 K.  $\nu = 9.5531 \text{ GHz}$ ..... 87
- II-4. ESR lines in a neon matrix at 4 K attributed to  $^{51}\text{VCO}$  in conformation (A).  $\nu = 9.5560 \text{ GHz}$ ..... 93
- II-5. ESR lines in a neon matrix at 4 K attributed to  $^{51}\text{V(CO)}_2$ .  $\nu = 9.5560 \text{ GHz}$ ..... 94
- II-6. (Top) ESR spectrum near  $g=2$  in a neon matrix at 4 K attributed to an axial  $^{51}\text{V(CO)}_3$  molecule.  $\nu = 9.5584 \text{ GHz}$ .  
(Bottom) Simulated spectrum using  $g$ ,  $A(^{51}\text{V})$  parameters and linewidths given in the text.... 95
- II-7. Molecular orbital scheme for the  $^6\Sigma \text{ VCO}$  molecule (modeled after Fig. 5-43 in DeKock and Gray(84))..... 101
- II-8. Infrared spectrum of  $\text{CrCO}$  using both  $^{12}\text{CO}$  and  $^{13}\text{CO}$  in argon. The top trace has a 1:200  $\text{CO/Ar}$  concentration and the bottom has a 1:1:200  $^{12}\text{CO}/^{13}\text{CO/Ar}$  concentration..... 113
- II-9. Infrared spectrum of  $\text{Mn}$  and  $\text{CO}$  codeposited into an argon matrix. The bottom trace is after annealing the matrix to about 30 K and cooling back down to 14 K..... 114
- II-10. Plot of the  $\text{CO}$  stretching frequencies in the first row transition metal monocarbonyl molecules  $\text{MCO}$  (circled points are tentative). Also shown is the variation of the energy of promotion corresponding to  $4s^2 3d^{n-2}$  to  $4s^1 3d^{n-1}$ , where  $n$  is the number of valence electrons(91). 117

- III-1. The pentagonal bipyramid structure ascribed to  $\text{Ag}_7$  in its  ${}^2\text{A}_2$  ground state. It has  $\text{D}_{5h}$  symmetry with two equivalent atoms along the axis and five equivalent atoms in the horizontal plane.. 126
- III-2. The ESR spectrum of  ${}^{109}\text{Ag}$  in solid neon matrix at 4 K ( $\nu = 9.5338$  GHz). The top trace is the overall spectrum, and the bottom traces are expansions of the three regions of interest after annealing. Notice the large intensity of the silver atom lines at 3000 G before annealing..... 127
- III-3. The ESR spectrum of  ${}^{109}\text{Ag}_7$  in a solid neon matrix at 4 K ( $\nu = 9.5338$  GHz). The fields indicated are the positions of the four hyperfine lines corresponding to  $|J, M_J\rangle = |1, 1\rangle, |1, 0\rangle, |0, 0\rangle$ , and  $|1, 1\rangle$  (see Table III-1). The spacing within each of the four 6-line patterns is uniformly 8.7 G. The few extra lines in the background of the lines centered at 3006 G are due to residual  ${}^{109}\text{Ag}$  atom signals..... 128
- IV-1. The ESR spectrum of  $\text{AgSi}$  is an argon matrix at 12 K. The line positions of the impurities ( $\text{CH}_3$  and  $\text{SiH}_3$ ) are noted.  $\nu = 9.380$  GHz..... 142
- IV-2. The ESR spectrum of  $\text{MnSi}$  in an argon matrix at 12 K.  $\nu = 9.380$  GHz..... 143
- IV-3. The ESR spectrum of  $\text{Sc}$  codeposited with  $\text{Si}$  into an argon matrix at 12 K. The eight sets of doublets are shown for  $\text{HScSiH}_n$ .  $\nu = 9.380$  GHz.. 153
- IV-4. The  $m_I = -1/2$  and  $-3/2$  transitions for  $\text{HScSiH}_n$  at 12 K. Two different rod orientations are shown. The top is with the rod parallel to the field and the bottom trace is for the rod perpendicular to the field.  $\nu = 9.380$  GHz..... 154
- IV-5. The ESR spectrum in the  $g=2$  region after annealing a matrix containing both  $\text{Si}$  and  $\text{Sc}$  ( $\nu = 9.380$  GHz). The doublets due to  $\text{HScSiH}_n$  have disappeared. The only remaining lines are due to impurities and  $\text{H}_2\text{ScSiH}_n$  (noted)..... 155

- IV-6. The ESR spectrum ( $m_I=7/2$  and  $5/2$ ) for  $H_2ScSiH_n$  in argon at 12 K after annealing to about 30 K. The top trace is for the rod perpendicular to the field and the bottom trace is for the rod parallel to the field.  $\nu = 9.380$  GHz..... 162
- IV-7. Same as Figure IV-6 except the  $m_I=3/2$  and  $-3/2$  transitions are shown..... 163
- IV-8. Same as Figure IV-6 except the  $m_I=1/2$  transition is shown..... 164
- IV-9. Same as Figure IV-6 except the  $m_I=-5/2$  and  $-7/2$  transitions are shown..... 165

Abstract of Dissertation Presented to the  
Graduate School of the University of Florida  
in Partial Fulfillment of the Requirements for  
the Degree of Doctor of Philosophy

SPECTROSCOPIC INVESTIGATIONS OF METAL CLUSTERS AND  
METAL CARBONYLS IN RARE GAS MATRICES

By

STEPHAN BRUNO HEINRICH BACH

December, 1987

Chairman: Professor William Weltner, Jr.  
Major Department: Chemistry

Three vanadium carbonyls were formed by codeposition of vanadium vapor and small amounts of  $^{12}\text{CO}$  and  $^{13}\text{CO}$  in neon, argon, and krypton. Two of the species were high spin ( $S > 1$ ) molecules. For  $\text{VCO}$  ( $S = 5/2$ ) two conformations of almost equal stability were trapped in various matrices. The dicarbonyl was also observed and found to have an  $S = 3/2$  ground state and a zero field splitting parameter  $|D| = 0.30 \text{ cm}^{-1}$ . Also observed only in a neon matrix was  $\text{V}(\text{CO})_3$ . The ground state for this axial molecule is either  $^2\text{A}'_1$  or  $^2\text{A}_1$  depending on whether it has planar  $\text{D}_{3h}$  or pyramidal  $\text{C}_{3v}$  symmetry.

Other first row transition metal carbonyls were studied using Fourier transform infrared spectroscopy. When chromium and CO were codeposited into an argon matrix, a molecule was formed with CO for which a stretching frequency at  $1977 \text{ cm}^{-1}$

was observed. An attempt is made to relate the bonding of first row transition metal monocarbonyl molecules to the observed infrared CO stretching frequencies of these molecules.

A cluster of seven silver atoms was produced when the 109 isotope of silver was vaporized and deposited into a neon matrix and analyzed using electron spin resonance spectroscopy. The product signals were strongest after the matrix had been annealed. From the observed hyperfine splittings it was determined that the cluster has a pentagonal bipyramidal ( $D_{5h}$  symmetry) structure with a  $^2A_2''$  ground state. Its properties are shown to be similar to those found by other workers for the Group IA alkali metal septamers.

Pure metal clusters were isolated when silicon was codeposited with silver and manganese. Silver silicide was isolated in an argon matrix and found to have a doublet ground state. Manganese silicide was observed in both argon and neon matrices and found to have an  $S=3/2$  ground state. Hyperfine parameters have been determined for both species. Silicon-containing scandium hydrides have also been observed in argon matrices upon codeposition of silicon and scandium vapor. The two species identified contained one and two hydrogens attached to the scandium. Both molecules were found to have doublet ground states. Hyperfine parameters were determined for both species.

## CHAPTER I INTRODUCTION

### Matrix Isolation

Matrix isolated metal clusters and metal carbonyls can be studied in a variety of ways and are thought to aid in the understanding of metal catalysts. The methods of studying these compounds are as diverse as the compounds themselves, varying from optical methods such as infrared, Raman, uv-visible, to electron spin resonance and magnetic circular dichroism spectroscopies which probe the cluster for its magnetic and electronic properties. Using these varied techniques, it is possible to determine the electronic structure of the metal clusters. This information can then be tied together with theoretical calculations to elucidate the properties of the metal cluster.

Before the advent of matrix isolation, the study of metal clusters was carried out either in the gas phase or in solutions. Matrix isolation was developed in the mid-1950's by George Pimentel and coworkers (1). The technique was developed as a means of studying highly unstable reaction intermediates which would, under standard conditions, be too short lived to be observed. It has since been applied to a wide variety of systems which have one thing in common: The species of interest are too unstable to be studied under normal laboratory conditions.

Several things are required in order to do matrix isolation. First, the experiments require a high vacuum environment. This means a pressure below  $1 \times 10^{-6}$  torr must be maintained in order to minimize the amount of atmospheric impurities that will be trapped within the matrix. This type of a vacuum is usually achieved using an oil diffusion and a mechanical pump with a liquid nitrogen cold trap.

Matrix isolation experiments are usually carried out between 4 and 15 K. This temperature range can be achieved by one of two methods depending upon the desired minimum temperature. Using commercially available closed cycle helium refrigerators is one way to cool the deposition surface to the desired temperature. The only drawback of this system is that the minimum temperature the refrigerator can achieve lies at about 12 K (Recent advances have produced a closed cycle system which is capable of 4 K, but their cost is prohibitive). An alternative to this method is to simply use liquid helium to cool the deposition surface. This can be done by using either a dewar or a commercially available transfer device such as the Air Products Heli-tran. These devices can achieve a low temperature in the neighborhood of 4 K.

The final consideration in setting up this type of experiment is the substrate on which to deposit the matrix. Types of material for this surface range from CsI (or other suitable alkali halide salts), to sapphire, or to polished



metal surfaces. Factors to be considered when choosing the substrate depend on the type of experiment being done, but all such solids must have high thermal conductivity. Also, optical properties must be considered when doing absorption or emission studies, whereas magnetic susceptibilities are of concern in ESR and MCD. Obviously, the purity of the solid substrate is important since even small amounts of some impurities can cause strong absorptions or magnetic perturbations.

The term "matrix isolation" comes about because the molecules of interest are trapped in a matrix of inert material, usually a noble gas such as neon, argon, krypton, or nitrogen. The trapping site is usually a substitutional site or an imperfection in the crystalline structure of the solid gas, and the trapped species, seeing only inert nearest neighbors, are isolated and can not react further.

Trapping the metal atom in the matrix is fairly straightforward once the method of atomizing the metal has been determined. But, a problem arises in producing metal di, tri, and higher-order species. It is unusual to simply deposit a matrix and get a species other than a monomer or a dimer. In order to get these higher order species of interest several techniques can be used.

The most common technique used is to simply anneal the matrix. Annealing involves depositing the matrix, and then warming it. The amount that the matrix is warmed depends on

two things, the matrix gas being used and the trapped species. A matrix can usually be annealed up to a temperature equal to approximately one third that of its melting point without solid state diffusion occurring. The problem that occasionally arises is that once the temperature of the matrix has begun to rise, it is possible for some reactions to occur due to diffusion of smaller atoms or molecules that are trapped. This might induce an exothermic reaction, causing the matrix to heat more rapidly than intended, exceeding the capability of the cooling system to dissipate the heat produced. The pressure then rises and rapid evaporation of the matrix occurs (2).

Photoaggregation is another method employed to produce metal clusters after the matrix has been deposited. This method usually involves photo-excitation of the metal which causes local warming of the matrix as the metal atom dissipates the excess energy. This partial warming loosens the matrix around the metal atom allowing it to diffuse and possibly interact with other metal atoms in the vicinity. This method has been used to successfully produce silver clusters by Ozin and coworkers (3).

Using different matrix gases can also give differing results as to the size of the metal molecules formed. These differences arise for several reasons. The most obvious is that the different solid "gases" will have different sized substitutional and interstitial spaces. Another consideration

is the rate at which the matrix freezes. This will depend not only on the capacity of the cooling system to dissipate the excess energy, but also on the freezing point of the gas. It is important to remember that the amount of energy that the cooling system can dissipate depends on the temperature to which it must cool the deposition surface. The Displex or Helium dewar can dissipate substantially more energy at a higher temperature, such as that necessary to freeze krypton (melting point 140 K) rather than neon, which freezes at about 20 K. This difference in freezing rates will allow a varying amount of time for the atoms to move around on the surface of the matrix which is in a semi-liquid state. The longer the atoms can move on the surface of the matrix, the greater the chance for the aggregation and formation of small metal molecules (2). The kinetics of cluster formation will be discussed later in greater detail.

In the last 30 years a wide variety of methods has been applied to the study of molecules and atoms which have been trapped in matrices. One technique used to obtain data is resonance Raman spectroscopy. In this case a polished aluminum surface is used as the deposition surface for the matrix. The metal is vaporized by electrically heating a metal ribbon filament and codepositing the vapor with the matrix gas. The aluminum deposition surface is contained in a pyrex or quartz bell to facilitate viewing and irradiating the matrix with an argon laser (4).

In this type of an experiment one can limit the amount of metal entering the matrix to half of the aluminum surface, leaving the other half virtually free of metal atoms. It is then possible to probe various parts of the matrix to determine the distribution of metal in the matrix (Moskovits purposely screened part of the metal stream so as to achieve a concentration gradient within the matrix) (4). From resonance Raman experiments it is possible to determine the vibrational frequency (at the equilibrium internuclear separation ( $\omega_e$ )), and the first order anharmonicity constant ( $\omega_e x_e$ ). Typical molecules which have been investigated using this technique are  $\text{Fe}_2$ ,  $\text{NiFe}$ ,  $\text{V}_2$ ,  $\text{Ti}_2$ ,  $\text{Ni}_3$ ,  $\text{Sc}_2$ ,  $\text{Sc}_3$ , and  $\text{Mn}_2$ . Another common way of determining the presence of metal in the matrix is the color of the matrix. Most matrices containing metal atoms or molecules will have a characteristic color (4).

Magnetic circular dichroism (MCD) spectroscopy is another technique which has been used to study matrix isolated metal clusters. MCD is the differential absorbance of left and right circularly polarized light by a sample subjected to a magnetic field parallel to the direction of propagation of the incident radiation. A one inch diameter  $\text{CaF}_2$  deposition window is used, and the magnet (.55T) is rolled up around the vacuum shroud surrounding the deposition surface. Before an MCD spectrum is taken, a double beam absorption spectrum is usually taken, the reference beam

being routed around the vacuum shroud through the use of mirrors, in order to maximize the signal to noise ratio of the MCD spectrum. The optimum absorbance value has been found to be 0.87, and deposition times are controlled accordingly (5). The information gained from this type of experiment is very useful in assigning the electronic ground state of the species under study. The MCD technique also has the advantage of being able to assign spin-forbidden electronic transitions. Properties of excited electronic states have also been investigated utilizing MCD (5).

Optical absorption spectroscopy has also been done on matrix isolated samples; for example,  $\text{PtO}$  and  $\text{Pt}_2$  have been studied in argon and krypton. Atomic platinum lines were also observed. A KBr cold surface was used as a deposition surface. A hollow cathode arrangement was used to vaporize platinum wire, which was being used as the anode. This was then put into a stainless steel vacuum vessel equipped with an optical pathway. Deposition times were varied from a few minutes for Pt up to two hours to make  $\text{PtO}$  and  $\text{Pt}_2$ . The absorption spectrum was then taken (6).

The present work has utilized two types of analysis, namely electron spin resonance spectroscopy and Fourier transform infrared spectroscopy. When doing ESR, two types of deposition surfaces are usually used, either a copper or a single-crystal sapphire rod. Both are magnetically inert, and they, like other deposition surfaces, have good thermal

transport properties. In order to do ESR the sample has to be placed into a homogeneous magnetic field. This is usually accomplished by mounting the vacuum shroud surrounding the deposition surface on rails. The matrix can then be deposited outside of the confines of the magnet's pole faces (7,8).

In order to perform a typical matrix isolation experiment using electron spin resonance to analyze the matrix, several pieces of specialized equipment are necessary. Measurements on the matrix take place between the pole faces of an electromagnet. This inherently restricts the size of the vacuum chamber and deposition surface. The set-up used is typically in two parts. One half contains the metal deposition set-up or "furnace" (Figure I-1). The second part contains the deposition surface and the ESR cavity (Figures I-2 and I-3). Figure I-2 shows the system configured with the Heli-Tran liquid helium transfer device from Air Products, and Figure I-3 has the set-up configured with the Air Products Displex closed cycle helium refrigeration system. The two halves are separated by a set of gate valves so that they can be disconnected from each other without compromising the high vacuum conditions maintained in each. Once separated the rod is lowered into the ESR cavity with the aid of pneumatic pistons. After the rod is in the cavity, the half containing the ESR cavity and

the rod is rolled into the magnet so that the ESR cavity and rod are located between the pole faces of the magnet.

Infrared work can also be done in a fashion similar to that used for ESR. The primary difference is that the deposition surface is usually CsI or quartz because of their optical properties (No significant absorptions between 4000 and 200 wavenumbers). For this type of work the vacuum shroud containing the deposition window usually sits in the sample compartment of the infrared spectrometer aligned so that the sample beam passes through the deposition window.

The apparatus for doing infrared experiments has some similarities to that used for the ESR experiments. There is a furnace and a dewar, and gate valves separating the two (Figure I-4). But a much smaller vacuum shroud can be used because only a deposition window is contained inside of it. It is important that the infrared beam passes into the vacuum vessel, through the deposition surface (in most cases), and back out again so that the beam can reach the detector, which means that the matrix, as well as the windows through which the infrared beam must pass, needs to be able to transmit radiation in the infrared region. The deposition window usually remains in the infrared instrument for the entire experiment, which then enables one to follow the deposition of the matrix.

Several options are available to vaporize the metal sample. The usual method is resistive heating. The metal is

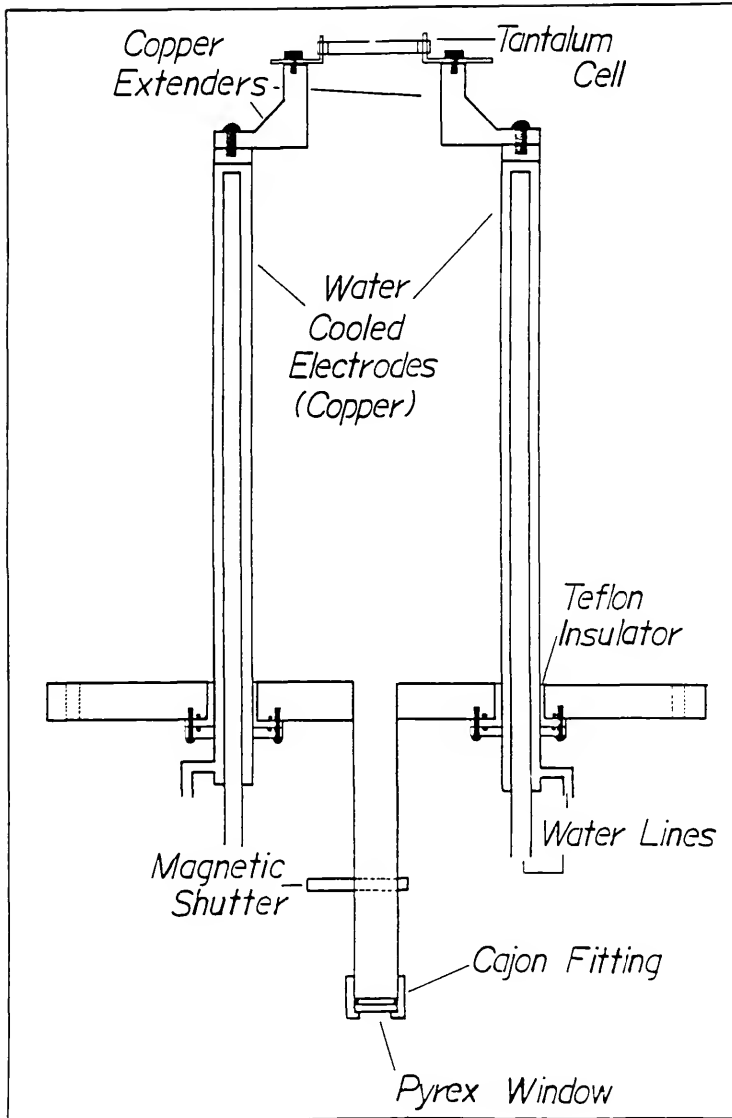


Figure I-1. The furnace flange with copper electrodes and a tantalum cell attached.



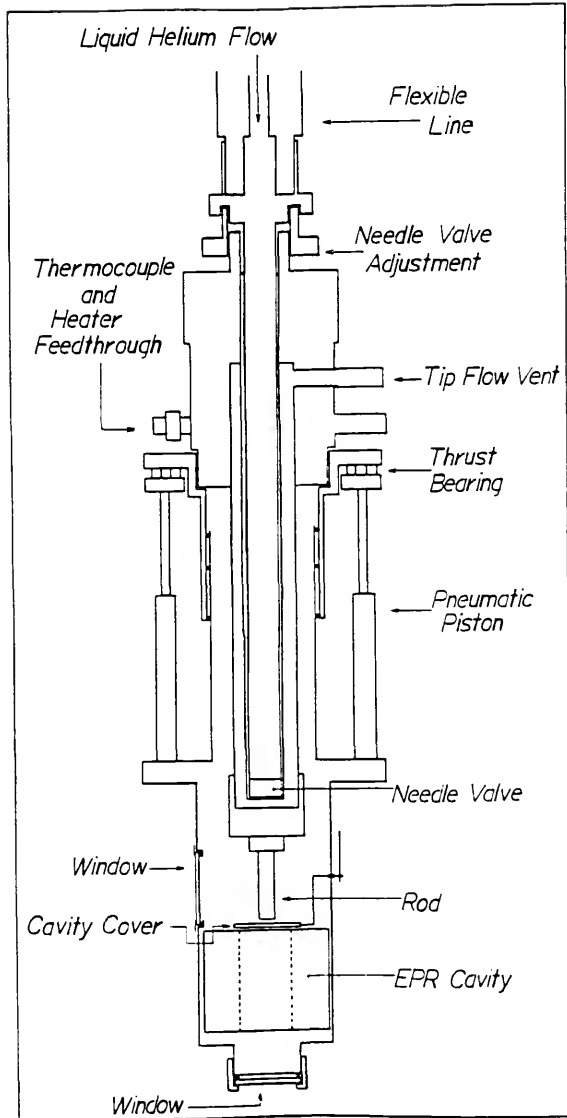


Figure I-2. The EPR cavity and deposition surface within the vacuum vessel. The apparatus is capable of cooling the rod to 4 K, because of the liquid helium transfer device (Heli-Tran) on the top.

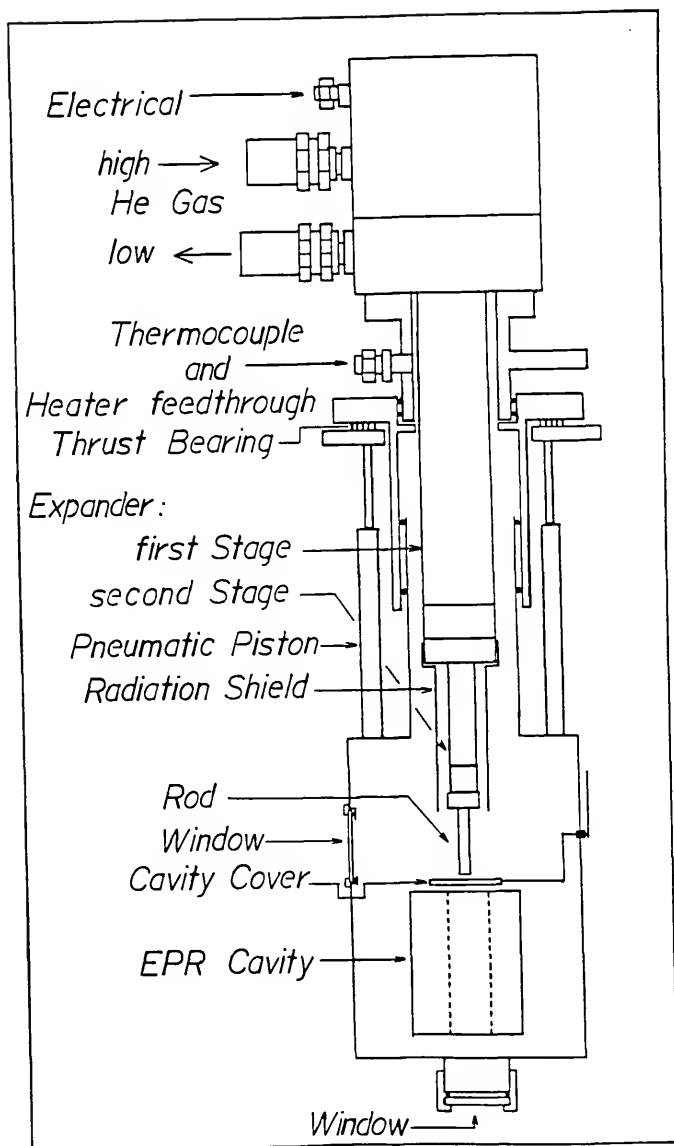


Figure I-3. The ESR cavity and deposition surface within the vacuum vessel. The apparatus is capable of cooling to 12 K because of the closed cycle helium refrigeration device (Displex) on the top.

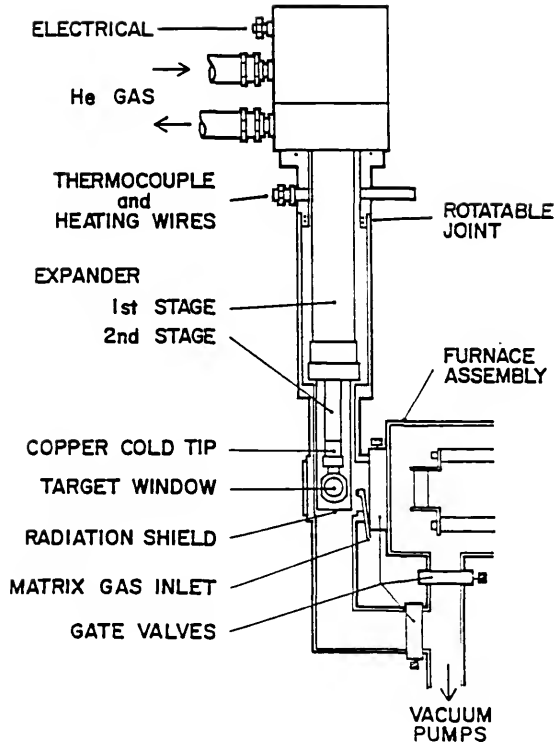


Figure I-4. The vacuum vessel, deposition surface, Displex, and furnace assembly for infrared experiments.

placed into a cell made of a high melting metal with good electrical properties. (Mixed metal species may sometimes arise in high temperature work because a significant portion of the cell may also vaporize with the sample.) Heating in this fashion, it is possible to achieve temperatures in excess of 2000 °C. An alternative method is to put the sample cell into an inductive heating coil; in this manner, comparable temperatures can usually be attained. The temperature of the furnace is estimated by using an optical pyrometer; more accurate measurements require an estimate of the emissivity of the hot surface.

The determination of what has been trapped can sometimes be simple or, at other times, rather complex. In the case of  $\text{Sc}_2$  it was rather straightforward. The ESR spectrum was measured by Knight and co-workers (9). Since the Sc nucleus has a spin of  $7/2$  ( $I=7/2$ ), the hyperfine structure observed identified the trapped species. A resonance Raman experiment determined the vibrational frequency of the ground state molecule to be  $238.9 \text{ cm}^{-1}$  (10). From this information it was then possible to determine whether a chemical bond exists between the trapped species. In the case of discandium, a single bond and not van der Waals forces binds the two atoms (11).

A more controversial diatomic molecule, dichromium, is not quite as straightforward; it has a singlet ground state and is therefore not observable using ESR. Theoretical

studies of  $\text{Cr}_2$  indicate a variety of bonding configurations. A resonance Raman study has examined both di and tri chromium (10). For the dichromium species it was first necessary to decide which of the spectral features belonged to dichromium and which belonged to trichromium. This was done in two ways. The change in relative intensities of the bands was observed as the concentration was varied (the assumption being that a more concentrated matrix would favor a larger cluster), and a high resolution scan of one of the observed lines was fit with the calculated isotopic fine-structure spectrum, assuming the carrier of the line to be  $\text{Cr}_2$ . The vibrational frequency could then be determined from the spectra, and from this a force constant indicating the strength of bonding. The results from the experiment indicate that multiple bonding does exist ( $k=2.80 \text{ mdyne/\AA}$ ). (Dicopper with a single bond has a  $k=1.3 \text{ mdyne/\AA}$ .) The extent of the multiple bonding can not be determined from these results (11).

Divanadium has also been investigated using the resonance Raman technique to yield an equilibrium vibrational constant of  $537.5 \text{ cm}^{-1}$  (4), but mass spectrometric data were needed to complete the picture. It was determined that the dissociation energy for divanadium is about 1.85 eV (11). From spectroscopy done in a two-photon-ionization mass selective experiment, on a supersonically expanded metal beam, a value of  $1.76 \text{ \AA}$  for the equilibrium distance was

measured (12). The short bond distance coupled with a high vibrational frequency shows that the molecule is strongly bonded by 3d electrons (11).

Higher order metal clusters such as  $Mn_5$  have also been trapped, and ESR spectra measured in matrices. In this case several equally spaced (300 G) lines were observed in the spectrum. From the number of these fine-structure lines it was determined that the molecule has 25 unpaired electrons (Hyperfine splittings were not resolved.). On this basis it is possible to postulate the cluster size. Smaller clusters are improbable on the basis of  $S=25/2$ . It is also important to remember that the larger clusters are unlikely to form in the matrix initially. The structure of  $Mn_5$  is thought to be pentagonal with single bonds between each of the manganese atoms and with each of the atoms having five unpaired electrons. The ESR spectrum indicates that all of the manganese atoms in the molecule are equivalent; a pentagonal structure fulfills this requirement (13).

A similar problem arises in the case of doing a high concentration scandium experiment. In this case it is thought that a molecule with 13 Sc atoms is made. The ESR spectrum contains over 60 lines in the  $g=2$  region of the spectrum, which usually indicates one unpaired electron in the molecule. Because the intensity of the lines drops off at the fringes of the hyperfine structure, it is difficult to ascertain exactly how many lines exist. With the observed

lines there are at least nine Sc atoms in the molecule. The  $\text{Sc}_{13}$  molecule seems likely because of theoretical calculations done on transition metal clusters with 13 atoms. A single Self-Consistent Field X $\alpha$ -Scattered wave calculation has been done for  $\text{Sc}_{13}$  giving a single unpaired electron, in agreement with the ESR results (14).

Matrix isolation is more of a technique than a method of analysis. It can be used in conjunction with various analytical tools which then can be used to determine the composition and structure of the trapped compound. It is important to use some forethought in choosing the method of analyzing the trapped molecule because the method chosen will determine what information can be obtained from the experiment. Data from various methods will tend to complement each other. For example, if the molecule of interest does not contain an unpaired electron, then it would not be worthwhile to do ESR since this method requires the presence of at least one unpaired electron in order to produce a spectrum. Analyzing the molecule for its vibrational structure by using resonance Raman or infrared spectroscopy will only give the molecule's vibrational modes. From these modes it may or may not be possible to determine the molecule's structure, depending on the complexity of the molecule and the degeneracy of the modes. Another problem, when dealing with clusters, is that it is sometimes difficult to determine the size of the cluster from the observed

spectra. Also, once the molecule is trapped, its trapping environment may not be uniform throughout the matrix. This will cause splittings in the observed lines of the spectrum due to different trapping sites. The trapping site may also cause a lowering of the observed point group of the molecule, which will cause lines to split because they are no longer degenerate. Matrix isolation is a useful tool which aids in determining the structure of unstable species, but it is best used in conjunction with other techniques if accurate structures are to be determined.

As can be seen from what other workers have done, matrix isolation can be used to trap very reactive and also very interesting species. We set out to use this technique to further elucidate the properties of transition metals and transition metal carbonyls. Following this line of interest has lead us to study various first row transition-metal carbonyls using both ESR and FTIR. We continued our work with transition metals by investigating the group IB metals and attempted to produce larger clusters. We finally turned our attention to the first row transition-metal silicides. Our hope in these endeavors was to produce various metal containing species in order to determine structure and to obtain possible enlightenment as to the reaction processes occurring to form them.

Producing these metal species as well as analyzing the resultant spectra tends to be a rather complicated process.



A review of the kinetics of cluster formation is very helpful in pointing out and understanding some of the processes involved in producing these exotic species. The analysis of the ESR spectra can sometimes be rather simple when one is dealing with only a few lines. But when the trapped species produces many lines, the analysis rapidly becomes complicated and a review of relevant theory becomes mandatory. A brief review of infrared spectroscopy will also be presented.

### Theory of Cluster Formation

In recent years the area of metal cluster chemistry has become rather active. The main reason behind this is the hope that the metal cluster will be useful in the investigation of the chemistry that occurs at metal surfaces. This interest has lead to two major thrusts, one involving the reproducible production of these clusters and the other concerning itself with the mechanisms involved in the evolution of the clusters. Both of these areas are now being actively pursued by various workers (15-19).

Experimentally, the production of these clusters and their identification have proven extremely challenging. Three primary methods of vaporizing the metal exist, laser vaporization, resistively heating of a cell containing the metal of interest, or heating a wire made of the appropriate metal. Of these the most successful has been the use of lasers. A major problem in determining the kinetics involved

in cluster formation is the reproducibility of the distribution of cluster sizes from experiment to experiment. Several groups have had some success at this and even have begun to react these metal clusters with various types of reactants (20,21).

In developing a general mean-field kinetic model of cluster formation one must look first at the aggregation process in the thermal vaporization source. Second, a method needs to be found to calculate probabilities for cluster formation taking into account atom-atom collisions to form dimers as well as collisions between clusters. This would have to include not only aggregation but also cluster fragmentation from collisions, structural stabilities of certain clusters, how energy is dissipated upon collision, and possible transition states of the clusters. It should also be able to explain the cluster distribution found in mass spectra of these systems.

The metal clusters are produced by laser vaporization in a supersonic nozzle source and then allowed to enter a fast-flow reactor, before being mass analyzed. The source of the metal of interest is a rod about 0.63 cm in diameter. The rod is placed in the high pressure side of a pulsed supersonic nozzle, operating with a ten atmosphere back pressure. The frequency doubled output of a Q-switched Nd:YAG laser (30 to 40 mJ/pulse, 6 ns pulse duration) is focused to a spot approximately 0.1 cm in diameter on the

target rod, and fired at the time of maximum density in the helium carrier gas pulse. The target rod is continually rotated and translated, thus preventing the formation of deep pits, which would otherwise result in erratic fluctuations in the sizes of the metal clusters. The helium-metal vapor mixture then flows at near sonic velocity through a cluster-formation and thermalization channel, 0.2 cm in diameter and 1.8 cm in length, before expanding into a 1 cm diameter, 10 cm long reaction tube. Effectively, all cluster formation in such a nozzle source is accomplished in the thermalization channel since expansion into the 1 cm diameter reaction tube produces a 25 fold decrease in density of both the metal vapor and the helium buffer gas (20).

The reaction tube has four needles which can be used to inject various reactants into the flowing mixture of carrier gas and metal. Following the reaction tube, the reaction gas mixture is allowed to expand freely into a large vacuum chamber. A molecular beam is extracted from the resulting supersonic free jet by a conical skimmer and collimated by passage through a second skimmer. The resulting well-collimated, collisionless beam is passed, without obstruction, through the ionization region of a time-of-flight mass spectrometer (TOFMS). Detection of the metal clusters and their reaction products is accomplished by direct one photon ionization in the extraction region of the TOFMS (20).

With the advent of this type of a device, it is now possible to produce metal clusters under relatively controlled conditions with a fairly reproducible distribution of cluster sizes. The reproducibility of cluster size distribution between experiments has made it possible to compare the results to kinetic studies dealing with the formation of metal clusters. The kinetic analysis of the clusters has been able to explain why some cluster sizes are favored, to suggest the relative importance of kinetic and thermodynamic effects, and to shed some light on the possible influence of ionization of the clusters.

The kinetic theory applicable is that of aggregation and nucleation. The mean-field rate equations governing the aggregation of particles developed by Smoluchowski (22) are

$$(I-1) \quad \dot{X}_i = \sum_{j=1}^{i-1} K_{ji-1} X_j X_{i-1} - \sum_{j=1}^N 2K_{ij} X_i X_j \quad i = 1, \dots, N$$

In equation I-1,  $X_i$  denotes the concentration of clusters of size  $i$ . The aggregation kernel,  $K_{ij}$ , determines the time-dependent aggregation probability. The first term on the right hand side of the equation describes the increase in concentration of clusters size  $i$  due to the fusion of two clusters size  $j$  and  $i-j$ . The second term describes the reduction of clusters size  $i$  due to the formation of larger clusters. The equation must be generalized in order that the

neutral-positive, neutral-negative, and positive-negative cluster fusions are included because the vaporization process will produce some ions. But, since the electrons and the ions are attracted by long range Coulomb forces, the recombination processes are very fast, leading to a population of neutral atoms that is much larger than the population of ions. Therefore, the probability for positive-negative cluster fusion is much smaller than that of neutral-positive and neutral-negative cluster fusion and can be neglected (15).

The terms due to the formation of positive clusters are

$$(I-2) \quad \dot{X}_i^0 = \dot{X}_i - \sum_{j=1}^N K_{ij}^{0+} X_i^0 X_j^+$$

and

$$(I-3) \quad \dot{X}_i^+ = \sum_{j=1}^{i-1} K_{ji}^{0+} X_j^0 X_{i-j}^+ - \sum_{j=1}^N K_{ji}^{0+} X_j^0 X_i^+ \quad i = 1, \dots, N$$

where  $\dot{X}_i$  is defined by the right hand side of equation I-1 and  $\dot{X}_i^0$  and  $\dot{X}_i^+$  denote the concentration of the neutral and positively charged clusters, respectively. The kernels  $K_{ij}$  and  $K_{ij}^{0+}$  describe the neutral-neutral and neutral-positive aggregation probabilities. Analogous terms are introduced due to the presence of the negatively charged clusters (15).

During cluster growth, there is also the possibility of charge transfer between the charged and the neutral clusters without the accompanying cluster fusion. The probability of electron transfer between the negatively charged and the

neutral clusters is much greater than the probability of electron transfer between the neutral and the positively charged species since electron affinities are much smaller than the ionization potentials for small and medium sized clusters. Therefore, only the electron transfer terms from the negatively charged to the neutral clusters are included

$$(I-4) \quad \dot{X}_i^0 = \dot{X}_i^0 - \sum_{j=1}^N T_{ij} X_i^0 X_j^- + \sum_{j=1}^N T_{ji} X_j^0 X_i^-$$

and

$$(I-5) \quad \dot{X}_i^- = \dot{X}_i^- + \sum_{j=1}^N T_{ij} X_i^0 X_j^- - \sum_{j=1}^N T_{ji} X_j^0 X_i^-$$

where  $T_{ij}$  is the nonsymmetric charge transfer kernel. The coupled rate equations I-(2 through 5) can then be solved simultaneously for the concentrations of the neutral and the charged clusters (15).

Classically, the aggregation probability for clusters  $i$  and  $j$  with diffusion coefficients  $D_i$  and  $D_j$  is proportional to  $D_{ij}R_{ij}$ , where  $D_{ij} = D_i + D_j$  is the joint coefficient for the two clusters, and  $R_{ij}$  is the catching radius within which the clusters will stick with unit probability. In a reactive aggregation, one has to consider the reaction probability within the interaction radius. The expression for reactive aggregation becomes

$$(I-6) \quad K_{ij} = 4\pi D_{ij} R_{ij} [P_{ij} / (P_{ij} + PD)]$$

where  $P_{ij}$  is the reaction probability per unit time and PD is the probability of the reactants to diffuse away. One has  $PD = 1/\tau_{ij}$ , where  $\tau_{ij}$  is the average time in which the clusters remain within the reaction distance  $R_{ij}$ . From the diffusion equation,

$$(I-7) \quad D = (k_B T)^{3/2} / (\sigma p_{\text{He}}^{0.5})$$

one can easily show that  $1/\tau_{ij} = 6D_{ij}/(R_{ij})^2$  leading to

$$(I-8) \quad K_{ij} = 4\pi D_{ij} R_{ij} [P_{ij} / (P_{ij} + (6D_{ij}/R_{ij}^2))]$$

The limiting forms of equation I-8 are of particular interest. If  $P_{ij} > PD$ ,  $K_{ij} \approx 4\pi D_{ij} R_{ij}$  and the distribution of cluster sizes is governed by the classical aggregation kinetics. No reaction-induced magic numbers will arise in this case. The true solution to equation I-1 can be approximated in this case by the ones corresponding to the exactly solvable simple kernels. Since the variation of the kernels with cluster size is not very strong in the classical limit, a constant kernel solution may be used where  $K_{ij} = 2C$  and  $x_1(t=0) = x_0$  may be used for qualitative purposes.

$$(I-9) \quad X_i(t) = X_0 (CX_0 t)^{i-1} / (1 + CX_0 t)^{i+1}$$

A more accurate solution can be obtained provided one includes the variation of the diffusion coefficients and the

catching radii with cluster size. Since cluster reactivity varies with its structure, the uniqueness of the structure explains the reproducibility of the reactivity data for small transition metal clusters (15).

The application of classical kinetics is best exemplified by transition metal clusters. The mass distribution spectra of these clusters are essentially featureless. This is what is predicted by classical kinetics. However, although the distribution of transition metal clusters is classical, the small and medium size clusters will probably have unique or nearly unique shapes. This will result in a certain amount of nonclassical behavior which will cause certain cluster sizes to be favored (15).

In the other limit of equation I-8, where  $PD = 6D_{ij}/(R_{ij})^2 > P_{ij}$ , the growth of clusters is reaction limited. In this case, one can neglect  $P_{ij}$  in the denominator. Since the diffusion constants cancel, the equation becomes

$$(I-10) \quad K_{ij} \approx 4\pi/[6(R_{ij})^3 P_{ij}].$$

Thus the aggregation probability in the reaction limited regime is dependent only on the reaction probability and does not depend on the value of the diffusion coefficient. Therefore, the aggregating clusters will undergo several collisions before fusion. Significant variations in cluster



size are likely to occur since the reaction probabilities depend on structure, symmetry, and the stability of the reacting clusters. This is the reason why magic numbers are observed. The reproducibility of the measured magic numbers under a wide variety of experimental conditions is due to the independence of the rate of fusion on the diffusion coefficient (15).

The knowledge of reaction probabilities for each pair of reacting clusters, including their charge dependence, is required to calculate the cluster distribution in the reaction limited regime. Since this is computationally prohibitive, one is forced to make several approximations in order to make the calculation feasible. The final expression for the aggregation kernel becomes

$$(I-11) \quad K_{ij} = \sigma R_{ij}^3 e^{-\gamma(\Delta G_i^{\ddagger} + \Delta G_j^{\ddagger})/K_B T_{av}}$$

after using the Polanyi-Bronsted relationship to estimate the relative differences between transition state energies. Also, since the reactants are probably going to undergo considerable structural rearrangement after initial attachment, scaled derivatives are used to describe the energy gained upon addition of a single atom. Gibbs free energies can be used to account for the possible temperature

dependent structures which can arise due to the dependence of cluster entropy with structure (15).

The charge transfer kernel is approximated by

$$(I-12) \quad T_{ij} = \sigma R_{ij}^3 e^{-\xi(A_i + A_j)/K_B T_{av}}$$

Since the electronic wave function of a negatively charged cluster has a relatively large radius, the Polanyi-Bronsted proportionality factor,  $\xi$ , in the charge transfer kernel is significantly larger than the corresponding factor in the aggregation kernel (15).

The final two equations require electronic structure calculations for only the end products (those observed in a mass spectrum). The average temperature,  $T_{av}$ , is not known at the outset, but the analysis of experimental spectra provides an upper bound. The spectra of positively charged clusters are thus determined by two adjustable parameters, where as those of negatively charged clusters require an additional parameter ( $\xi$ ) (15).

Ziff and co-workers (16) have studied the validity of using the Smoluchowski equation for cluster-cluster aggregation kinetics. They investigated the validity of the mean-field assumption by looking at the concentrations of the cluster species and also by investigating the asymptotic behavior of the equations. They found the mean-field Smoluchowski equation to be appropriate in describing the

aggregation of particles which form fractal clusters. The only problem was in determining the fractal properties of the kernel. Even though these properties are difficult to determine, once they are known the entire description of the kinetics follows Smoluchowski, as presented by Bernholc and Phillips (15).

The kinetic theory for clustering as presented by Bernholc and Phillips (15) has been able to model the cluster distributions found for carbon by Smalley and co-workers (23). Bernholc and Phillips used the calculated formation energies with a semiempirical estimate of the entropy difference between chains and rings as input for the kinetic energy calculations. They found that the cluster distributions were in good agreement with the experimental work of Smalley. This includes the data for both the positive and negative ions produced directly in the source. The magic numbers in the range of  $n$  equal 10 to 25 were well reproduced. They also found that electron transfer effects have a strong effect on the measured distributions of small and medium clusters of the negative ions. For the positive ions produced from photoionization of neutral clusters, the calculated cluster distributions show that photofragmentation and/or photothreshold and photoionization cross section dependence on cluster size have a major effect on the measured spectra up to about  $n$  equals 25. This was not found to be true for larger clusters.

Even though these are just beginnings in the understanding of what is involved in cluster formation, it is essential to realize that the clusters which are seen by experimentalists are the products of a complicated set of circumstances which may possibly be at the control of the experimentalist. With this type of background it may be possible in the future to produce a desired cluster size by finely tuning the experimental conditions. To be able to do this, it will be necessary to understand what the critical factors are in the formation of clusters. Is it the overall flux of metal in the carrier gas? Can the amount of ionization be controlled in order to produce the desired cluster sizes? Or will the inherent stabilities of certain clusters override these factors and limit the variation of cluster size which can be easily produced? These are questions which will only be answered through a close synergic relationship between experiment and theory.

### ESR Theory

Electron Spin Resonance (ESR) spectroscopy is concerned with the analysis of paramagnetic substances containing permanent magnetic moments of atomic or nuclear magnitude. The theory of ESR spectroscopy has been dealt with by many authors, and if desired a more in depth treatment can be found there (24-29). In the absence of an external field

such dipoles are randomly oriented, but application of a field results in a redistribution over the various orientations in such a way that the substance acquires a net magnetic moment. If an electron or nucleus possesses a resultant angular momentum or spin, a permanent magnetic dipole results and the two are related by

$$(I-13) \quad \underline{\mu} = \gamma \underline{p}$$

where  $\underline{\mu}$  is the magnetic dipole moment vector,  $\underline{p}$  is the angular momentum (an integral or half-integral multiple of  $h/2\pi = \hbar$ , where  $h$  is Planck's constant), and  $\gamma$  is the magnetogyric ratio. The motion of these vectors in a magnetic field  $H$  consists of uniform precession about  $H$  at the Larmor precession frequency

$$(I-14) \quad \underline{\omega} = -\gamma \underline{H}.$$

The component of  $\underline{u}$  along  $\underline{H}$  remains fixed in magnitude, so the energy of the dipole in the field (the Zeeman energy)

$$(I-15) \quad W = -\underline{\mu} \cdot \underline{H}$$

is a constant of the motion.

The relationship between the angular momentum and the

magnetic moment is expressed by the magnetogyric ratio in equation I-13 and is defined by

$$(I-16) \quad \gamma = -g[e/(2mc)]$$

where  $e$  and  $m$  are the electronic charge and mass, respectively, and  $c$  is the speed of light. The  $g$  factor is equal to one for orbital angular momentum and is equal to 2.0023 ( $g_e$ ) for spin angular momentum. Defining the Bohr magneton as  $\beta = e\hbar/2mc$  and combining the  $g$  factor with equation I-13 we have (along the field direction)

$$(I-17) \quad \mu_S = -g_e \beta m_S.$$

Only  $2p+1$  orientations are allowed along the magnetic field and are given by  $m_S \hbar$  where  $m_S$  is the magnetic quantum number taking the values

$$(I-18) \quad m_S = s, s-1, \dots, -s$$

because the angle of the vector  $\underline{\mu}$  is space quantized with respect to the applied field  $\underline{H}$ . This accounts for the appearance in Eq. (I-17) of the  $m_S$  factor for spin angular momentum.

In the case of an atom in a  $^2S_{1/2}$  state where only spin

angular momentum arises, the  $2S+1$  energy levels separate in a magnetic field. Each level will have an energy of

$$(I-19) \quad E_{M_S} = g_e \beta m_S H$$

which will be separated by  $g_e \beta H$ . The  $g$  factor is an experimental value and  $m_S$  an "effective" spin quantum number because the angular momentum does not usually enter into the experiment as purely spin, i.e. some orbital angular momentum usually enters into the observed transitions. For orbitally degenerate states described by strong coupling scheme (Russell-Saunders),  $J=L+S$ ,  $L+S-1$ , ...,  $|L-S|$  and

$$(I-20) \quad E_J = g_J \beta m_J H$$

where

$$(I-21) \quad g_J = 1 + [S(S+1) + J(J+1) - L(L+1)]/[2J(J+1)]$$

is the Lande splitting factor. This reduces to the free electron value for  $L=0$ .

The simplest case of a free spin where  $m_J = m_S = \pm 1/2$  will give two energy levels. The equation for the resonance condition follows:

$$(I-22) \quad h\nu = g_e \beta H_0$$

where  $H_0$  is the static external field and  $\nu$  is the frequency of the oscillating magnetic field associated with the microwave radiation. In this research a frequency of about 9.3 GHz (X-band) was employed. The transitions observed can be induced by application of magnetic dipole radiation obtained from a second magnetic field at right angles to the fixed field which has the correct frequency to cause the spin to flip.

#### The Hyperfine Splitting Effect

As described above, an ESR spectrum would consist of only one line. This would allow one to determine only a value for the  $g$  factor for the species. Fortunately, this is not the only interaction which can be observed via ESR spectroscopy. These other interactions tend to greatly increase the observed number of lines. One of the most important of these interactions is the nuclear hyperfine interaction. ESR experiments are usually designed so that at least one nucleus in the species under investigation has a non-zero magnetic moment. The magnetic moment of the odd electron can interact with this nuclear moment and split the single ESR line into hyperfine structure.

In the simplest case of a nucleus having a spin  $I=1/2$  interacting with a single electron, the magnetic field sensed by the electron is the sum of the applied fields (external and local). A local field would be one caused by the moment



of the magnetic nucleus. This local field is controlled by the nuclear spin state ( $I=1/2$ , in this case). Because there are two nuclear levels ( $2I+1$ ), the electron will find itself in one of two local fields due to the nucleus. This allows two values of the external field to satisfy the resonance condition, which is

$$(I-23) \quad H_r = (H' \pm (A/2)) = (H' - AM_I)$$

where  $A/2$  is the value of the local magnetic field ( $A$  being the hyperfine coupling constant), and  $H'$  is the resonant field for  $A=0$ .

A good example of an ESR spectrum is that of the hydrogen atom with the Zeeman energy levels shown in Figure I-5. Hydrogen has one unpaired electron for which a transition at about  $g_e$  should be observed. Because of the spin angular momentum of the electron interacting with the spin angular momentum of the nucleus ( $I=1/2$ ), two lines are observed. The lines are split around the "g" value for a free electron which is  $g_e = 2.0023$  and occurs at about 3,400 Gauss in an X-Band experiment. The magnitude of the splitting (hyperfine interaction) of the two lines about the free electron position at  $g_e$  is due to the interaction of the free electron with the nuclear moment of the hydrogen atom. The spin angular momentum of the unpaired electron can also be split by several nuclei that have spins, as is the case

with  $\text{CH}_3$ . The carbon nuclei (99%) are  $^{12}\text{C}$  which has zero spin ( $I=0$ ). The hyperfine interaction in this case arises from the three equivalent hydrogen nuclei (each with  $I=1/2$ ) which gives an overall  $I=3/2$ , and four lines are observed (30,31).

Several interactions are involved when a paramagnetic species with a non-zero nuclear spin interacts with a magnetic field. The obvious one is the direct interaction of the magnetic moment with the external field. The precession of the nuclear magnetic moment in the external field results in a similar term. The equation

$$(I-24) \quad g_I \underline{I} = \underline{\mu}_I / \beta_N$$

relates the nuclear magnetic moment  $\mu_I$  to the nuclear g factor ( $g_I$ ). In the equation the nuclear magneton,  $\beta_N$ , is defined as  $e\hbar/2Mc$  where  $M$  is the proton mass and is about 1/2000th of the Bohr magneton.

The Hamiltonian can be written as

$$(I-25) \quad \{H\} = g_J \beta_e \underline{H}^* \{J\} + hA \{I\}^* \{J\} - g_I \beta_N \underline{H}^* \{I\}$$

where  $\{ \}$  indicates that the term is an operator. Small effects such as the nuclear electric quadrupole interaction, as well as the interaction of the nuclear moment with the

external magnetic field (Nuclear Zeeman term), which is the last term in equation I-25, are small and will be neglected.

The Zeeman effect in weak fields is characterized by an external field splitting which is small compared to the natural hyperfine splitting ( $hA\{\underline{I}\} \cdot \underline{J} > g\beta H \cdot \underline{J}$ ) in equation I-25. The orbital electrons and the nuclear magnet remain strongly coupled. The total angular momentum  $\underline{F} = \underline{I} + \underline{J}$  orients itself with the external field and can take the values  $I+J, I+J-1, \dots, |I-J|$ . The component of  $\underline{F}$  along the field direction,  $m_F$ , has  $2F+1$  allowed values. In a weak field the individual hyperfine levels can split into  $2F+1$  equidistant levels which gives a total of  $(2J+1)(2I+1)$  Zeeman levels. (Not all levels are degenerate even at zero field.)

The splitting becomes large compared to the natural hyperfine splitting in the strong field (Paschen-Back) region. Decoupling of  $\underline{I}$  and  $\underline{J}$  occurs because of strong interaction with the external field. Therefore  $F$  is no longer a good quantum number. Since  $\underline{J}$  and  $\underline{I}$  have components along the field direction, the Zeeman level of the multiplet characterized by a fixed  $m_J$  is split into as many Zeeman hyperfine lines as there are possible values of  $m_I$  ( $2I+1$ ). The total energy states are still given by  $(2J+1)(2I+1)$  since there are still  $(2J+1)$  levels for a given  $J$ . The levels in this case form a completely symmetric pattern around the energy center of gravity of the hyperfine multiplet.

Intermediate fields are somewhat more difficult to treat. The transition between the two limiting cases takes place in such a way that the magnetic quantum number,  $m$ , is preserved (In a strong field  $m = m_I + m_J$ , in a weak field  $m = m_P$ ). The Zeeman splitting is of the order of the zero field hyperfine splitting in this region.

With so many possible levels, the observed ESR spectrum needs to be explained in terms of selection rules. The transition between Zeeman levels involves changes in magnetic moments so it is necessary to consider magnetic dipole transitions and the selection rules pertaining to them. A single line is observed for the  $m_S = 1/2 \leftrightarrow -1/2$  transition in the pure spin system ( $I=0$ ). A change in spin angular momentum of  $\pm\hbar$  is necessary. This corresponds to selection rule of  $\Delta m_J = \pm 1$ . A photon has an intrinsic angular momentum equal to  $\hbar$ . Conservation of angular momentum therefore dictates that only one spin can flip (electronic or nuclear) upon absorption of a photon. The transitions usually observed with fields and frequencies employed in the standard ESR experiment are limited to the selection rules  $\Delta m_J = \pm 1$ , and  $\Delta m_I = 0$  (The opposite of NMR work).

These interactions can be categorized as isotropic and anisotropic, and are related to the kind interactions of the electron with the nucleus, and can be deduced from the ESR spectrum. The isotropic interaction is the energy of the nuclear moment in the magnetic field produced at the nucleus

by electric currents associated with the spinning electron. This interaction only occurs with s electrons because they have a finite electron density at the nucleus. The isotropic hyperfine coupling term is given by

$$(I-26) \quad a_S = (8\pi/3)g_e\beta_N\beta_N|\Psi(0)|^2$$

where the final term represents the electron density at the nucleus. There is no classical analog to this term. The  $a_S$  value, also known as the Fermi contact term, is proportional to the magnetic field, and can be of the order of  $10^5$  gauss. It is obvious then very large hyperfine splittings can arise from unpaired s electrons interacting with the nucleus.

Classical dipolar interactions between two magnetic moments are the basis for describing the anisotropic interaction. This interaction can be described by

$$(I-27) \quad E = (\underline{\mu}_e * \underline{\mu}_N)/r^3 - [3(\underline{\mu}_e * \underline{r})(\underline{\mu}_N * \underline{r})]/r^5$$

where  $\underline{r}$  is the radius vector from the moment  $\underline{\mu}_e$  to  $\underline{\mu}_N$ , and  $r$  is the distance between them. Substituting the operators,  $-g\beta\{S\}$  and  $g_N\beta_N\{I\}$ , for  $\underline{\mu}_e$  and  $\underline{\mu}_N$  respectively, gives the quantum mechanical version of equation I-27 as

$$(I-28) \quad H_{dip} = -g\beta g_N\beta_N[\{I\} * (\{L\} - \{S\})/r^3 - 3(\{I\} * \underline{r})(\{S\} * \underline{r})/r^5].$$

Then a dipolar term arises

$$(I-29) \quad a = g_e \beta g_I \beta_N [(3 \cos^2 \theta - 1) / r^3]$$

where  $\theta$  is the angle between the line connecting the two dipoles and the direction of the magnetic field. The angular term found in Eq. (I-29) needs to be averaged over the electron probability distribution function because the electron is not localized. The average of  $\cos^2 \theta$  over all  $\theta$  vanishes for an s orbital because of the spherical symmetry of the orbital.

### Doublet Sigma Molecules

#### The spin Hamiltonian

The full spin Hamiltonian involves all the interactions of the unpaired spin within the molecule, not just the ones directly affected by the magnetic field. The full Hamiltonian contains the terms below,

$$(I-30) \quad H = H_F + H_{Ze} + H_{LS} + H_{hf} + H_{Zn}$$

the magnitude of the terms on the right side of Eq. (I-30) tend to decrease going from left to right. The first term in equation I-30 is the total kinetic energy of the electrons. The "Ze" and "Zn" terms describe the electronic and nuclear Zeeman interactions, respectively. The energy,  $H_{LS}$ , is due

to the spin-orbit coupling interaction. The term,  $H_{hf}$ , accounts for the hyperfine interaction due to the electronic angular momentum and magnetic moment interacting with a nearby nuclear magnetic moment. These terms have been adequately described in detail by several authors (24-27).

This full Hamiltonian is rather complicated and difficult to use in calculations, and the higher order terms which could be observed in crystals have not been included. Using a spin Hamiltonian in a simplified manner, it is possible to interpret experimental ESR data. This was first done by Abragam and Pryce (32). The ESR data are usually of the lowest-lying spin resonance levels which are commonly separated by a few  $\text{cm}^{-1}$ . All other states lie considerably higher in energy and are generally not observed. The behavior of this smaller group of levels in the spin system can be described by a simplified Hamiltonian. The splittings are the same as if one ignored the orbital angular momentum and replaced its effect by an anisotropic coupling between the spin and the external magnetic field.

Since  $\{S\}$  cannot represent a true spin, it represents an "effective" spin. This is related to the anisotropy found in the  $g$  factor which does not necessarily equal  $g_e$ . By convention, the "effective"  $g$  factor is defined so that the observed number of levels equals  $2S+1$ , just like the real spin multiplet. Therefore all the magnetic properties of a system can be related to this effective spin by the spin

Hamiltonian. This is possible because the spin Hamiltonian combines all of the terms in the full Hamiltonian that are effected by spin. Nuclear spins can be treated in a similar fashion, so that the spin Hamiltonian which corresponds to Eq. (I-30) can be written as

$$(I-31) \quad H_{\text{Spin}} = \beta H_0 * g * \{S\} + \{I\} * A * \{S\}$$

where  $g$  and  $A$  are tensor quantities and the nuclear Zeeman term has been neglected.

#### The $g$ tensor

The anisotropy of the  $g$ -tensor arises from the orbital angular momentum of the electron through spin-orbit coupling. The anisotropy occurs even in the sigma states which nominally have zero orbital angular momentum. Apparently the pure spin ground state interacts with low-lying excited states which add a small amount of orbital angular momentum to the ground state. This small amount is enough to change the values of the  $g$  tensor. The interaction is generally inversely proportional to the energy separation between the states. This spin-orbit interaction is given by

$$(I-32) \quad \{H\}_{LS} = \lambda \{L\} * \{S\} = \lambda (\{L\}_x \{S\}_x + \{L\}_y \{S\}_y + \{L\}_z \{S\}_z)$$

This term is added to the Zeeman term in the spin Hamiltonian



$$(I-33) \quad \{H\} = \beta \underline{H}^* (\{ \underline{L} \} + g_e \{ \underline{S} \}) + \lambda \{ \underline{L} \}^* \{ \underline{S} \}.$$

For an orbitally nondegenerate ground state represented by  $|G, M_S\rangle$ , the first order energy is given by the diagonal matrix element

$$(I-34) \quad W_G = \langle G, M_S | g_e \beta_z \{ \underline{S} \}_z | G, M_S \rangle \\ + \langle G | \{ \underline{L} \}_z | G \rangle \langle M_S | \beta H_z + \lambda \{ \underline{S} \}_z | M_S \rangle$$

where the first term is the spin-only electronic Zeeman effect. The term,  $\langle G | \{ \underline{L} \}_z | G \rangle$ , vanishes since the ground state is orbitally non-degenerate. The second order correction to each element in the Hamiltonian is given by

$$(I-35) \quad \{H\}_{M_S M_S'} = - \sum_n' [ ( \langle G, M_S | (\beta \underline{H} + \lambda \{ \underline{S} \})^* \{ \underline{L} \} \\ + g_e \beta \underline{H}^* \{ \underline{S} \} | n, M_S' \rangle^2 ) / (W_n^{(0)} - W_G^{(0)}) ]$$

where the prime designates summation over all states except the ground state. The matrix elements of  $g_e \beta \underline{H} \{ \underline{S} \}$  will vanish because  $\langle G | n \rangle = 0$ .

Expanding this, it is possible to factor out a quantity

$$(I-36) \quad \underline{A} = ( - \sum_n' \langle G | \{ \underline{L} \} | n \rangle \langle n | \{ \underline{L} \} | G \rangle ) / (W_n^{(0)} - W_G^{(0)})$$

which is a second rank tensor. The  $ij$ th element of this tensor is given by

$$(I-37) \quad \Lambda_{ij} = (-\sum_n \langle G | L_i | n \rangle \langle n | L_j | G \rangle) / (W_n^{(0)} - W_G^{(0)})$$

where  $L_i$  and  $L_j$  are orbital angular momentum operators appropriate to the  $x$ ,  $y$ , or  $z$  directions. Substituting this tensor into  $H_{M_S, M_S'}$  yields

$$(I-38) \quad H_{M_S, M_S'} = \langle M_S | \beta^2 \{H\} * \{\Lambda\} * \{H\} + 2\lambda \beta \{H\} * \{\Lambda\} * \{S\} + \lambda^2 \{S\} * \{\Lambda\} * \{S\} | M_S' \rangle$$

The first operator does not need to be considered any further since it represents a constant contribution to the paramagnetism. The second and third terms constitute a Hamiltonian which operates only on spin variables. The spin Hamiltonian results when the operator  $g_e \beta \{H\} * \{S\}$  is combined with the last two terms of Eq. (I-38). The spin Hamiltonian takes the form of

$$(I-39) \quad H_{Spin} = \beta \{H\} * (g_e \{1\} + 2\lambda \{\Lambda\}) * \{S\} + \lambda^2 \{S\} * \{\Lambda\} * \{S\} \\ = \beta \{H\} * \{g\} * \{S\} + \{S\} * \{D\} * \{S\}$$

where

$$(I-40) \quad \{g\} = g_e \{1\} + 2\lambda \{\Lambda\}$$

and

$$(I-41) \quad \{D\} = \lambda^2 \{\Lambda\}.$$

The final term in equation I-39 is effective only in systems with  $S \geq 1$ . The first term is then the spin Hamiltonian for a  $^2\Sigma$  molecule. The anisotropy of the g-tensor arises from the spin-orbit interaction due to the orbital angular momentum of the electron which is evident from the derivation.

The g-tensor would be isotropic and equal to 2.0023 if the angular momentum of the system is due solely to spin angular momentum. Deviation (anisotropy) from this value results from the mixing in of orbital angular momentum from excited states which is expressed through the  $\{\Lambda\}$  tensor.

If a molecule has axes of symmetry, they need to coincide with the principal axes of the g tensor. Three cases of interest can be outlined. The simplest case is one in which g is equal to  $g_e$ . This is a spin only system for which g is isotropic. For a system containing an n-fold axis of symmetry ( $n \geq 3$ ) there are two equivalent axes. The axis designated z is the unique axis and the g value for the field (H) perpendicular to z is  $g_{\perp}$  and  $g_{\parallel}$  is the value for g when H is parallel to z. The spin Hamiltonian therefore becomes

$$(I-42) \quad H_{\text{Spin}} = \beta(g_{\perp}H_x\{S\}_x + g_{\perp}H_y\{S\}_y + g_{\parallel}H_z\{S\}_z).$$

The third case deals with the situation where the molecule

contains no equivalent axes (orthorhombic symmetry), where  $g_{xx}$ ,  $g_{yy}$ , and  $g_{zz}$  are not equal and

$$(I-43) \quad \{H\}_{Spin} = \beta(g_{xx}H_x\{S\}_x + g_{yy}H_y\{S\}_y + g_{zz}H_z\{S\}_z).$$

### The A tensor

The hyperfine tensor takes into account three types of interactions. The first term involves the interaction between the magnetic field produced by the orbital momentum and the nuclear moment,  $L \cdot I$  which is usually small. More important terms involve the interactions due to the amount of s character of the wavefunction (the Fermi contact term) and to the non-s character of the wavefunction also need to be accounted for.

The isotropic interaction due to the s character is called  $A_{iso}$ . Fermi (33) has shown that for systems with one electron the isotropic interaction energy is approximately given by

$$(I-44) \quad W_{iso} = -(8\pi/3) |\Psi(0)|^2 \mu_e \mu_N \rho_N$$

where  $\Psi(0)$  represents the wave function evaluated at the nucleus.

The interaction arising from the dipole-dipole interaction of the nucleus and electron (non-s character) is called  $A_{dip}$ . The dipolar interaction gives rise to the

anisotropic component of hyperfine coupling in the rigid matrix environment. The expression for the dipolar interaction energy between an electron and nucleus separated by a distance  $r$  is

$$(I-45) \quad W_{\text{dipolar}} = (\mu_e \mu_N) / r^3 - [3(\mu_e r)(\mu_N r)] / r^5.$$

The term,  $H_{\text{hf}}$ , can now be written as

$$(I-46) \quad \begin{aligned} H_{\text{hf}} &= H_{\text{iso}} + H_{\text{dip}} \\ &= [A_{\text{iso}} + H_{\text{dip}}] \underline{I} \cdot \underline{S} \end{aligned}$$

where  $A_{\text{iso}}$  has been given in Eq. (I-26) and  $A_{\text{dip}}$  can be expressed by equation I-29. The brackets indicate the average of the expressed operator over the wave function  $\Psi$ . In tensor notation the term become

$$(I-47) \quad H_{\text{hf}} = \underline{I} \cdot \underline{A} \cdot \underline{S}$$

where  $\underline{A} = A_{\text{iso}} \underline{1} + \underline{T}$ . Here  $\underline{1}$  is the unit tensor and  $\underline{T}$  is the tensor representing the dipolar interaction. The components of the  $A$  tensor becomes

$$(I-48) \quad A_{ij} = A_{\text{iso}} \underline{1}_{ij} + T_{ij}.$$

For a completely isotropic system the components of the A tensor ( $A_{xx}$ ,  $A_{yy}$ ,  $A_{zz}$ ) will equal  $A_{iso}$ . A system with axial symmetry is treated in a manner similar to that of the g tensor where  $A_{xx}$  and  $A_{yy}$  are equal to  $A_{\perp}$ . The term,  $A_{\perp}$ , is given by

$$(I-49) \quad A_{\perp} = A_{iso} + T_{xx} \quad ,$$

and  $A_{zz}$  is equal to  $A_{\parallel}$  which is given by

$$(I-50) \quad A_{\parallel} = A_{zz} + T_{zz} \quad .$$

And finally for a system which exhibits a completely anisotropic A tensor  $A_{xx}$ ,  $A_{yy}$ ,  $A_{zz}$  are not equal to each other.

In matrix isolation experiments only the absolute values of the hyperfine parameters can be determined. In most matrix isolation experiments, it is found that for the most part, the signs of  $A_{\perp}$  and  $A_{\parallel}$  are positive. There are two general exceptions to this. First, this may not generally be true for very small hyperfine interactions, such as the hyperfine interaction in CN where the splitting due to  $^{14}\text{N}$  is only 5 to 10 gauss. Second, if  $\mu_I$  is negative, the A values will usually be negative, also (34).

Randomly oriented molecules

There is a very distinct difference between samples held in a single crystal and those trapped in matrices. In the case of a single crystal, the sample can be aligned to the external field and spectra recorded at various angles of the molecular axes to the field. Matrix isolated samples are usually randomly oriented within the field and the observed spectra will contain contributions from molecules at various angles. This was first considered by Bleaney (35,36), and later by others (37-43)

In the orthorhombic case the spin Hamiltonian can be solved (assuming the  $g$  tensor to be diagonal), and the energy levels can be given by

$$\begin{aligned}
 \text{(I-51)} \quad E &= \beta \underline{S}_H (g_1^2 \sin^2 \theta \cos^2 \phi + g_2^2 \sin^2 \theta \sin^2 \phi \\
 &\quad + g_3^2 \cos^2 \theta)^{0.5} \\
 &= \beta g_H \underline{S}_H H
 \end{aligned}$$

where  $\underline{S}_H$  is the component of the spin vector  $S$  along  $H$ ,  $g_H$  is the  $g$  value in the direction of  $H$ ,  $\theta$  is the angle between the molecular  $z$  axis and the field direction, and  $\phi$  is the angle from the  $x$  axis to the projection of the field vector in the  $xy$  plane. Returning to axial symmetry

$$\text{(I-52)} \quad g_H = (g_{\perp}^2 \sin^2 \theta + g_{\parallel}^2 \cos^2 \theta)^{0.5}$$

and the energy of the levels is given by

$$(I-53) \quad E = \beta S_H H (g_{\perp}^2 \sin^2 \theta + g_{\parallel}^2 \cos^2 \theta).$$

It is obvious that the splittings between the energy levels are angularly dependent. This makes the transitions between the energy levels also angularly dependent.

The absorption intensity as a function of angle is proportional to the number of molecules lying between  $\theta$  and  $\theta + d\theta$ , assuming the transition probability is independent of orientation. Since  $g$  is a function of  $\theta$  for a fixed frequency  $\nu$ , the resonant magnetic field is

$$(I-54) \quad H = (h\nu/\beta)(g_{\parallel}^2 \cos^2 \theta + g_{\perp}^2 \sin^2 \theta)^{-0.5}$$

and from this

$$(I-55) \quad \sin^2 \theta = (g_0 H_0 / H)^2 - g_{\parallel}^2 / (g_{\perp}^2 - g_{\parallel}^2)$$

where  $g_0$  equals  $(g_{\parallel} + 2g_{\perp})/3$  and  $H_0$  equals  $h\nu/g_0\beta$ . From the above equations we have

$$(I-56) \quad H = h\nu/g_{\parallel}\beta = g_0 H_0 / g_{\parallel} \quad \text{at } \theta = 0^\circ$$

and

$$(I-57) \quad H = h\nu/g_{\perp}\beta = g_0 H_0 / g_{\perp} \quad \text{at } \theta = 90^\circ.$$

The absorption intensity varies from  $0^\circ$  to  $90^\circ$  and when plotted against magnetic field, takes the appearance of



Figure I-6a, for  $g_{\parallel} > g_{\perp}$ . In a typical ESR experiment one usually measures the first derivative of the absorption signal. This spectrum appears in part b of Figure I-6. The perpendicular component is generally easily determined from such a powder pattern. It is usually the strongest signal observed. The parallel component is typically much weaker and usually more difficult to detect. The values of  $g_{\parallel}$  and  $g_{\perp}$  can be determined as indicated assuming that the  $g$  tensor is not very anisotropic.

Hyperfine interaction with spin containing nuclei can split the pattern shown in Figure I-6b into  $(2I+1)$  such patterns. A simple case would be that of a molecule containing an  $I=1/2$  nucleus. This is presented in Figure I-6c. One important point is that the orientation of the  $m_I=1/2$  pattern is opposite to that of the  $m_I=-1/2$  pattern. This is because  $g_{\parallel}$  is approximately equal to  $g_{\perp}$ , and  $A_{\perp} < A_{\parallel}$ . Another common situation is that of the hyperfine splitting for both parallel and perpendicular orientations are almost equal and  $g_{\perp}$  is shifted up-field from  $g_{\parallel}$ . In this case the spectrum would contain two features like Figure I-6b separated by the hyperfine splitting,  $A$ .

#### Molecular parameters and the observed spectrum

With all of this theory, the question now becomes what can be learned from an ESR spectrum? To answer this, let us begin with the solution of the spin Hamiltonian in axial

$$h\nu = g\beta H_0 \approx 9,500 \text{ MHz}$$

$$g = 2.0023$$

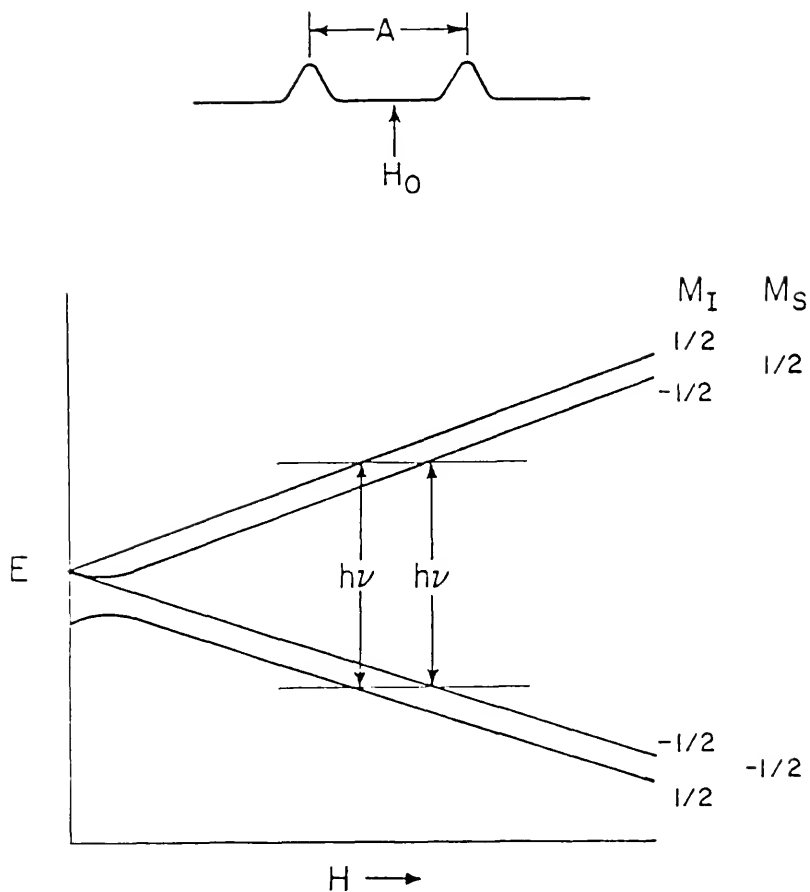


Figure Figure I-5. Zeeman energy levels of an electron interacting with a spin 1/2 nucleus.

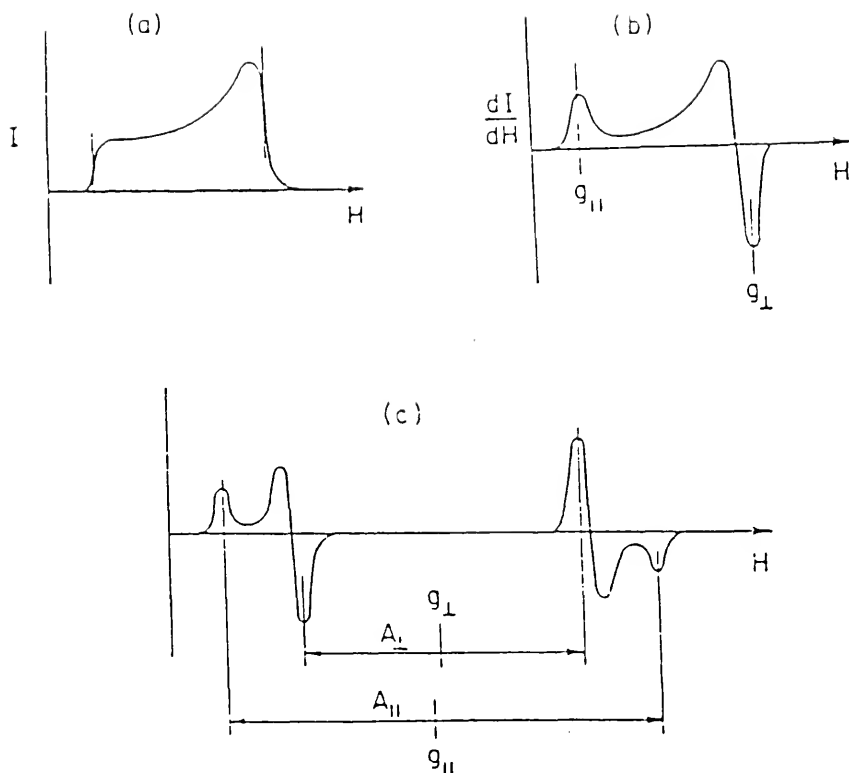


Figure I-6. (a) Absorption and (b) first derivative lineshapes of randomly oriented molecules with axial symmetry and  $g_{\perp} < g_{||}$ ; (c) first derivative lineshape of randomly oriented, axially symmetric molecules  $g_{\perp} < g_{||}$ , including hyperfine interaction with a spin 1/2 nucleus ( $A_{\perp} < A_{||}$ ).

symmetry including second order perturbations. This will then show what molecular parameters can be uncovered from an ESR spectrum.

Several authors (24,26,27,38) have given detailed discussions of the spin Hamiltonian

$$(I-58) \quad \{H\}_{\text{Spin}} = g_{\parallel} \beta H_z \{S\}_z + g_{\perp} \beta (H_x \{S\}_x + H_y \{S\}_y) \\ + A_{\parallel} \{I\}_z \{S\}_z + A_{\perp} (\{I\}_x \{S\}_x + \{I\}_y \{S\}_y).$$

Considering the Zeeman term first, a transformation of axes is performed to generate a new coordinate system  $x'$ ,  $y'$ , and  $z'$ , with  $z'$  parallel to the field. If the direction of  $H$  is taken as the polar axis and  $\theta$  is the angle between  $z$  and  $H$ , then  $y$  can be arbitrarily chosen to be perpendicular to  $H$  and hence  $y=y'$ . Therefore only  $x$  and  $z$  need to be transformed. The Hamiltonian is transformed to

$$(I-59) \quad \{H\} = g\beta H \{S\}_{z'} + K \{I\}_{z'} \{S\}_{z'} + (A_{\parallel} A_{\perp} / K) \{I\}_{x'} \{S\}_{x'} \\ + [(A_{\perp}^2 - A_{\parallel}^2) / K] (g_{\parallel} g_{\perp} / g^2) \sin \theta \cos \theta \{I\}_{x'} \{S\}_{x'} \\ + A_{\perp} \{I\}_{y'} \{S\}_{y'},$$

where  $l_z^n = A_{\parallel} g_{\parallel} \cos \theta / Kg$ ,  $l_x^n = A_{\perp} g_{\perp} \sin \theta / Kg$ , and  $K^2 g^2 = A_{\parallel}^2 g_{\parallel}^2 \cos^2 \theta + A_{\perp}^2 g_{\perp}^2 \sin^2 \theta$ . Dropping the primes and using ladder operators  $\{S\}^+ = \{S\}_x + i\{S\}_y$  and  $\{S\}^- = \{S\}_x - i\{S\}_y$ , this can be rewritten in the final form

$$\begin{aligned}
 (I-60) \quad H_{\text{Spin}} = & g\beta H \{S\}_Z + K \{S\}_Z \{I\}_Z \\
 & + [((A_{\perp}^2 - A_{\parallel}^2)/K)((g_{\parallel}g_{\perp})/g^2) \\
 & \cdot \cos\theta \sin\theta ((\{S\}^+ + \{S\}^-)/2) \{I\}_Z] \\
 & + [((A_{\parallel}A_{\perp})/4K) + A_{\perp}/4] (\{S\}^+ \{I\}^+ + \{S\}^- \{I\}^-) \\
 & + [((A_{\parallel}A_{\perp})/4K) + A_{\perp}/4] (\{S\}^+ \{I\}^- + \{S\}^- \{I\}^+).
 \end{aligned}$$

This Hamiltonian can be solved for the energies at any angle by letting the Hamiltonian matrix operate on the spin kets  $|M_S, M_I\rangle$ . The solution of the spin Hamiltonian is difficult to solve at all angles except at  $\theta=0^\circ$  and  $90^\circ$ . Elimination of some of the off-diagonal elements results in some simplification and is usually adequate. The solution is then correct to second order, and can be used when  $g\beta H \gg A_{\parallel}$  and  $A_{\perp}$ , as is typically the case. The general second-order solution is given by Rollman and Chan (44) and by Bleaney (36). The energy levels are given by

$$\begin{aligned}
 (I-61) \quad \Delta E(M, m) = & g\beta H + Km + (A_{\perp}^2/8G)[(A_{\parallel}^2 + K^2)/K^2] \\
 & \cdot [I(I+1) - m^2] + (A_{\perp}^2)(A_{\parallel}/K)(2M - 1)
 \end{aligned}$$

where  $K$  is  $A_{\parallel}$  and  $A_{\perp}$  at  $\theta=0^\circ$  and  $90^\circ$ , respectively, and  $G=g\beta H/2$ . Also,  $M$  is the electron spin quantum number of the lower level in the transition, and  $m$  is the nuclear spin quantum number. The first two terms on the right result from the diagonal matrix elements and yield equidistant hyperfine lines. The last two terms cause spacing of the hyperfine

lines at higher field to increase, which is referred to as a second-order effect. This solution is routinely applied because the hyperfine energy is usually small and not comparable to the Zeeman energy.

As described above, the hyperfine coupling constant consists of both an isotropic and anisotropic part. The isotropic part ( $A_{iso}$ ) can be written as

$$(I-62) \quad A_{iso} = (A_{||} + 2A_{\perp})/3 = (8\pi/3)g_e\beta g_N\beta_N|\Psi(0)|^2.$$

The isotropic hyperfine parameter can be used to determine the amount of unpaired s spin density. The dipolar component can be written as

$$(I-63) \quad A_{dip} = (A_{||} - A_{\perp})/3 = g_e\beta g_N\beta_N \langle (3\cos^2\theta - 1)/2r^3 \rangle$$

These then relate the fundamental quantities  $|\Psi(0)|^2$  and  $\langle (3\cos^2\theta - 1)/(2r^3) \rangle$  to the observed ESR spectrum. Approximate spin densities in the molecule can also be obtained from  $A_{iso}$  and  $A_{dip}$ .

#### Spin densities

The electron spin density,  $\rho_x$  at a nucleus X is the unpaired electron probability density at the nucleus. In the case of a single unpaired electron it is the fraction of that electron/cm<sup>3</sup> at a particular nucleus. The spin density of the unpaired electron is generally split among s, p and d

orbitals. The spin density at nucleus X for an s electron is given by  $\rho_{sX} |X_{sX}(0)|^2$  and for electrons in a  $p\sigma$  orbital the spin density is given by  $\rho_{p\sigma X} \langle X_{p\sigma X} | (3\cos^2\alpha - 1)/r^3 | X_{p\sigma X} \rangle$ .

Similar expressions can be given for  $p\pi$  and  $d\sigma$ , etc.

orbitals. The terms  $\rho_{sX}$  and  $\rho_{p\sigma X}$  represent the contributions of the s and  $p\sigma$  orbitals to the spin density at nucleus X.

The isotropic and anisotropic hyperfine parameters can be written as

$$(I-64) \quad A_{iso}^X (\text{molecule}) = (8\pi/3) g_e \beta_e g_I \beta_N \rho_{sX} |X_{sX}(0)|^2$$

$$(I-65) \quad A_{dip}^X (\text{molecule}) = g_e \beta_e g_I \beta_N \rho_{p\sigma X} \langle X_{p\sigma X} | (3\cos^2\alpha - 1)/2r^3 | X_{p\sigma X} \rangle.$$

Since the equations above are characteristic of atom X, it is possible to rewrite them for  $A_{iso}$  and  $A_{dip}$  as given below

$$(I-66) \quad A_{iso}^X (\text{molecule}) = \rho_{sX} A_{iso}^X (\text{atom})$$

$$(I-67) \quad A_{dip}^X (\text{molecule}) = \rho_{p\sigma X} A_{dip}^X (\text{atom}).$$

From Eqs. (I-66,67) one can easily obtain an expression relating the unpaired spin density to the isotropic and anisotropic hyperfine parameters,

$$(I-68) \quad \rho_{sX} = A_{iso}^X (\text{molecule}) / A_{iso}^X (\text{atom})$$

$$(I-69) \quad \rho_{2p\sigma X} = A_{dip}^X (\text{molecule}) / A_{dip}^X (\text{atom}).$$

The hyperfine parameters for the molecule are obtained from the ESR spectra. The hyperfine parameters for the atoms can be obtained from tables (see Weltner (24), Appendix B) and multiplied by the appropriate correction factors. The correct value of  $A_{dip}$  is calculated by taking the free atom value of  $P = g_e \beta_e g_N \beta_N$  and multiplying it by an angular factor  $\alpha/2 = \langle (3\cos^2\alpha - 1)/2 \rangle$ . The factor equals 2/5 for a p electron, 2/7 for a d electron and 4/15 for an f electron. The value for  $A_{iso} (\text{atom})$  can be found in Table B1 (column 5) of Weltner (24) and the uncorrected value for  $A_{dip} (\text{atom})$  can be found in column 7 of the same Table.

#### Quartet Sigma Molecules ( $S=3/2$ )

These high spin molecules ( $S>1$ ) often contain transition metals. The metal atom will generally have a large zero field splitting (D) value due to its large spin-orbit coupling constant ( $\xi$ ). If there are only a few ligands attached to the metal atom, the unpaired electrons will be confined to a small volume which will cause a sizable spin-spin interaction. A large D value will cause many predicted lines to be unobservable.



### The spin Hamiltonian

A  $4\Sigma$  molecule will exhibit a fine structure spectrum. A theorem due to Kramer states that in the absence of an external magnetic field the electronic states of any molecule with an odd number of electrons will be at least doubly degenerate. In the case of a quartet molecule the zero field splitting produces two Kramer's doublets, or degenerate pairs of states, with  $M_S$  values of  $\pm 1/2$  and  $\pm 3/2$ .

The spin Hamiltonian for a quartet sigma molecule with axial symmetry can be written as

$$(I-70) \quad \{H\}_{\text{Spin}} = g_{\parallel} \beta H_Z \{S\}_Z + g_{\perp} H_X \{S\}_X + D((\{S\}_Z)^2 - 5/4).$$

This equation does not take into account hyperfine structure. A 4X4 spin matrix can be calculated which upon diagonalization yields four eigenvalues

$$(I-71) \quad W(\pm 3/2) = D \pm (3/2) g_{\parallel} \beta H$$

$$(I-72) \quad W(\pm 1/2) = D \pm (1/2) g_{\parallel} \beta H$$

and at zero field the  $\pm 3/2$  level and the  $\pm 1/2$  level are separated by  $2D$ . With  $H$  parallel to the molecular axis, the energy levels will vary linearly with the magnetic field. For the applied field perpendicular to the principal axis ( $H_{\perp Z}$ ) with  $H_X = H$  and  $H_Z = 0$ , the eigenvalues are more difficult to calculate because the off-diagonal terms are no

longer zero. The eigenvalue matrix can be expanded to yield a quartic equation

$$(I-73) \quad E^4 - 1/2(1 + 15x^2)E^2 + 3x^2E + (1/16)(1 + 6x^2 + 81x^4) = 0,$$

where  $E = W/2D$  and  $x = g_{\perp}\beta H / (2(3)^{0.5}D)$ . Singer (45) has developed a more general form of the equation which can be applied to any angle. The eigenvalues for  $H_{\perp}z$  can be expressed as

$$(I-74) \quad W(\pm 3/2) = D \pm (3/8D)(g_{\perp}\beta H)^2 + \dots$$

$$(I-75) \quad W(\pm 1/2) = -D \pm g_{\perp}\beta H - (3/8D)(g_{\perp}\beta H)^2 + \dots,$$

when  $H/D$  or  $x$  is small. By expanding  $E$  it can then be given as  $E = a + bx + cx^2 + \dots$ , with the levels indexed by the low field quantum numbers.

When  $D > g\beta H^* \{S\}$  all the matrix elements of the type  $\langle \pm 3/2 | \{H\}_{\text{Spin}} | \pm 1/2 \rangle = \langle \pm 1/2 | \{H\}_{\text{Spin}} | \pm 3/2 \rangle$  vanish. This approach yields the eigenvalues below,

$$(I-76) \quad W(\pm 3/2) = D \pm (3/2)g_{\parallel}\beta H \cos \theta$$

$$(I-77) \quad W(\pm 1/2) = -D \pm (1/2)\beta zH(g_{\parallel}^2 \cos^2 \theta + 4g_{\perp}^2 \sin^2 \theta)^{0.5},$$

remembering that  $H_z = H \cos \theta$  and  $H_x = H \sin \theta$  and that the angle between the molecular axis and the applied field is  $\theta$ . This

is used to introduce the "effective" or apparent  $g$  value. The effective  $g$  value generally indicates where the transition occurs and is defined by assuming that the resonance is occurring within the doublet, that is between  $M_S = \pm 1/2$  levels with  $g = g_e$ . The  $g$  values of the observable transitions  $|+3/2\rangle \leftrightarrow |-3/2\rangle$  and  $|+1/2\rangle \leftrightarrow |-1/2\rangle$  become

$$(I-78) \quad M_S = \pm 3/2 \quad \underline{g_{\parallel}} \approx 3g_{\parallel} \approx 6.0 \quad \underline{g_{\perp}} \approx 0.0$$

$$(I-79) \quad M_S = \pm 1/2 \quad \underline{g_{\parallel}} \approx g_{\parallel} \approx 2.0 \quad \underline{g_{\perp}} \approx 2g_{\perp} \approx 4.0$$

for a large zero field splitting. The underlines indicate the effective  $g$  value. The derivative signal for the  $\pm 3/2$  transition is usually undetectable because of the low population of that level. There is not a significant population of the  $\pm 3/2$  level unless  $D$  is very small. Also, the absorption pattern corresponding to the  $g$  values for this transition would be very broad. Finally, assuming that  $H/D$  is large implies that the transition is forbidden. The transitions usually observed for this spin state are those between the  $\pm 1/2$  levels (the lower Kramer's doublet). Kasai (46) and Brom et al. (47) have analyzed  $^4\Sigma$  molecules and found the following spin Hamiltonian.

$$(I-80) \quad \{H\}_{\text{Spin}} = g_{\parallel} \beta H_Z \{S\}_Z + g_{\perp} \beta (H_X \{S\}_X + H_Y \{S\}_Y) \\ + A_{\parallel} \{I\}_Z \{S\}_Z + A_{\perp} (\{I\}_X \{S\}_X + \{I\}_Y \{S\}_Y) \\ + D[(\{S\}_Z)^2 - (1/3)S(S+1)]$$

and rewrote it as an effective spin Hamiltonian

$$(I-81) \quad \{H\}_{Spin} = g_{\parallel} \beta H_z \{S\}_z + 2g_{\perp} \beta (H_x \{S\}_x + H_y \{S\}_y) \\ + A_{\parallel} \{I\}_z \{S\}_z + 2A_{\perp} (\{I\}_x \{S\}_x + \{I\}_y \{S\}_y)$$

for the  $\pm 1/2$  transition. The D term vanishes and S is taken to be  $1/2$ . The effective spin Hamiltonian can be rearranged to be diagonal. The Zeeman terms become

$$(I-82) \quad \{H\}_{Spin} = g\beta H \{S\}_z + A \{I\}_z \{S\}_z \\ + ((4(A_{\perp}^2) - (A_{\parallel})^2)/A) \\ \cdot (2g_{\parallel} g_{\perp} / g^2) \sin \theta \cos \theta \{I\}_z \{S\}_z \\ + (1/2) A_{\perp} [(A_{\parallel} + A)/A] (\{I\}^+ \{S\}^- + \{I\}^- \{S\}^+) \\ + (1/2) A_{\perp} [(A_{\parallel} + A)/A] (\{I\}^+ \{S\}^+ + \{I\}^- \{S\}^-)$$

where  $g^2 = (g_{\parallel})^2 \cos^2 \theta + 4(g_{\perp})^2 \sin^2 \theta$ , and  $A^2 = ((A_{\parallel})^2 \cdot (g_{\parallel})^2 / g^2) \cos^2 \theta + (16(A_{\perp})^2 (g_{\perp})^2 / g^2) \sin^2 \theta$ . This equation can be solved analytically at  $\theta = 0^\circ$  and by a continued fraction method at  $\theta = 90^\circ$ . A computer program is usually used to match the observed lines with those calculated by the iterative procedure in order to come up with the values for g and A.

The observed transitions and therefore the energy levels are typically very dependent on  $\theta$  and D. Figures I-7 and I-8 indicate the levels as a function of field for the perpendicular and parallel orientations, respectively. Two

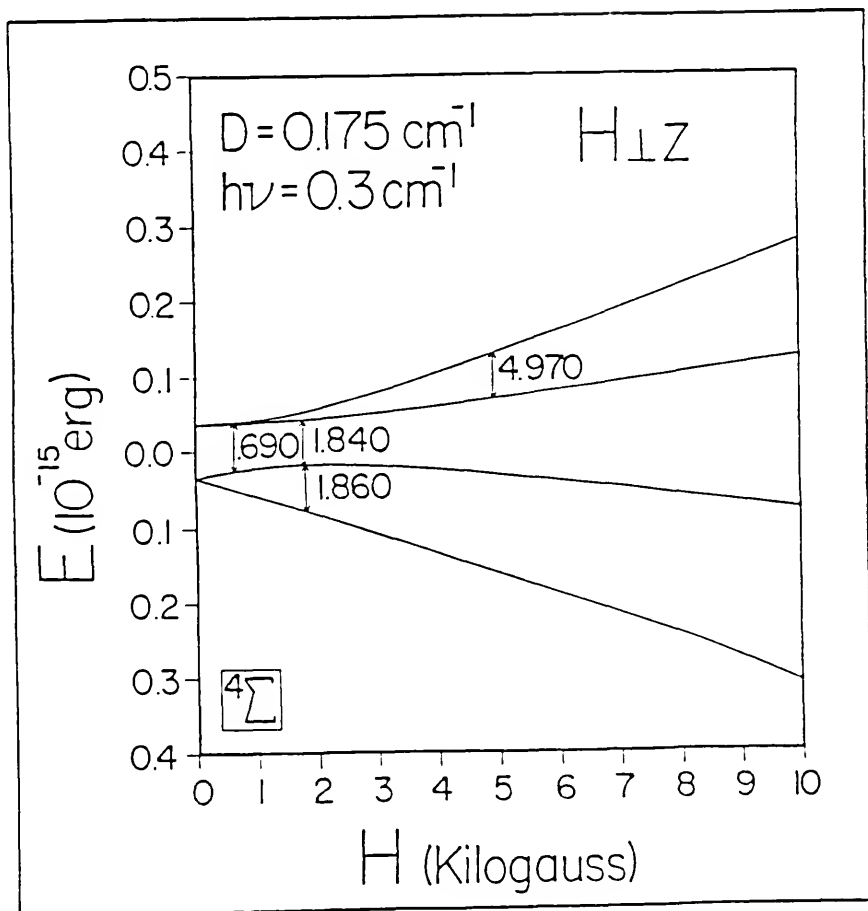


Figure I-7. Energy levels for a  $4\Sigma$  molecule in a magnetic field; field perpendicular to molecular axis.

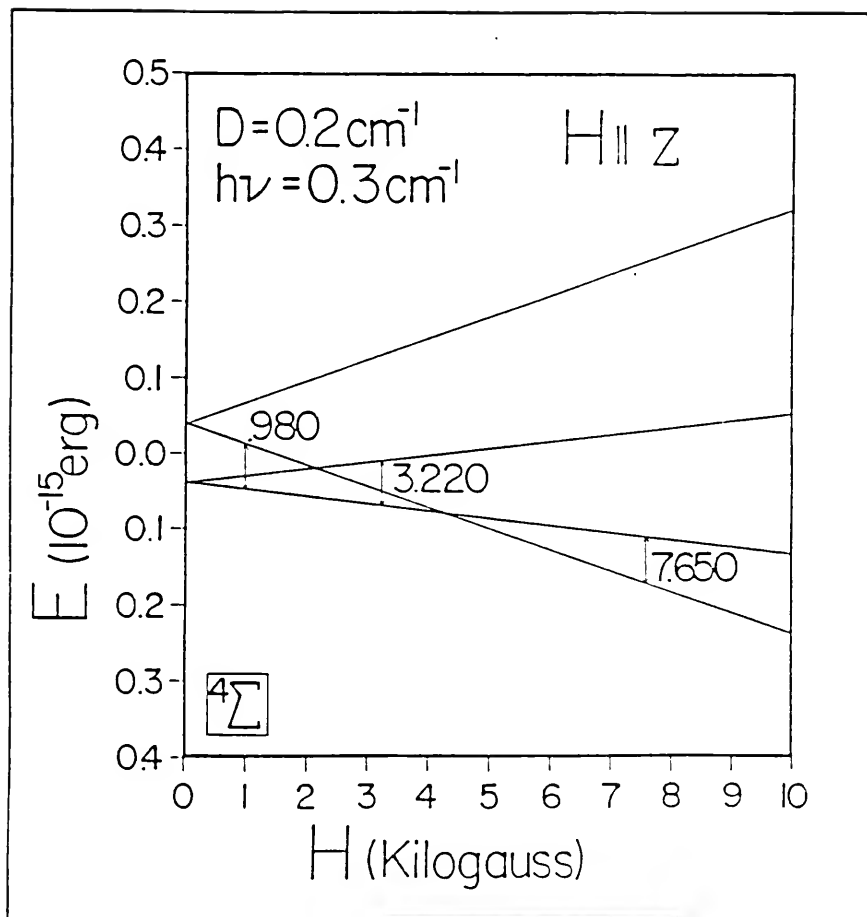


Figure I-8. Energy levels for a  $4\Sigma$  molecule in a magnetic field; field parallel to molecular axis.

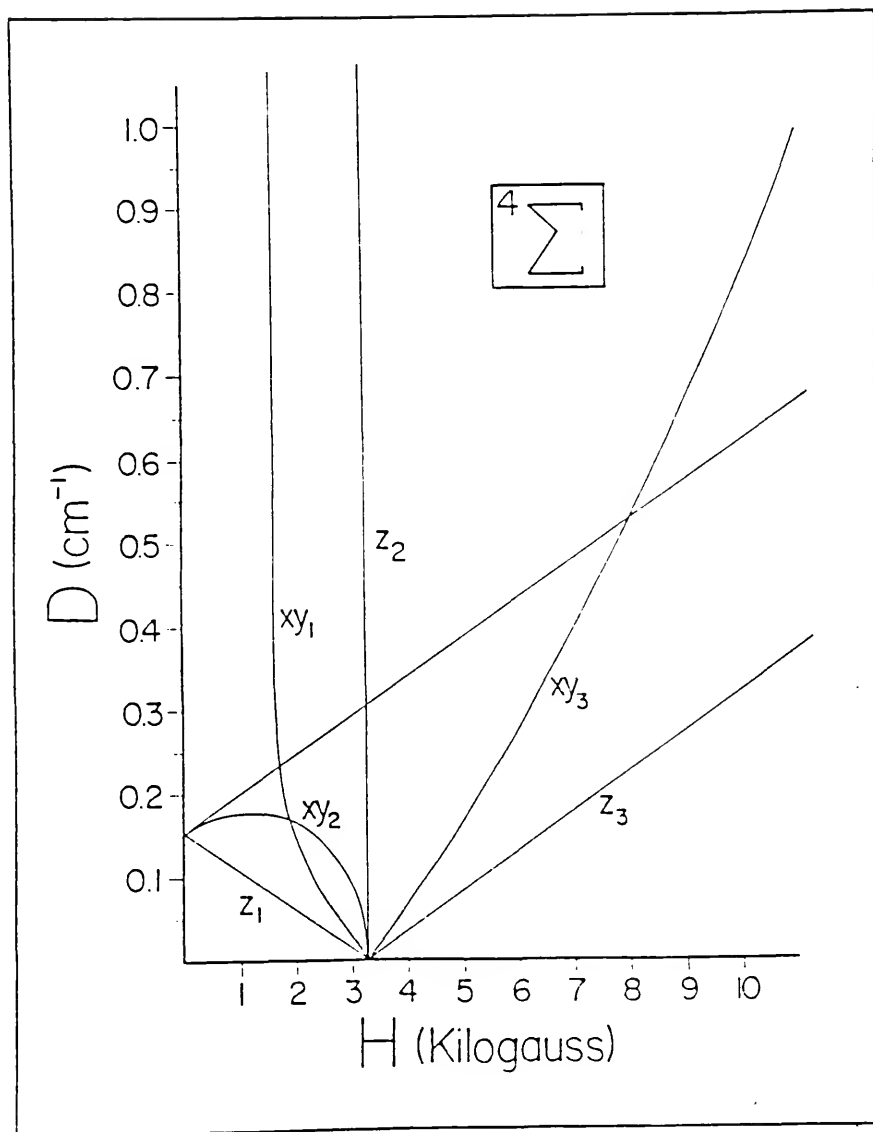


Figure I-9. Resonant fields of a  $^4\Sigma$  molecule as a function of the zero field splitting.

transitions are indicated between the same two levels at 690 and 1840 G. The reason for this can be seen in Figure I-9. The  $xy_2$  line is shown as an arc which reaches a maximum at about 1000 G.

### Sextet Sigma Molecules

The molecules considered here will have  $S=5/2$ , axial symmetry (at least a three-fold symmetry axis), and a large D. Ions such as  $Fe^{3+}$  and  $Mn^{2+}$  fall in this category in some coordination complexes.

### The spin Hamiltonian

The spin Hamiltonian for a  $^6\Sigma$  molecule with axial symmetry can be given as

$$(I-83) \quad \{H\}_{Spin} = g_{\parallel} \beta H_Z \{S\}_Z + g_{\perp} \beta H_X \{S\}_X \sin \theta \\ + D((\{S\}_Z)^2 - 35/12)$$

including all angles. For  $\theta = 0^\circ$  all of the off diagonal elements are zero and the eigenvalues of the 6X6 matrix are given below;

$$(I-84) \quad E(\pm 5/2) = (10/3)D \pm (5/2)g_{\parallel} \beta H$$

$$(I-85) \quad E(\pm 3/2) = -(2/3)D \pm (3/2)g_{\parallel} \beta H$$

$$(I-86) \quad E(\pm 1/2) = -(8/3)D \pm (1/2)g_{\parallel} \beta H.$$



Three levels appear at zero field which are separated by  $2D$  and  $4D$ . Applying the magnetic field will split these into three Kramers' doublets, which diverge linearly with field at high fields and with slopes proportional to  $M_S$ .

A mixing of states occurs in the perpendicular case and no simple solution is possible. A direct solution is possible using a computer. This type of a solution has been done by Aasa (48), Sweeney and coworkers (49), and by Dowsing and Gibson (50). The eigenvalues of the  $6 \times 6$  matrix calculated by computer are shown in Figure I-10. The diagonalization of the secular determinant was done at many fields and at four angles. It is evident that the resonant field for some transitions is very dependent on the angle. The plot of zero field splitting versus the resonant field is given in Figure I-11. It was prepared by solution of the Hamiltonian matrix at many fields and  $D$  values for  $\theta$  equal to  $0^\circ$  and  $90^\circ$ . For the situation where  $D \gg h\nu$  the  $xy_1$  line at  $g=6$  and the  $z_3$  line at  $g=2$  will be most easily observed. As can be seen in Figure I-10, these correspond to  $\pm 1/2$  transitions.

### Infrared Spectroscopy

Sir William Herschel discovered infrared radiation in 1800, but it was not until the turn of the century that infrared absorption investigations of molecules began (51).

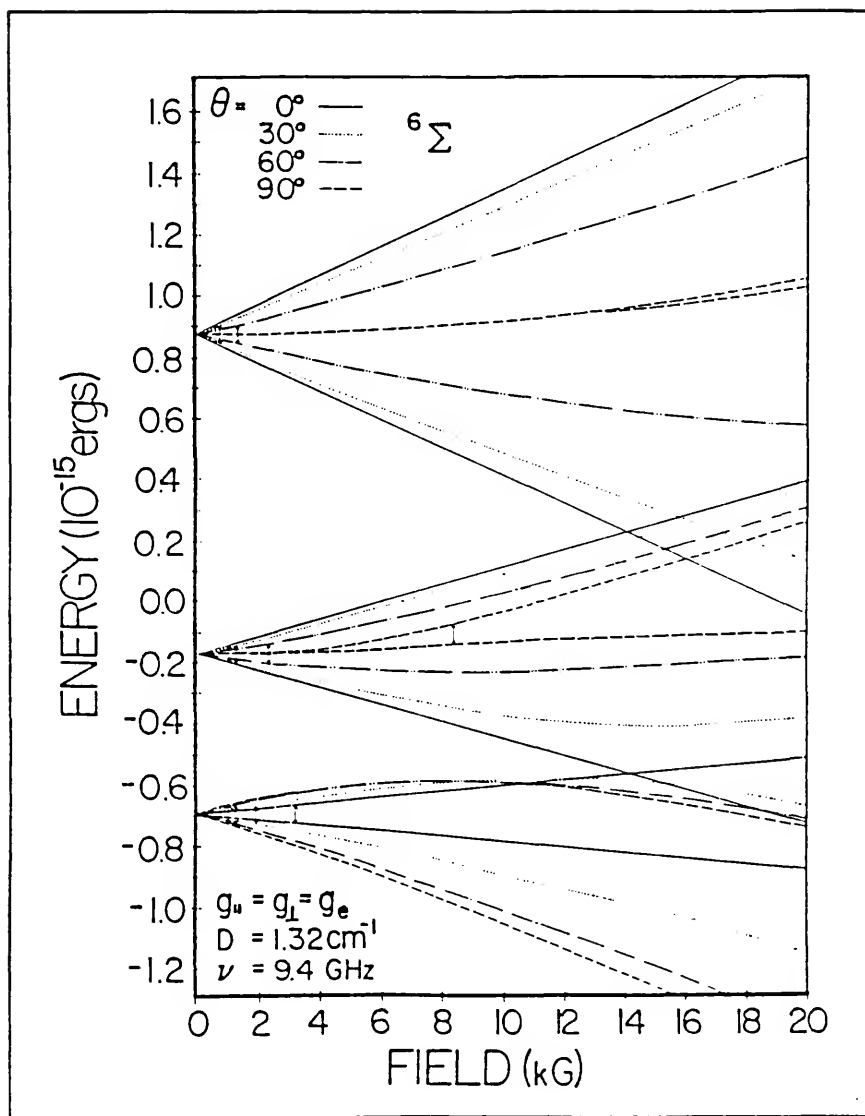


Figure I-10. Energy levels for a  ${}^6\Sigma$  molecule in a magnetic field for  $\theta = 0^\circ, 30^\circ, 60^\circ$ , and  $90^\circ$ .

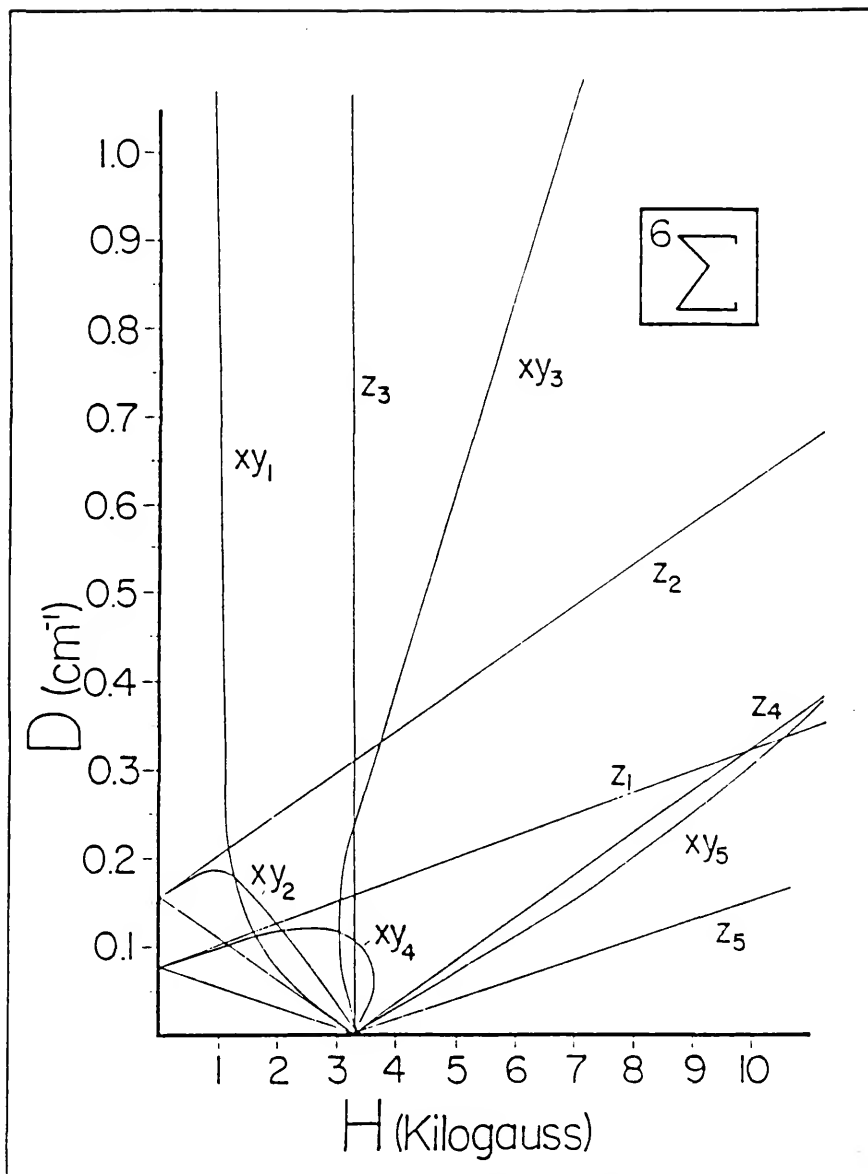


Figure I-11. Resonant fields of a  ${}^6\Sigma$  molecule as a function of the zero field splitting.

The typical IR source is a Nernst glower which is heated by passing electricity through it. The radiation, which is emitted over a continuous range by the source, is dispersed by using a prism, such as KBr, which is transparent over the range of interest. Various types of detectors ranging from thermocouples to photodetectors are used to analyze the light which has passed through the sample.

When dealing with infrared spectroscopy, one usually deals with three specific regions of the spectrum. The region from 800 to 2500 nm is the near infrared region and adjoins the visible region of the spectrum. The infrared region is found between 2500 to 50,000 nm. And the far infrared region borders the microwave region of the spectrum and starts at 50,000 nm and extends to about 1,000,000 nm. The far infrared region is used to analyze vibrational transitions of molecules containing metal-metal bonds, as well as the pure rotational transitions of light molecules. Most spectrometers are used in the mid-infrared region. This is where most molecular rotational and vibrational transitions occur (51).

### Theory

Since infrared spectra are due to the vibration and rotations of molecules, a brief review of the theory may be useful. When a particle is held by springs between two fixed points and moved in the direction of one of the fixed points,

it is constrained to move linearly. A restoring force develops as the particle is moved farther from its equilibrium position. The springs want to return to their equilibrium position. Hooke's law states that the restoring force is proportional to the displacement.

$$(I-87) \quad f = kx$$

where  $k$  is a constant of proportionality and called the force constant. The displacement is given by  $x$ , and the restoring force is  $f$ . The force constant is used as a measure of the stiffness of the springs. When the particle is released after the displacement, it undergoes vibrational motion. The frequency of oscillation can be written as

$$(I-88) \quad \nu = (1/2\pi)(k/m)^{0.5}$$

where  $m$  is the mass of the particle. The frequency can also be expressed in wavenumbers ( $\text{cm}^{-1}$ ) by dividing the right side of the equation with the speed of light. Because we are dealing with small particles (atoms in this case), it is necessary to enter into a quantum mechanical description of the oscillation. The allowed energy values are given by

$$(I-89) \quad E_v = (v + (1/2))h\nu,$$

where  $\nu$  is found in Eq.(I-88) and  $v$  is the vibrational quantum number. The equation above tells us that the energy of the harmonic oscillator can have values only of positive half-integral multiples of  $h\nu$ . The energy levels are evenly spaced, and the lowest possible energy is  $(1/2)h\nu$  even at absolute zero (52).

If one analyzes the vibrational behavior of a simple molecular system, such as a diatomic molecule, the system's oscillatory motion will be nearly harmonic and the frequency of the motion can be described by

$$(I-90) \quad \nu(\text{cm}^{-1}) = (1/2\pi c)(k/\mu)^{0.5}$$

where  $\mu$  is the reduced mass of the particles and is defined as

$$(I-91) \quad \mu = (m_1 m_2) / (m_1 + m_2).$$

Since the motion of the atoms is not completely harmonic, we must look at the energy levels of an anharmonic oscillator. This is given by

$$(I-92) \quad E_v = (v + (1/2))h\nu - (v + (1/2))^2 h\nu x_e \\ + (v + (1/2))^3 h\nu y_e \dots$$

where the constants  $x_e$ ,  $y_e$ , ... are anharmonicity constants.

These are small and typically positive and usually of the magnitude  $|x_e| > |y_e| > |z_e| > \dots$  (53).

Anharmonicity in a molecule allows transitions to be observed which are called overtones. These are transitions between  $v=0$  and  $v=2$  or  $v=3$  which are designated the first and second overtones, respectively. The first overtone is usually found at a frequency which is a little less than twice the fundamental frequency. Combination bands can also arise. These are caused by the sum or difference of two or more fundamentals.

The force constant for a molecule is related to the bond strength between the atoms. The force constant for a molecule containing a multiple bond is expected to be larger than the force constant of a single bond. A large force constant is also usually indicative of a strong bond. For diatomic molecules there is a good correlation between  $(k)^{0.5}$  and  $\nu(\text{cm}^{-1})$ . This relationship unfortunately does not hold for polyatomic molecules. In this case force constants must be calculated by a normal coordinate analysis of the molecule. Several authors have presented detailed descriptions of this method (51-54).

The vibrations of a molecule depend on the motions of all of the atoms in the molecule. To describe the location of the atoms relative to each other one looks at the degrees of freedom of the molecule. In a molecule with  $N$  atoms,  $3N$  coordinates are required to describe the location of all of

the atoms (3 coordinates for each atom). The position of the entire molecule in space (its center of gravity) is determined by 3 coordinates. Three more degrees of freedom are needed to define the orientation of the molecule. Two angles are needed to locate the principal axis and 1 to define the rotational position about this axis. For a linear molecule the rotation about the molecular axis is not an observable process. The number of vibrations of a polyatomic molecule is given then by

$$(I-93) \quad \text{number of vibrations} = 3N - 6$$

for a nonlinear molecule and

$$(I-94) \quad \text{number of vibrations} = 3N - 5$$

for a linear molecule.

What is observed in an infrared spectrum is usually a series of absorptions. These correspond to various stretching and bending frequencies of the sample molecule. In order for an infrared transition to be observed, there needs to be a change in the dipole moment of the molecule when it undergoes a stretching or bending motion. The strongest bands are those corresponding to the selection rule

$$(I-95) \quad \Delta v_k = \pm 1 \quad \text{and} \quad \Delta v_j = 0$$



where  $j$  does not equal  $k$  and  $k$  equals 1, ...,  $3N-6$ .

The most intense absorptions are those from the ground vibrational level since that is typically the most populated level. These type of transitions are called fundamental frequencies. These frequencies differ from the equilibrium vibrational frequencies,  $\nu_{1,e}$ ,  $\nu_{2,e}$ , ... . The fundamental frequencies are the ones generally used in force constant calculations because the available information is typically not sufficient to allow the calculation of anharmonicity constants. The fundamental frequencies of the molecule need not be the most intense absorptions. This can happen if the change in dipole moment,  $(\delta d / \delta Q_k)$ , is small or zero (51).

The phase or environment that the molecule is in will affect the appearance of the IR spectrum. With gas phase samples it is often possible to resolve the rotational fine structure of the compound using high resolution instruments. On the other hand, when dealing with a matrix isolated sample, there usually is not much, if any, rotational fine structure even under high resolution. This is because the molecule is rigidly held (small molecules such as HCl exhibit a rotational spectrum due to a hindered rotation within the matrix site) within the lattice of the matrix, and is not able to rotate freely as it is able to do in the gas phase. The elimination of the rotational fine structure simplifies the spectrum and enables the analysis of more complicated

vibrational spectra which arise when studying larger molecules.

### Fourier Transform IR Spectroscopy

The basic components of an FTIR instrument are an infrared source, a moving mirror, a stationary mirror, and a beamsplitter. The source in a typical FTIR spectrometer is a glower which is heated to about 1100 °C by passing an electrical current through it. The beam from the glower is directed to a Michelson interferometer where the intensity of each wavelength component is converted into an ac modulated audio frequency waveform. Assuming that the source is truly monochromatic, a single frequency,  $\lambda/c$ , hits the beamsplitter, where half is transmitted to the moving mirror and half to the fixed mirror. The two components of the light will return in phase only when the two mirrors are equidistant from the beamsplitter. In this case constructive interference occurs and they reinforce each other. Destructive interference occurs when the moving mirror has moved a distance of  $\lambda/4$  from the zero position. This means that the radiation which goes to the moving mirror will have to travel  $\lambda/2$  further than the radiation that went to the fixed mirror, and the two will be 180° out of phase. As the components go in and out of phase, the sample and the detector will experience light and dark fields as a function

of the mirror traveling  $+x$  or  $-x$  from its zero position. The intensity at the detector can be expressed as

$$(I-96) \quad I(x) = B(\nu) \cos(2\pi x \nu),$$

where  $I(x)$  is the intensity,  $B(\nu)$  is the amplitude of frequency  $\nu$ , and  $x$  is the mirror distance from the zero position. For a broadband source the signal at the detector will be the summation of Eq.(I-96) over all frequencies, and the output, as a function of mirror movement  $x$ , is called an interferogram (53).

The interferogram can then be converted into the typical intensity versus frequency spectrum by performing a Fourier transformation. The signal is transformed from a time domain signal, which arises from the motion of the mirror, to a frequency domain signal which is observed in the typical IR spectrum. This can be done mathematically by using

$$(I-97) \quad C(\nu) = \int I(x) \cos(2\pi x \nu) dx,$$

where  $C(\nu)$  is the intensity as a function of frequency.

There are several advantages in using an FTIR instrument. The detector in a Fourier transform instrument gets the full intensity of the source without an entrance slit. This yields a 100 fold improvement over the typical prism and grating instrument. The signal to noise ratio is

theoretically improved by a factor of  $M^{1/2}$ , where  $M$  is the number of resolution elements. This has been termed Fellgett's advantage since it results mathematically from one of his derivations. A direct result of Fellgett's advantage is that a dispersive instrument requires 3000 seconds to collect a spectrum, whereas an interferometer needs only about 60 seconds to collect an IR spectrum with the same signal to noise ratio. ( $M$  equals about 3000 and the observation time is about 1 sec/element) (53).

A complete IR investigation, when possible, can enable one to determine the structure of the molecule of interest. The IR spectrum allows one to determine force constants of the various bonds and from that information the bond strengths can be determined. The bending frequencies even enable one to determine the bond angle between the atoms involved in the bending motion. The shift in both stretching frequencies and bending frequencies caused by the substitution of isotopes into a molecule is very useful towards this purpose since the amount of the shift is dependent on the change in mass when the isotope is substituted into the molecule.

## CHAPTER II METAL CARBONYLS

### ESR of $\text{VCO}_n$ Molecules

#### Introduction

Transition-metal carbonyl molecules continue to be of great interest, partially because of their relevance to catalysis. The simplest molecules, those containing only one metal atom, have been studied spectroscopically, and electron spin resonance (ESR) has been applied successfully in some cases, specifically to  $\text{V(CO)}_4$ ,  $\text{V(CO)}_5$  (55),  $\text{V(CO)}_6$  (56-59),  $\text{Mn(CO)}_5$  (60),  $\text{Co(CO)}_3$ ,  $\text{Co(CO)}_4$  (61,62),  $\text{CuCO}$ ,  $\text{Cu(CO)}_3$  (63,64), and  $\text{AgCO}$ ,  $\text{Ag(CO)}_3$  (65,66). (Ionic carbonyls have also been observed via ESR (67,68) but will not be explicitly discussed here.) Theoretical discussions of the geometries, ground states, and bonding in these types of molecules have been given by several authors beginning perhaps with Kettle (69) and then by DeKock (70), Burdett (71,72), Elian and Hoffmann (73), and Hanlan, Huber, and Ozin (74). Although a number of ab initio calculations have been made on such carbonyls, the vanadium molecules considered here apparently have not been treated in detail.

The background for the present investigation was provided by the matrix work of Hanlan, Huber, and Ozin (74) who observed the infrared spectra of  $\text{V(CO)}_n$  where  $n$  equals 1

to 5, in the solid rare gases. Most notably, those authors concluded, from experiment and theory, that [1] VCO is nonlinear, [2]  $V(CO)_2$  exists in linear, cis, and trans forms in all three matrices, argon, krypton, and xenon, [3]  $V(CO)_3$  is probably of  $D_{3h}$  trigonal planar geometry. It should be emphasized that the supporting theory usually assumed low-spin ground states.

Morton and Preston have prepared  $V(CO)_4$  and  $V(CO)_5$  in krypton matrices by irradiation of trapped  $V(CO)_6$ . From ESR they assign  $V(CO)_4$  as a high-spin  $^6A_1$  in tetrahedral ( $T_d$ ) symmetry and  $V(CO)_5$  as  $^2B_2$  with distorted trigonal bipyramid ( $C_{2v}$ ) symmetry. The  $V(CO)_6$  molecule is a well known stable free radical which has been rather thoroughly researched by infrared (75), MCD (76), ultraviolet (77), electron and X-ray diffraction (78), and ESR. It is presumably a Jahn-Teller distorted octahedral ( $^2T_{2g}$ ) molecule at low temperatures leading to a  $^2B_{2g}$  ground state.

Our ESR findings are only for  $V(CO)_n$ , where n equals 1 to 3, and are not always in agreement with conclusions from optical work and semiempirical theory. The most explicit departure is in finding that VCO and  $V(CO)_2$  are high-spin molecules.

#### Experimental

The vanadium carbonyls synthesized in this work were made in situ by co-condensing neon (Airco, 99.996% pure), argon (Airco, 99.999% pure), or krypton (Airco, 99.995% pure)

doped with 0.1-5 mol%  $^{12}\text{CO}$  (Airco, 99.3% pure) or  $^{13}\text{CO}$  (Merck, 99.8% pure) with vanadium metal [99% pure, 99.8%  $^{51}\text{V}(I=7/2)$ ] onto a flat sapphire rod maintained at 4-6 K but capable of being annealed to higher temperatures.

The furnace, Heli-Tran, and IBM/Bruker X-band ESR spectrometer have been previously described (79). Vanadium was vaporized from a tungsten cell at 1975 °C, as measured with an optical pyrometer (uncorrected for emissivity).

### ESR Spectra

#### VCO

Two ESR spectra of the VCO molecule were observed in matrices prepared by condensing vanadium into CO/argon mixtures at 4 K. We designate these two forms of VCO below as (A) and (a). This symbolism is derived from one of their distinguishing features: one has a considerably larger  $^{51}\text{V}$  hyperfine splitting (hfs) than the other. Only the (a) form survived after annealing the argon matrices and only it appeared in a krypton matrix. Only (A) was observed in solid neon.

#### $^{51}\text{VCO(A)}$ and $^{51}\text{VCO(a)}$ in argon

Upon depositing vanadium metal into an argon matrix doped with 1.0 mol%  $^{12}\text{CO}$ , we obtained the 4 K ESR spectrum shown in Figure II-1. The two sets of eight strong, sharp lines centered near 1200 G could be attributed to separate

species since upon annealing one set [designated by (A)] disappeared. The hyperfine splitting (hfs) in the perpendicular  $xy_1$  and  $xy_3$  lines of the (A) species due to  $^{51}\text{V}(I=7/2)$  is approximately 100G, whereas that in the (a) species is about 60 G. The line centered at about 8100 G has been observed with that intensity only once, but its appearance, and disappearance upon annealing, correlates best with the (A) molecule. Its complex hfs is indicative of an off-principal axis line where forbidden  $\Delta m_1$  not equal to zero transitions can also occur. The observed lines of both (a) and (A) are listed in Tables II-1 and II-2.

Annealing to 16 K and quenching to 4 K converted the VCO (A) species into (a) which has the spectrum in argon in Figure II-2. Again the  $xy_1$  and  $xy_3$  lines have the same hfs, now about 60 G, and an "extra" line appears but centered at about 6700 G.

#### $^{51}\text{V}^{13}\text{CO}$ (A) and $^{51}\text{V}^{13}\text{CO}$ (a) in argon

These same spectra can be observed when  $^{13}\text{CO}$  replaces  $^{12}\text{CO}$  and the effect upon the  $xy_1$  line, which is the same effect for (A) and (a), is shown in Figure II-3. Each line is split into a doublet separated by about 6 G, indicating most importantly that there is only one CO in each species.

#### $^{51}\text{VCO}$ (A) in neon

In neon only one VCO molecule appears to be trapped, the one designated as (A) in argon with the hfs of about



Table II-1. Observed and calculated line positions  
(in G) for VCO ( $X^6\Sigma$ ) in conformation (A)  
in argon at 4 K. ( $\nu = 9.5596$  GHz)

$M_I(^{51}\text{V})^a$	$xy_1$		$xy_3$		Extra lines $\theta = 10^\circ$	
	Obs.	Calc.	Obs.	Calc.	Obs.	Calc.
7/2	797	789	5065	5082	7906	7897
5/2	882	877	5154	5170	8015	8012
3/2	974	971	5254	5262	8119	8124
1/2	1072	1072	5364	5360	8252	8234
-1/2	1174	1176	5473	5463	8346	8344
-3/2	1282	1285	5584	5573	8467	8453
-5/2	1396	1400	5692	5689	--	8562
-7/2	1511	1519	5819	5814	--	8671

$\Delta M_I = \pm 1$  transitions

Derived Parameters		Obs.	Calc.
$g_{\parallel}$	2.002(37)	7944	7938
$g_{\perp}$	1.989(5)	7976	7970
$ A_{\parallel}(^{51}\text{V}) $	247(28) MHz	8054	8052
$ A_{\perp}(^{51}\text{V}) $	288(6) MHz	8083	8083
$ D $	0.603(2) $\text{cm}^{-1}$	8161	8164
$A_{\text{iso}}(^{51}\text{V})^a$	274(13) MHz	8192	8194
$A_{\text{dip}}(^{55}\text{V})^a$	-14(11) MHz	8252	8274
$ A_{\perp}(^{13}\text{C}) $	17(3) MHz	8304	8304
		8380	8384
		8423	8413
		--	8493
		8514	8521
		--	8603
		--	8630

<sup>a</sup> Assuming  $A_{\parallel}$  and  $A_{\perp}$  are positive

( ) Error of the reported value

Table II-2. Observed and calculated line positions  
(in G) for VCO ( $X^6\Sigma$ ) in conformation (a)  
in argon at 4 K. ( $\nu = 9.5596$  GHz)

$M_I(^{51}\text{V})^a$	$xy_1$		$xy_3$		Extra lines $\theta = 12^\circ$	
	Obs.	Calc.	Obs.	Calc.	Obs.	Calc.
7/2	940	940	4460	4461	6449	6448
5/2	1000	999	4520	4520	6530	6526
3/2	1061	1060	4581	4580	6603	6603
1/2	1124	1124	4645	4644	6684	6680
-1/2	1191	1190	4710	4709	6756	6755
-3/2	1258	1257	4777	4777	6828	6831
-5/2	1326	1327	4847	4847	6906	6907
-7/2	1396	1398	4918	4921	--	6983

$\Delta M_I = \pm 1$  transitions

Derived Parameters		Obs.	Calc.
$g_{\parallel}$	2.002(10)	6476	6479
$g_{\perp}$	1.998(3)	6502	6496
$ A_{\parallel}(^{51}\text{V}) $	165(14) MHz	6563	6556
$ A_{\perp}(^{51}\text{V}) $	183(1) MHz	6590	6573
$ D $	0.452(2) $\text{cm}^{-1}$	6637	6633
$A_{\text{iso}}(^{51}\text{V})^a$	177(5) MHz	6665	6650
$A_{\text{dip}}(^{51}\text{V})^a$	-6(5) MHz	6711	6709
$ A_{\perp}(^{13}\text{C}) $	17(3) MHz	--	6726
		6782	6785
		6804	6802
		6857	6861
		6887	6877
		6934	6937
		--	6953

<sup>a</sup> Assuming  $A_{\parallel}$  and  $A_{\perp}$  are positive.

( ) Error in the indicated value

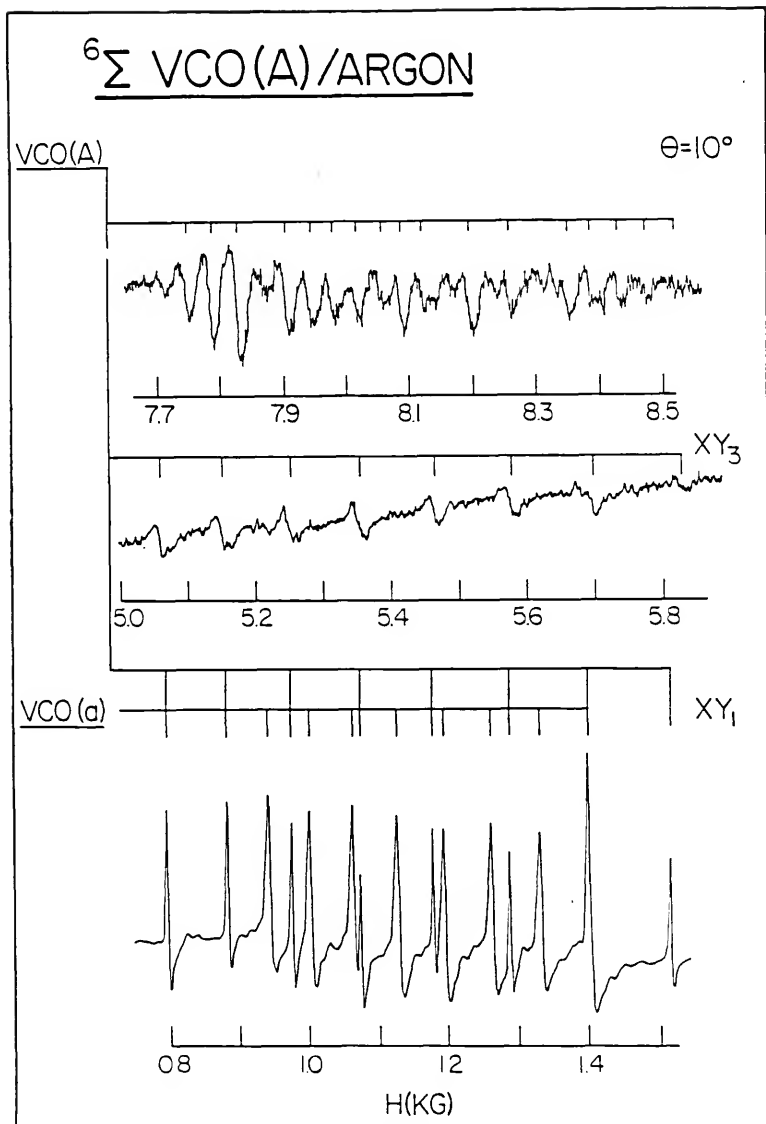


Figure II-1. ESR spectrum of an unannealed matrix at 4 K containing  ${}^{51}\text{VCO(A)}$ , with hfs of about 100 G, and  ${}^{51}\text{VCO(a)}$ , with hfs of about 60 G. For the conformation (A) two perpendicular lines and an off principle axis line are shown.  $\nu = 9.5585$  GHz.

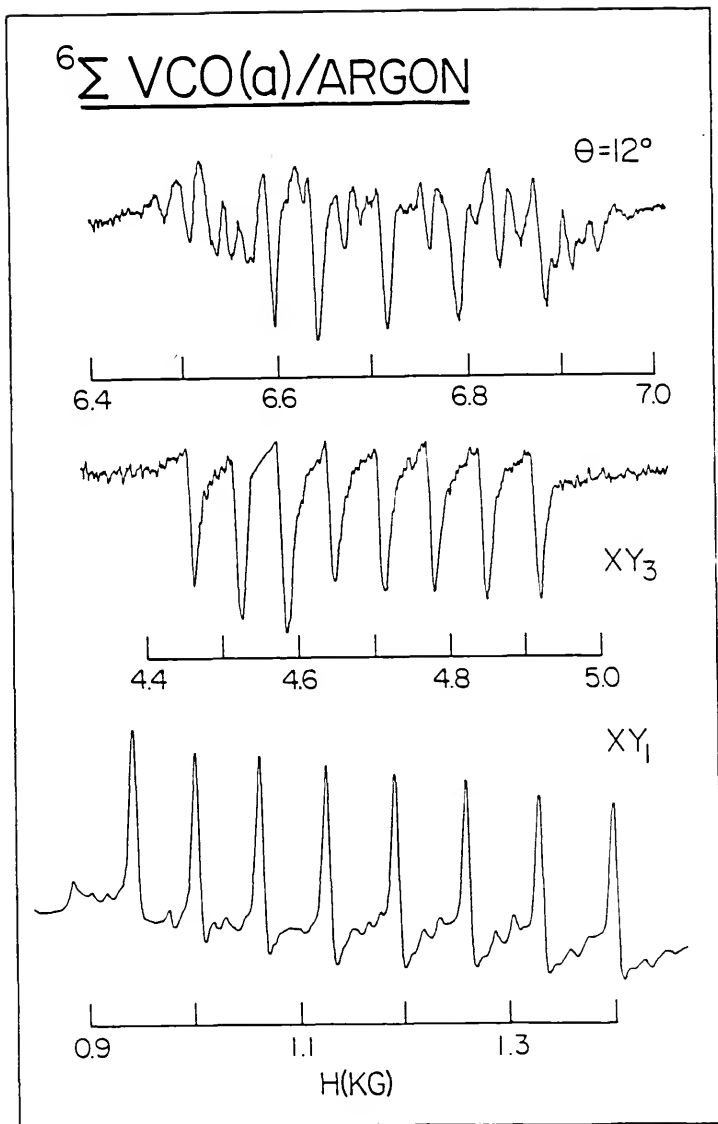


Figure 11-2. ESR spectrum of an annealed argon matrix at 4 K containing only  ${}^{51}\text{VCO}$  in conformation (a). Two perpendicular lines and off principal axis line are shown.  $\nu = 9.5585$  GHz.

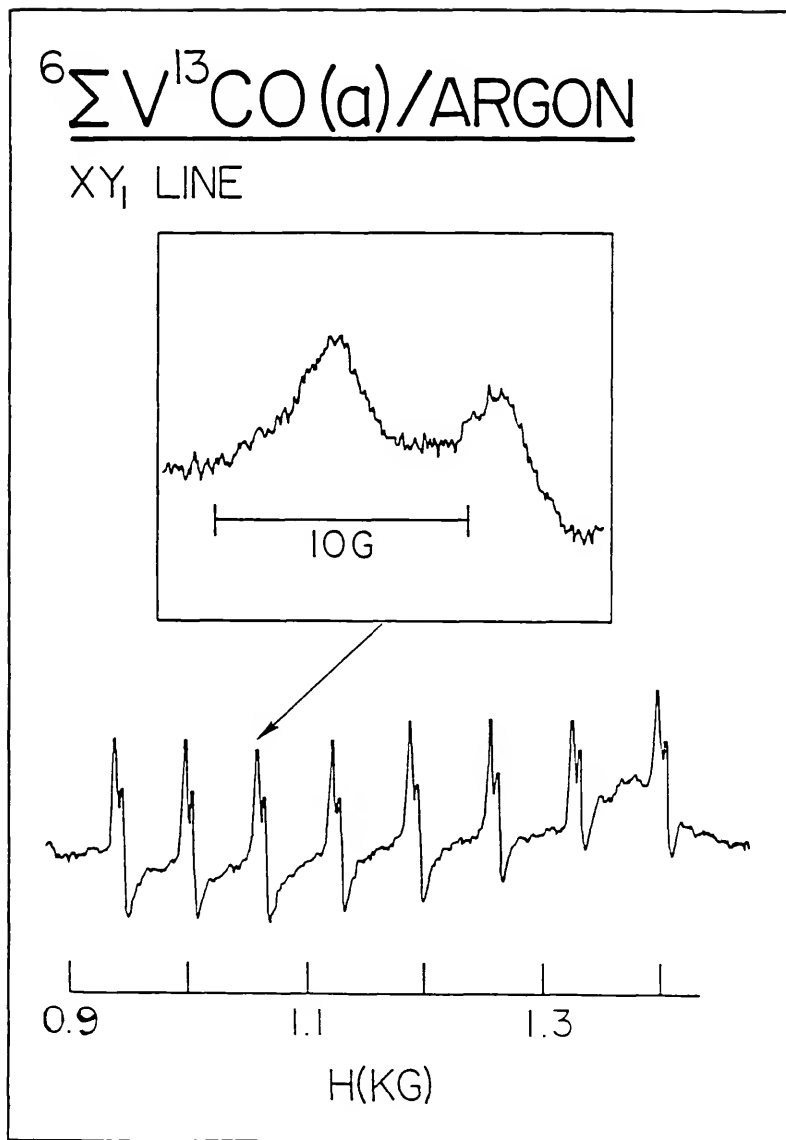


Figure II-3. ESR spectrum of the perpendicular  $xy_1$  line of  ${}^{51}\text{V}{}^{13}\text{CO}$  in conformation (a) in an argon matrix at 4 K.  $\nu = 9.5531$  GHz.

100 G. The ESR spectrum when vanadium was trapped in neon doped with 0.1%  $^{12}\text{CO}$  is shown in Figure II-4 and the observed lines are listed in Table II-3. Again the  $xy_1$  line is centered at about 1200 G. but the center of the  $xy_3$  fine-structure line is difficult to determine. This is because the intensity of the spectrum is lower than in argon, and the lines appear to be split by site structure which is apparently more exaggerated in the high-field line. The off principal axis line was not detected in neon. Annealing is difficult in neon matrices, and it only led to loss of the matrix here. At CO concentrations higher than 0.1% this spectrum was not observed, presumably because the higher carbonyls were formed in this lower melting solid.

#### $^{51}\text{VCO(a)}$ in krypton

Before annealing there are two series of eight lines of about equal intensity, each with about 60 G hfs. one centered at about 1138 G and the other at about 1170 G at 4 K. When the sample was annealed to about 30 K, only the series centered at about 1170 G (extending from 967 to 1392 G) remained sharp at 4 K.

#### $^{51}\text{V}(^{12}\text{CO})_2$ and $^{51}\text{V}(^{13}\text{CO})_2$ in neon

With CO/Ne concentrations of 0.1%. in addition to VCO(A), two additional fine-structure lines appeared centered at about 1800 and 6400 G with  $^{51}\text{V}$  hyperfine splittings of

about 60 G. This spectrum, assigned to  $V(CO)_2$  molecules, is shown in Figure II-5 and the observed lines are listed in Table II-4. With incorporation of  $^{13}CO$ , the line widths appear to be almost the same, perhaps broadened by no more than 20%. As with the monocarbonyl this spectrum is not observed in neon at higher CO concentrations. It has also not been observed in argon with any of the CO concentrations used, which varied from 0.1% to 5%, nor has it been formed by extensive annealing of any argon matrix.

$^{51}V(^{12}CO)_3$  and  $^{51}V(^{13}CO)_3$  in neon

Using concentrations of 0.1 to 1.0% in neon gave a complex signal extending from 3000 to 3500 G containing a pattern of eight strong hyperfine lines centered about  $g = 2.12$  with  $A(^{51}V) = 50$  G (see Figure II-6 and Table II-5). There are also two very weak signals at 2948 and 3008 G (not shown) and two at 3560 and 3643 G which appear clearly in Figure II-6. These weaker lines did not appear to have the same intensity variation from matrix to matrix as the strong features and using  $^{13}CO$  essentially doubled the width of the eight strong lines. The region between about 3430 and 3530 G becomes approximately one broad line with phase down, indicating a broadening of each of the narrow  $^{12}CO$  lines by a factor of at least three. Even with extensive annealing this spectrum was not observed in argon matrices.

Table II-3. Observed line positions (in G) for VCO ( $X^6\Sigma$ ) in conformation (A) in neon at 4 K.  
( $\nu = 9.5560$  GHz).

$M_I(^{51}\text{V})$	$xy_1$
7/2	796(5)
5/2	885
3/2	976
1/2	1074
-1/2	1177
-3/2	1286
-5/2	1398
-7/2	1514



Table II-4. Observed and calculated line positions (in G)  
for  $V(CO)_2$  ( $X^4\Sigma_g^-$ ) isolated in neon at 4 K.  
( $\nu = 9.5560$  GHz)

$M_I(^{51}V)^a$	$xy_1$		$xy_3$	
	Obs.	Calc.	Obs.	Calc.
7/2	1586(5)	1586	6136	6140
5/2	1646	1646	6199	6198
3/2	1707	1707	6259	6259
1/2	1766	1769	6324	6321
-1/2	1830	1833	6387	6385
-3/2	1896	1898	6452	6451
-5/2	1960	1965	6522	6519
-7/2	2030	2032	6597	6589

Derived Parameters

$g_{\perp}$	1.9908(9)
$ D $	0.2995(5) $cm^{-1}$
$ A_{\parallel}(^{51}V) $	132(56) MHz
$ A_{\perp}(^{51}V) $	178(3) MHz
$A_{iso}(^{51}V)^a$	163(21) MHz
$A_{dip}(^{51}V)^a$	-15(20) MHz
$ A_{\perp}(^{13}C) $	$\leq 42$ MHz

<sup>a</sup> Assuming  $A_{\parallel}$  and  $A_{\perp}$  are positive.

Table II-5. Calculated and observed line positions (in G) and magnetic parameters of  $V(CO)_3$  molecule in a neon matrix at 4 K. ( $\nu = 9.55498$  GHz)

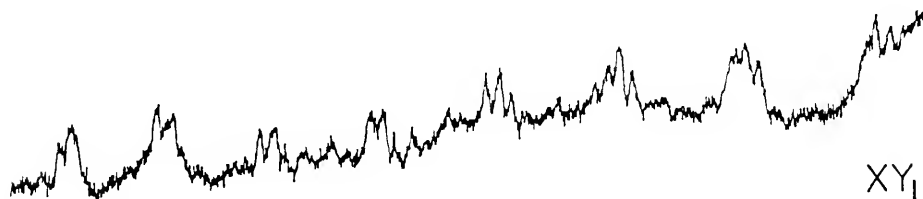
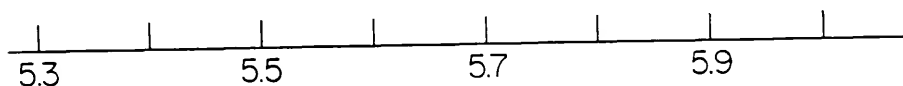
$M_I^a$	Perpendicular Lines		Parallel Lines	
	Obs.	Calc.	Obs.	Calc.
$+7/2$	3067(3)	3068	3358(?)	3356
$+5/2$	3117	3118	--	3373
$+3/2$	3167	3168	3395(?)	3391
$+1/2$	3218	3218	3411(5)	3410
$+1/2$	3269	3269	3433(5)	3430
$+3/2$	3321	3321	3451(3)	3451
$+5/2$	3373	3373	3472	3472
$+7/2$	3425	3425	3495	3495

Derived Parameters	
$g_{\perp}$	2.1024(9)
$g_{\parallel}$	1.9923(9)
$ A_{\parallel}^{(51V)} $	55(3) MHz
$ A_{\perp}^{(51V)} $	150(3) MHz
$ A_{iso}^{(51V)} ^a$	82(3) MHz
$ A_{dip}^{(51V)} ^a$	68(2) MHz

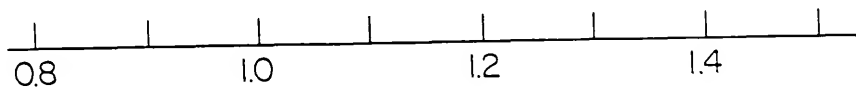
<sup>a</sup> Assuming  $A_{\parallel}$  and  $A_{\perp}$  are of opposite sign.

${}^6\Sigma$  VCO(A)/NEON

$XY_3$



$XY_1$



H(KG)

Figure II-4. ESR lines in a neon matrix at 4 K attributed to  ${}^{51}\text{VCO}$  in conformation (A).  $\nu = 9.5560$  GHz.

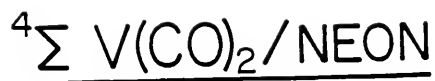
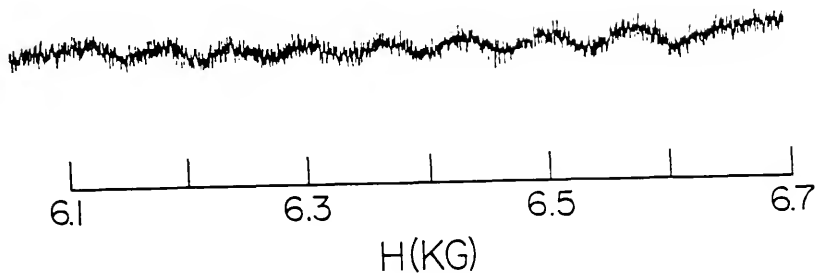
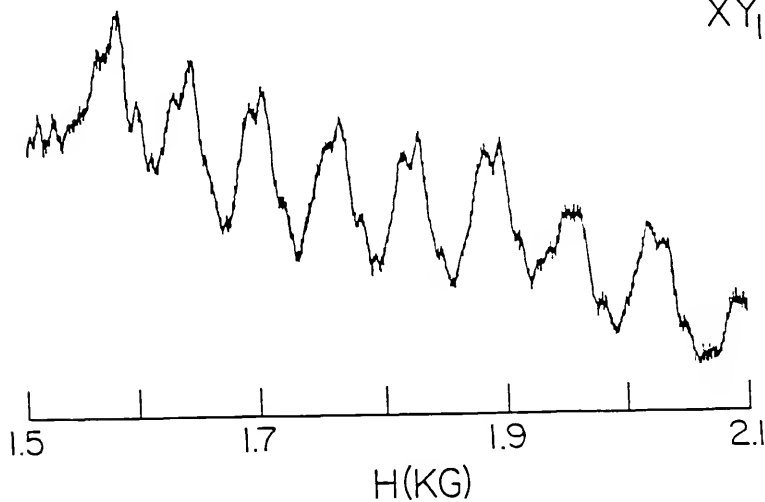

 $XY_3$ 

 $XY_1$ 


Figure II-5. ESR lines in a neon matrix at 4 K attributed to  ${}^{51}V(CO)_2$ .  $\nu = 9.5560$  GHz.

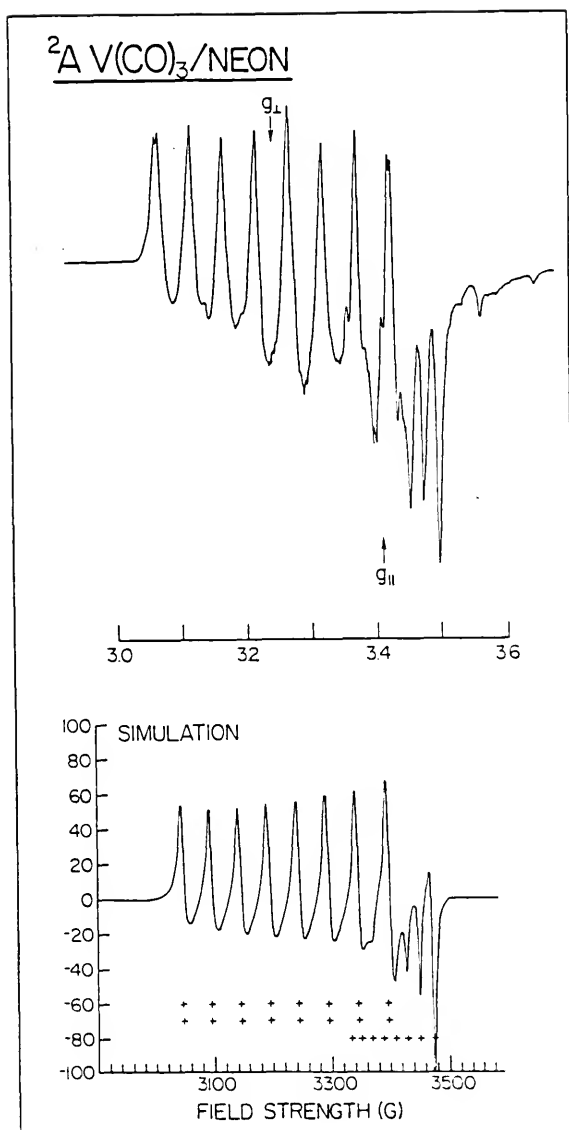


Figure II-6. (Top) ESR spectrum near  $g=2$  in a neon matrix at 4 K attributed to an axial  $^{51}V(CO)_3$  molecule.  $\nu = 9.5584$  GHz. (Bottom) Simulated spectrum using  $g$ ,  $A(^{51}V)$  parameters and linewidths given in the text.

### Analysis

#### VCO, (A) and (a)

The low-field fine structure line of each of these molecules has an effective  $g_e \approx 6$  and each may then be assigned a sextet sigma ground state. This is in accord with the further analysis shown in Tables II-(1-3). The  $xy_1$  line at about 1100 G in each case corresponds to the transition within the Kramers doublet ( $M_S = +1/2 \leftrightarrow -1/2$ ). The other lines in argon diverge further for the two species, indicating that their zero-field splitting (zfs) parameters are quite different; as the tables show these are 0.60 and  $0.45 \text{ cm}^{-1}$  for (A) and (a), respectively, in argon. Although the hfs in neon indicates that the trapped molecule there is (A), there was insufficient data for analysis. The same was true of the krypton spectra; however in that matrix the hfs identified the trapped molecules as (a), presumably in two sites before annealing.

The two perpendicular-line positions in argon yield good values of  $|b_2^0| = |D|$  and  $g_{\perp}$  for (A) and (a), and in principle  $g_{\parallel}$  could then be determined reliably from high-field extra lines in each case if the  $b_4^0$  parameter is neglected in the spin Hamiltonian for these presumably linear molecules (80):

$$\begin{aligned}
 \text{(II-1)} \quad H = & g_{\parallel} \beta H_Z S_Z + g_{\perp} \beta (H_X S_X + H_Y S_Y) + b_2^0 [S_Z^2 - (1/3)S(S+1)] \\
 & + A_{\parallel} I_Z S_Z + A_{\perp} (I_X S_X + I_Y S_Y) + (1/60) b_4^0 [35 S_Z^4 \\
 & - 30 S(S+1) S_Z^2 + 25 S_Z^2 - 6 S(S+1) + 3 S^2 (S+1)^2]
 \end{aligned}$$

where  $b_2^0 = D$  and the hyperfine parameters here refer to  $^{51}\text{V}(I=7/2)$ . The  $b_4^0$  parameters have been determined for at least two axial high-spin molecules (81,9) and, although they were small, they had a pronounced effect upon the positions of high-field lines. This may not be the case here but it makes the establishment of  $g_{\parallel}$  uncertain. However, neglecting  $b_4^0$ , one finds  $g_{\parallel}$  values of 2.039 (A) and 2.012 (a), with the admittance of forbidden  $\Delta M_I = \pm 1$  transitions, gave reasonable fits to the lines. For  $S = 5/2$ ,  $I = 7/2$ , the above Hamiltonian generates a  $48 \times 48$  spin matrix which was diagonalized to obtain eigenvalues and thereby magnetic parameters which best fit the observed transitions at the resonance frequency. If interaction with the quadrupole moment of the  $^{51}\text{V}$  nucleus ( $-0.05b$ ) is involved then the coupling constant must be less than 14 MHz (A) and 6 MHz (a). These  $g_{\parallel}$  values are large, and it seemed more reasonable to see if a fit could be made with  $g_{\parallel} = g_e$ . This necessitated a slight alteration in the  $A_{\parallel}$  hyperfine parameter, which is very uncertain in any case, but the approximate fit of the "extra-line" transition shown in Tables II-1 and II-2 could be made. This leaves the  $g_{\parallel}$  and  $b_4^0$  parameters in considerable doubt.

There is no doubt about both of these molecules being VCO since the  $^{51}\text{V}$  and  $^{13}\text{C}$  hfs clearly established that. The spectra appear to be those of linear molecules since the perpendicular lines are narrow and any splitting would have to be very small. However, as can be seen from the lines at about 1200 G in Figure II-1, the widths of the VCO(a) lines, while still quite narrow (about 8 G), are about twice as wide as those of the (A) form. This may be significant in suggesting an unresolved splitting in the (a) molecule lines (see below). It is also possible that the molecules are bent but appear linear because they are rotating about axes of least moment of inertia. However, the similarity of the spectra in three matrix environments may be evidence against such motional averaging.

### V(CO)<sub>2</sub>

The same Hamiltonian applies to a linear V(CO)<sub>2</sub> as was used for VCO except that  $S = 3/2$  instead of  $5/2$ . Again neglecting  $b_4^0$ , one solves a 32 X 32 eigenvalue problem to arrive at the parameters given in Table II-4. With only perpendicular fine structure lines observed, only  $g_{\perp}$ , assuming  $|D|$ , could be derived.

### V(CO)<sub>3</sub>

Because of the complexity of the spectrum in Figure II-6 near  $g = 2.0$ , a simulation program for  $S = 1/2$  utilizing



second-order perturbation theory (82) was employed to derive the magnetic parameters. The final fit shown in the bottom of that Figure used the following parameters:  $g_x = g_y = 2.1189$ ,  $g_z = 2.0057$ ;  $A_x = A_y = 148.0$  MHz,  $A_z = 56.0$  MHz; linewidths  $W_x = W_y = 25$  MHz,  $W_z = 12$  MHz for Lorentzian line shapes;  $\nu = 9.5584$  GHz. To further confirm these derived parameters, exact diagonalization of the matrix was done, yielding almost the same results, as shown in Table II-5.

There was concern about the weak lines at low and high fields mentioned earlier in that perhaps they were part of the  $V(CO)_3$  spectrum which implies a nonaxial molecule. However, attempts to simulate the spectrum with all  $g$  and all  $A$  components distinct were not successful. Also, the observation that the intensities of these weak lines appeared to vary relative to the strong ones when the CO concentrations were varied, implied that the two sets of lines belonged to separate molecules. A possible source of the weak lines is  $V_2CO$ , although, from the triplet sigma ground state of  $V_2$  (12), one might expect the carbonyl to also be triplet (or singlet), but a fit to an  $S = 1$  molecule appears unlikely. It is not the spectrum attributed to  $V(CO)_4$  which is a "derivative-shaped line at  $g = 1.9583$ " in Kr, and it did not grow but diminished in relative intensity with increasing CO/Ne concentration.

## Discussion

### VCO

Both molecules observed at  $g_e \approx 6$  in unannealed argon matrices are established as VCO by the  $^{51}\text{V}$  and  $^{13}\text{C}$  hyperfine structure observed. The sharpness of the lines and the lack of additional features indicate that their  $g$  tensors are nearly axial and the molecules are therefore close to linear. Trapping in neon and krypton provides no evidence to the contrary and makes the possibility of axial spectra due to molecular rotation, as mentioned earlier, unlikely.

Vanadium atoms have a  $3d^3 4s^2 \ ^4F$  ground state but the  $3d^4 4s \ ^6D$  state lies only about  $2000 \text{ cm}^{-1}$  (83) higher. Thus, it is not difficult to justify  $S = 5/2$  for the VCO molecule. The ten valence electrons of CO plus the five of vanadium fill the levels, as indicated in Figure II-7, such that the  $3\sigma$  and  $1\pi$  provide the shared orbitals. (Figure II-7 was derived from a similar Figure for NiCO given by DeKock and Gray (84).) The five unpaired spins are then essentially 3d orbitals on vanadium with some hybridization of the  $3d\sigma$  with the  $4s\sigma$  and  $4p\sigma$ , and with some small population of CO orbitals. This orbital picture is corroborated by the observed hfs, as will be discussed below. It is also in accord with the energy level scheme described by Hanlan et al. (74), but here corrected to the high-spin case.

The unusual aspect of the VCO molecule is the appearance of two forms of the molecule in argon, designated

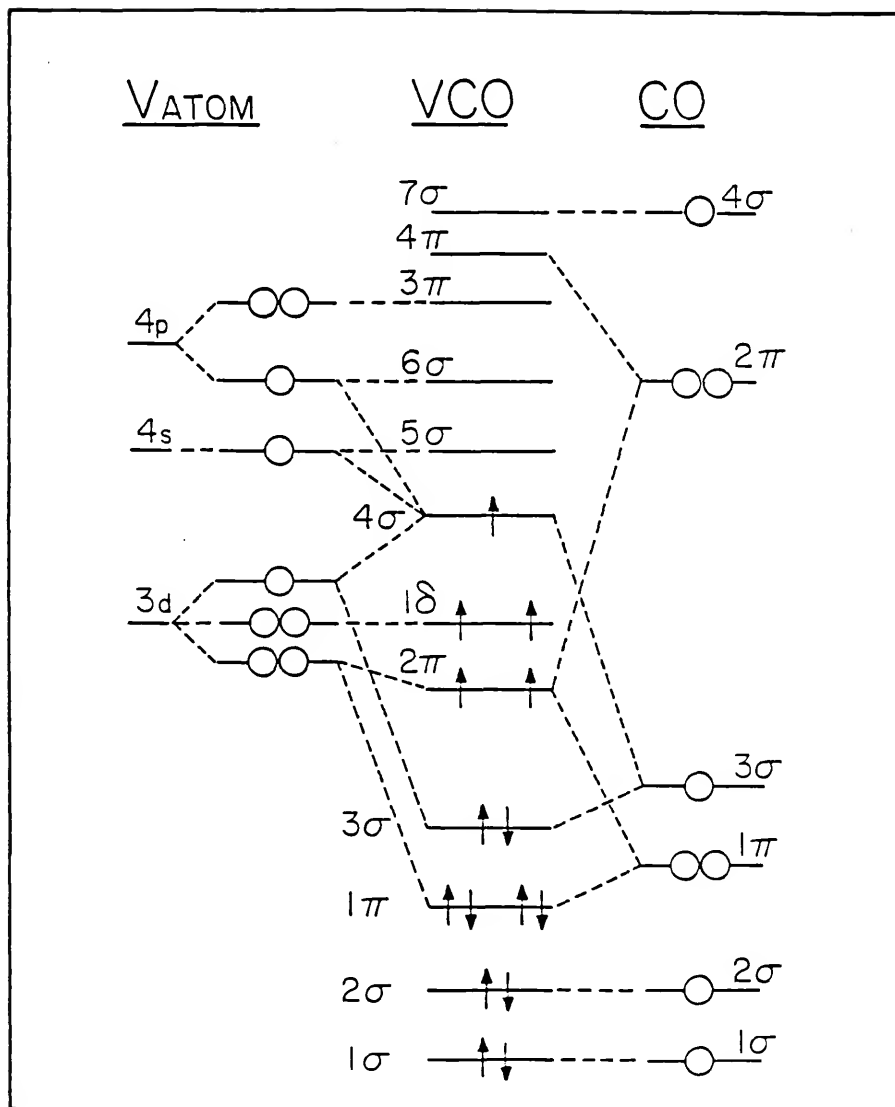


Figure II-7. Molecular orbital scheme for the  ${}^6\Sigma$  VCO molecule (modeled after Fig. 5-43 in DeKock and Gray(84)).

as (A) and (a) here, with only form (A) appearing in neon and only form (a) in krypton. The (A) form of the molecule is characterized by  $|D| = 0.60 \text{ cm}^{-1}$  and  $|A|(^{51}\text{V})| = 288 \text{ MHz}$  and (a) by  $|D| = 0.45 \text{ cm}^{-1}$  and  $|A|(^{51}\text{V})| = 183 \text{ MHz}$ , as given in Tables II-1 and II-2. The derived values of  $A_{\text{iso}}(^{51}\text{V})$  in the two cases, although less exact, also lie in that order: for (A) it is 274 MHz and for (a) 177 MHz. For a  $(d\pi)^2(d\delta)^2(s\sigma)^1$  configuration one would derive from  $^{51}\text{V}$  atomic data (85)  $A_{\text{iso}} = 1/5 \times 4165 = 833 \text{ MHz}$ , and comparison with the two above values yields the unpaired  $\sigma$  electron in VCO as 33% (A) and 21% (a) s character. The remainder of the  $\sigma$  character in each case is then 3d and 4p, and the values of  $A_{\text{dip}}$  can also be considered in this way. Since  $(\sigma d, \pi d)$  and  $\delta d$  contributions to  $A_{\text{dip}}$  have opposite signs, the small value of that parameter in both VCO molecules can then be accounted for. For example, for molecule (A) and assuming  $s\sigma + p\sigma$  hybridization

$$\begin{aligned} \text{(II-2)} \quad A_{\text{dip}}(\text{A}) &= [2/5(1/7 - 2/7) + 1/5 \cdot 0.67 \cdot 2/5] \cdot 438 \\ &= -2 \text{ MHz} \end{aligned}$$

where 438 MHz is the atomic radial factor (81), as compared to the observed value of -14 (55) MHz.

Only  $A_{\perp}(^{13}\text{C}) = 6 \text{ G}$  was definitely observed but there is no indication of distinct  $A_{\parallel}(^{13}\text{C})$  splittings (see Figure III-3) so that the  $A(^{13}\text{C})$  tensor of VCO may be assumed to be

approximately isotropic. Then, accounting for the 2S spins, one finds that the s character at  $^{13}\text{C}$  is only  $5.6 \cdot 2.8 / 3777 = 0.02$ , where the atomic  $A_{\text{iso}}$  factor for  $^{13}\text{C}$  is from Morton and Preston's table (85). (Corresponding values in  $\text{Cu}^{13}\text{CO}$  and  $\text{Ag}^{13}\text{CO}$  were  $\rho_S = 0.0510$ , and  $\rho_S = 0.01$ ,  $\rho_P = 0.0212$ , respectively.) Spin density on the CO ligand is then apparently quite small, although of course measurements of the hfs at the oxygen nucleus are needed to confirm that presumption.

The effective distortion of these approximate  $3d^5$  electrons from spherical symmetry leads to both the large zfs parameters and the shifts in the g components from  $g_e$ . If the orbital angular momentum in the ground state is coupled to the same excited states to produce  $|D|$  and g then one should find that (86)

$$(II-3) \quad D = +\lambda/2[g_{\parallel} - g_{\perp}]$$

where  $\lambda$  is the spin-orbit coupling constant of the vanadium atom with  $S = 5/2$ . The spin-orbit coupling constant,  $\lambda$ , is difficult to estimate for a  $d^5$  vanadium but might be taken the same as for  $\text{Cr}^+$  as  $190/5 = 38 \text{ cm}^{-1}$  so that

$$(II-4) \quad D = +19[2.002 - 1.989] = +0.25 \text{ cm}^{-1}$$

as compared to  $0.60 \text{ cm}^{-1}$  observed.

The idea that VCO (A) and (a) might be isomeric VCO and VOC can be dismissed because  $A_{\perp}(^{13}\text{C})$  is the same for both forms. One would expect quite different spin densities on  $^{13}\text{C}$  for these isomers. Of course, the ESR spectra, particularly in the absence of spin density information on oxygen, cannot eliminate the possibility that VOC and not VCO is being observed, but bonding considerations indicate that the metal-carbon bond is favored.

Earlier it was noted that the line widths differ for the two forms in Figure II-1. The increase in line width of (a) could be due to a slight bending of VCO in that form. This implies that a third g tensor component and a second zero-field parameter, E, are strictly required in the analysis of the VCO (a) spectra, but the effect is too small to make any significant change in the analysis. However, if (a) is a bent form of (A), the electronic parameters are very sensitive to angle, since the zfs and  $A(^{51}\text{V})$  are considerably lowered and the g tensor made more isotropic. (This concomitant decrease in  $|D|$  and  $g_{\perp}-g_{\parallel}$  is in accord with Eq. II-1.) A decrease in s $\sigma$  character in the bent molecule is not unexpected since it implies decreased s $\sigma$  + p $\sigma$  hybridization which in the linear molecule helps to lower the energy by placing some unpaired spin density on the side of the metal atom away from the CO.

Then one can understand the detection of two forms of VCO if the V-CO potential energy curve is relatively flat

with two shallow, but apparently distinct, minima. A rationale for the preference of particular forms (A) or (a) for particular matrices or matrix conditions might be given as follows: If (A) contains the more distorted vanadium, as judged by the larger s hybridization and larger zfs, then it is understandable that it would be the form found in unannealed strained sites in argon and in neon where the sites are smaller and less accommodating. Upon annealing, the (a) form becomes the preferred species in argon, presumably now being surrounded by a more relaxed environment. It is then reasonable that this form would also be found in solid krypton where the sites are larger than in argon. If asked which form would VCO take in the hypothetical gas phase at 4 K, one would choose (a), the bent  ${}^6A$  molecule.

If the V-CO bond is relatively weak, then the CO stretching frequency would be expected to be relatively high, as Hanlan et al. (74) have observed. However, in an unannealed argon matrix one might also expect to observe two C-O stretching frequencies from VCO (A) and (a). These apparently were not observed by those authors, but perhaps this could be the result of differences in experimental conditions during preparation of the matrices (74), since the sapphire rod was always cooled by liquid helium in these ESR studies, or perhaps to the low concentrations of CO used here.

V(CO)<sub>2</sub>

The molecule observed here definitely contains only one vanadium atom, but the number of attached CO's is not definite since only line broadening was observed when <sup>13</sup>CO was substituted. However, the addition of one CO molecule to S = 5/2 VCO can be expected to lower the spin to S = 3/2. The only possible evidence of any nonlinearity in the molecule is the small splittings of about 10 G on each of the xy hyperfine lines in neon (see Figure II-5), but this could also be due to multiple sites in the matrix. With the lower spin, the molecule also has lower values of |D| = 0.30 cm<sup>-1</sup> and A<sub>iso</sub>(51) = 160 MHz compared to the monocarbonyl. The spin density, ρ<sub>S</sub>, at the vanadium nucleus is calculated to be 160·3/4165 = 0.12, considerably smaller than in VCO.

Although the ESR spectra are not definitive, it seems very likely from the observed quartet multiplicity that the molecule is at least slightly bent. If the usual σ bonding and π back-bonding (84) applies to each attached CO so that a completely double-bonded structure is obtained, then one can only assume the unpaired spins to be essentially (dδ)<sup>3</sup> which would yield only a doublet state. Bending the molecule avoids this problem since it removes the degeneracies in the d orbitals. Then the about 10 G splitting in the lines could be due to a small zero-field splitting E term. If the bent symmetry is C<sub>2v</sub> then the ground electronic state might be <sup>4</sup>B<sub>2</sub>. Our observations are not in agreement with the IR



assignments in Ar, Kr, and Xe matrices (74) where the presence of three forms of the molecule was inferred.

### V(CO)<sub>3</sub>

As with V(CO)<sub>2</sub>, the assignment of the spectrum to a tricarbonyl is somewhat arbitrary since <sup>13</sup>CO substitution only led to broadening of each of the <sup>51</sup>V hyperfine lines. However, the molecule does contain only one vanadium atom, and the spectrum does not correspond to any of those observed for the higher carbonyls (55-59). There is no ambiguity in the analysis of the spectrum as that of a doublet axial molecule with  $\Delta g_{\perp}$  large and positive. The parameters are reminiscent of a d<sup>9</sup> Cu<sup>2+</sup> ion with the unpaired spin in a d<sub>z</sub><sup>2</sup> orbital in a distorted octahedron (88). A similarly large g tensor anisotropy is found for the linear CuF<sub>2</sub> molecule. Here, of course, the molecule is considered as planar D<sub>3h</sub> or pyramidal C<sub>3v</sub> with its lowest state being <sup>2</sup>A<sub>1</sub>" or <sup>2</sup>A<sub>1</sub>. The addition of four more CO electrons to VCO has resulted in lowering the spin to S = 1/2.

No matter what the relative signs of A<sub>||</sub> and A<sub>⊥</sub>, the small percent s character at the vanadium atom (<3%) implies that the unpaired electron occupies an almost pure d<sub>z</sub><sup>2</sup> orbital and that the molecule is probably of planar D<sub>3h</sub> symmetry. Then A<sub>dip</sub> should be about 2/7.438 = +125 MHz. If the observed A<sub>⊥</sub> is chosen as negative and A<sub>||</sub> as positive, A<sub>dip</sub> = (A<sub>||</sub> - A<sub>⊥</sub>)/3 = +68 MHz, which is of the right sign but

half the calculated magnitude perhaps indicating a slightly higher spin density of CO in this molecule. This is in accord with the increased line width in  $V(^{13}\text{CO})_3$  relative to  $V(^{12}\text{CO})_3$ . One can, in fact, crudely justify about 50% of the spin population in three  $C(p\pi)$  orbitals if  $A_{\perp}(^{13}\text{CO}) = -50$  MHz and  $A_{\parallel}(^{13}\text{CO}) = -70$  MHz (from estimated line widths) since then one calculates  $A_{\text{dip}}(^{13}\text{C}) = -7$  MHz compared to  $0.50 \cdot (1/3) \cdot (-1/5) \cdot 268 = -9$  MHz, where the angular factor is from Morton and Preston (85).

The large  $g_{\perp}$  value must imply a low lying electronic state, presumably  $^2E_1$ , involving essentially excitation of (50% of) a  $d\pi$  electron into the  $d\sigma$  "hole". If the spin-orbit constant is taken as  $95 \text{ cm}^{-1}$  then one finds  $\Delta E(^2E_1 - ^2A_1) = 1400 \text{ cm}^{-1}$ . Such a low lying state can also be used, in conjunction with Topp's second-order theory (90), to yield  $g_{\parallel} = 1.9954$ , versus the observed 1.9923.

### Conclusion

The unexpectedly high spin  $S = 5/2$  and relatively large zero-field splitting ( $0.45 \text{ cm}^{-1}$ ) of VCO is decreased by each addition of a CO ligand, first to  $V(\text{CO})_2$  with a quartet ground state,  $|D| = 0.30 \text{ cm}^{-1}$ , and then to  $V(\text{CO})_3$  with probable  $D_{3h}$  symmetry and a  $^2A_1$  ground state. The VCO molecule has two conformations of almost equal stability, one is linear and the other slightly bent, with rather different electronic parameters. The deduced geometries of these

carbonyls are not in complete agreement with theory, but the latter does also not always explicitly consider high-spin cases.

## Infrared Spectroscopy of First Row Transition Metal Carbonyls

### Introduction

There has been considerable interest in the area of metal-carbonyls, in order to understand their bonding and their activity as catalysts. This type of molecule is also a prototype for chemisorption on metal surfaces. To understand these systems, it is first necessary to understand what occurs when a metal atom is bound to a single carbonyl group. Our work suggests that in order to form a first row transition metal carbonyl ( $\text{MCO}$ ), the  $4s$  orbital must be half empty. New data shows a good correlation between the strength of the metal carbonyl bond and promotion energies of a  $4s$  electron into a  $3d$  orbital. There are now a large number of theoretical papers concerning the electronic and bonding properties of these molecules (91).

### Experimental

The experiments were done using a standard infrared matrix set up. An Air Products DS-202 closed cycle helium refrigerator was used to cool the deposition window to about 12 K. The chromium and manganese carbonyls were made by

codepositing argon (Airco, 99.996% pure) doped with various amounts of  $^{12}\text{C}^{18}\text{O}$  (Airco, 99.3% pure). The amount of CO in the argon varied anywhere from one part in 1000 to one part in 100. Chromium (Spec flake, 100ppm max.) was heated in a tantalum cell at about 1260 °C measured using an optical pyrometer without making any corrections for emissivity. The manganese (Spex flake, metal impurities 100ppm max.) was heated in a tantalum cell which was resistively heated to the desired temperatures. Deposition temperatures varied from 950 °C to about 1300 °C (uncorrected for emissivity) depending on the concentration of manganese desired in the matrix. Deposition times were usually held to about 1 hour. The spectra were taken using a Nicolet 7100 Series FT-IR. Thirty-two scans were usually taken and added together in order to produce a spectrum.

### Spectra

Chromium (Figure II-7) and manganese (Figure II-8) were studied using FT-IR and stretching frequencies were obtained for  $\text{CrCO}$ ,  $\text{Mn}_x\text{CO}$ , and  $\text{Mn}_2\text{CO}$ . The product bands observed in these experiments were not in agreement with those previously reported (92,93). We feel that those reported here are the correct assignments for the carbonyls in question.

Although the product band at  $1850\text{ cm}^{-1}$  was previously thought to be the position of the CO stretch in the  $\text{MnCO}$

complex (92), concentration studies done by varying the concentration of Mn in the matrix, showed that this stretching frequency was not due to a single manganese atom attached to a carbonyl, but rather a carbonyl attached to an aggregate of manganese atoms because the product peaks grew in and became more intense as the concentration of manganese was increased. The amount of manganese was crudely gauged by the amount of metal which was deposited on the furnace heat shield. At low temperatures and when there was only a small amount of manganese in the matrix (no clusters), no product peaks were observed. It is interesting to note that previous work (13) done involving manganese showed a critical dependance on the temperature of the manganese cell and the amount of cluster formation. Manganese is rather unique in that it easily forms clusters. We were also unable to assign a definitive stretching frequency for the  $\text{MnCO}$  species since none of the observed product bands remained when the amount of manganese was decreased in the matrix, or decreased when the manganese concentration was increased.

The carbonyl stretching frequency of the  $\text{CrCO}$  molecule is in disagreement with previously reported results (Table II-6) (92,93). Again, the concentration of the chromium and the amount of CO doped into the matrix gas was varied. At low concentrations of both chromium and CO only one strong product peak at  $1977\text{ cm}^{-1}$  was observed (top trace, Figure II-8). This was assigned to the CO stretching frequency of

Table II-6. Carbonyl stretching frequencies for the  
first row transition metal carbonyls.

<u>Metal</u>	<u>cm<sup>-1</sup> (2)</u>
Scandium	--
Titanium	--
Vanadium	1890 <sup>a</sup>
Chromium	1977 <sup>b</sup>
Manganese	2140 <sup>c</sup>
Iron	1898 <sup>d</sup>
Cobalt	1952 <sup>a</sup>
Nickel	1996 <sup>e</sup>
Copper	2010 <sup>a</sup>

( ) Uncertainty in line position

-- good line positions are not available

<sup>a</sup> Ref. 92

<sup>b</sup> This work

<sup>c</sup> free carbonyl stretching frequency

<sup>d</sup> Ref. 91

<sup>e</sup> Ref. 70

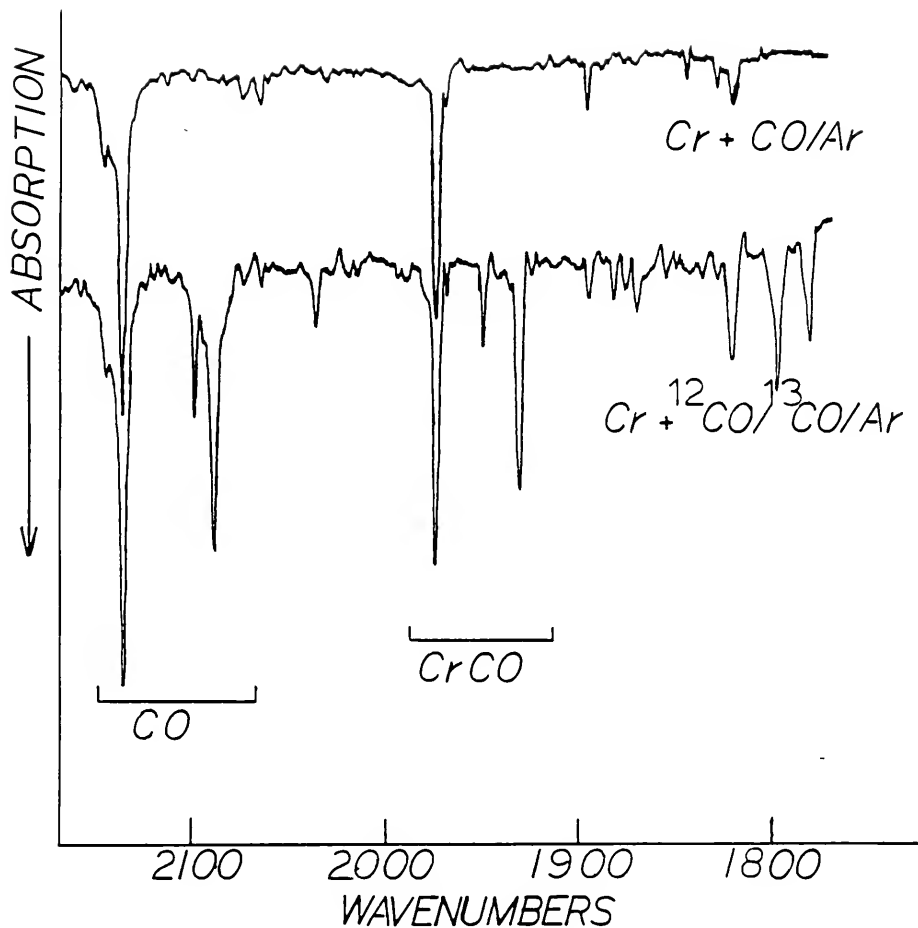


Figure II-8. Infrared spectrum of CrCO using both <sup>12</sup>CO and <sup>13</sup>CO in argon. The top trace has a 1:200 CO/Ar concentration and the bottom has a 1:1:200 <sup>12</sup>CO/<sup>13</sup>CO/Ar concentration.

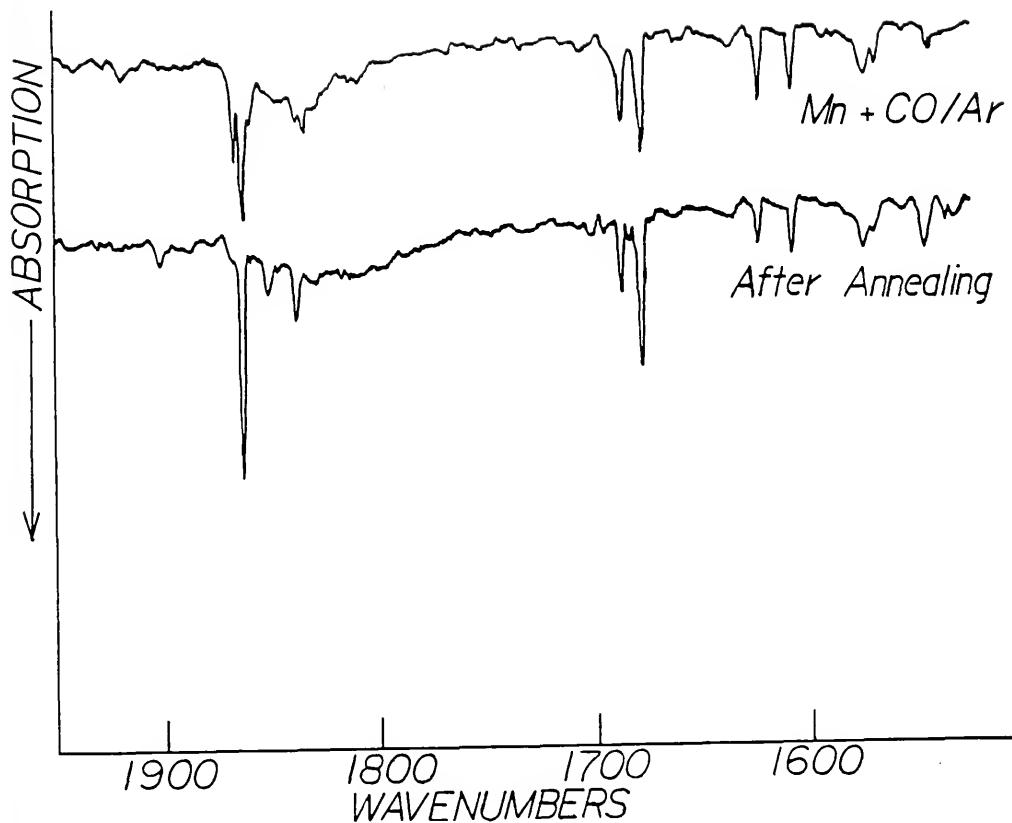


Figure II-9. Infrared spectrum of Mn and CO codeposited into an argon matrix. The bottom trace is after annealing the matrix to about 30 K and cooling back down to 14 K.



chromium monocarbonyl. When a 1:1 mixture of  $^{12}\text{CO}$  and  $^{13}\text{CO}$  in argon was used as the matrix gas, the bottom spectra was taken. A second strong peak at  $1928\text{ cm}^{-1}$  has grown in and was assigned to the CO stretch in the  $\text{Cr}^{13}\text{CO}$  molecule. The shift due to the carbon 13 isotope is on the order of what one would expect for this molecule. As the concentrations of both Cr and CO were increased, the intensity of the peaks due to the monocarbonyl decreased and other peaks such as the lines around  $1800\text{ cm}^{-1}$  grew in.

### Discussion

To understand how a metal bonds to a carbonyl, more data than vibrational frequencies are necessary. ESR is invaluable in giving this type of information, but unfortunately the only ESR data available for MCO type complexes of the first row transition metal carbonyls, are for VCO (94) and CuCO (64). Vanadium, which has a ground state electron configuration of  $4s^2 3d^3$ , forms a complex with a ground state electron configuration containing 5 unpaired electrons,  $4s^1 3d^4$ . It seems that promotion of a 4s electron is necessary in complex formation, when the 4s orbital is filled. The CuCO work also shows that the unpaired spin density in this molecule resides essentially in a 4s orbital.

In order to form first row transition metal carbonyls our data seems to indicate that the 4s orbital of the metal must be at least half empty. The reason for this is that,

since the 4s orbital projects about twice as far into space as the 3d orbital, having a filled 4s orbital would result in repulsion of the carbonyl rather than it being attracted to the metal. Having a half empty 4s orbital, would allow the carbonyl to be attracted to the metal, and gives the pair of electrons being donated by the carbonyl an available orbital. This gives a molecular orbital which contains three electrons, two in a bonding sigma orbital and one in the antibonding sigma orbital. The electron in the high energy sigma antibonding orbital will want to reside in a lower energy orbital, if possible, and will therefore go into a 3d orbital (91).

For seven of the first row transition metal carbonyls the first step in being able to form a metal carbonyl is the promotion of one of the 4s electrons into a 3d orbital. A look at how promotion energies (Figure II-10) vary across the row should predict, to a certain extent, how tightly bound the carbonyl will be to the metal. Also, the strength of interaction (Figure II-9), as shown by the CO stretch in the metal carbonyl, should vary with the promotion energy. The stronger the interaction between the metal and the CO, the lower the promotion energy for the metal, and the closer the CO frequency gets to the double bond value of  $1740\text{ cm}^{-1}$ .

The properties of first-row transition metals usually exhibit a characteristic "double hump". Our results hint at this, but do not clearly show this trait. Unfortunately,

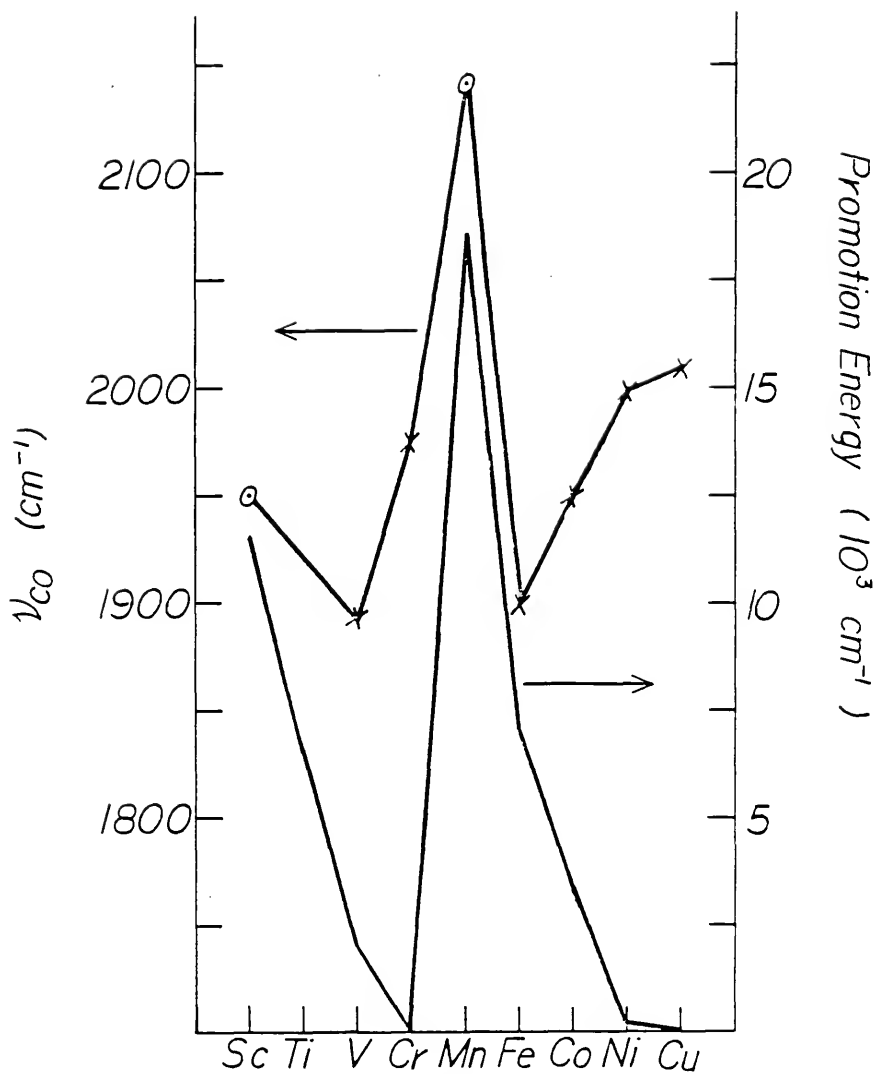


Figure II-10. Plot of the CO stretching frequencies in the first row transition metal monocarbonyl molecules MCO (circled points are tentative). Also shown is the variation of the energy of promotion corresponding to  $4s^2 3d^{n-2}$  to  $4s^1 3d^{n-1}$ , where  $n$  is the number of valence electrons(91).

looking at just the promotion energy is too simplistic. One also has to consider the pairing energy of electrons within the d orbitals, as well as the repulsion caused by having filled orbitals. From this, one would predict that vanadium forms the strongest metal carbonyl. This is because vanadium has a low energy of promotion for the 4s electron, no repulsion from filled d orbitals, and no pairing energy (Figure II-10). Chromium, which has a  $4s^1 3d^5$  ground state, is less tightly bound than vanadium or iron because of the pairing energy necessary when the electron in the sigma antibonding orbital goes into the 3d orbital, which is lower in energy. Manganese carbonyl is probably very weakly bound because of its very large promotion energy. The promotion energy is about twice that of any other first row transition metal carbonyl. This also explains the small difference in CO stretching frequencies between NiCO ( $4s^1 3d^9$ ) and CuCO ( $4s^1 3d^{10}$ ), since both have essentially filled d orbitals. The theory also correctly predicts that Fe will form the second most tightly bound first row transition metal carbonyl, because of its low pairing energy, low promotion energy, and a small amount of repulsion from a single filled d orbital.

The trends between promotion energies and carbonyl stretching frequencies of the metal carbonyls match up well for the first few metals. When one gets to chromium, pairing energies and repulsion from the filled d orbitals begin to

play a part in the bonding. Pairing of the first d electron will cost the most energy. One would expect that the bonding energies of nickel and copper carbonyl would be almost the same since they have no open d orbitals even if pairing were possible.

Theoretical studies have been done on  $\text{FeCO}$  (91) and  $\text{NiCO}$  (91). The iron-carbonyl study shows the low energy configuration of the molecule to have 4 unpaired electrons, which is in agreement with what is predicted by our theory. The  $\text{NiCO}$  study predicts either a triple or singlet state for the nickel carbonyl. The triplet state probably is lower in energy than the singlet state. Both of these theoretical studies predict promotion of one of the 4s electrons into a d orbital, in agreement with our scheme. The theory put forth here, also correctly predicts the number of unpaired electrons in the metal-carbonyl complex.

### Conclusion

From the ESR data it is obvious that a half filled 4s orbital is necessary in order to form the monocarbonyl. Also, we feel that  $\text{MnCO}$  is so weakly bound that the metal prefers to dimerize and polymerize before reacting successfully with the carbonyl. Using the new value obtained for  $\text{CrCO}$ , the graph of the CO stretching frequencies in the MCO complex is in good agreement with the plot of the promotional energies of the 4s electrons, and the plot

exhibits the feature that so many graphs of properties of the first row transition metals do, a double dip.

CHAPTER III  
ESR STUDY OF A SILVER SEPTAMER

Introduction

Silver is a Group IB metal and therefore it is expected that  $\text{Ag}_7$  would be the transition-metal counterpart of the known alkali-metal (Group IA),  $\text{Li}_7$ ,  $\text{Na}_7$ , and  $\text{K}_7$  clusters. In a series of classic electron spin resonance experiments Lindsay, et al., have generally established the electronic, magnetic, and structural properties of these clusters and also of  $\text{Li}_3$ ,  $\text{Na}_3$ , and  $\text{K}_3$  (95,96). Theory has agreed with those findings (97). (It is noteworthy that the pentamers within that series have not been detected (98).)

Correspondingly, the Group IB clusters  $\text{Cu}_3$ ,  $\text{Ag}_3$ , and  $\text{Au}_3$  were trapped in matrices by Howard, Mile, Sutcliffe, et al., and the ESR spectra revealed that their properties were very similar to those of the Group IA trimers (99-101). Those authors also report the detection and analyses of the ESR spectra of the pentamers  $\text{Cu}_5$ ,  $\text{Ag}_5$ ,  $\text{Cu}_2\text{Ag}_3$  (102,103), and  $\text{CuAg}_4$ . Although we have not investigated the copper containing clusters, the parameters for  $\text{Ag}_7$  given here, as obtained from an ESR spectrum in a solid neon matrix, are almost the same as those assigned to  $\text{Ag}_5$  by Howard, and

coworkers (103). This suggests that those authors were actually observing  $\text{Ag}_7$  and that the putative  $\text{Cu}_5$ ,  $\text{Cu}_2\text{Ag}_3$ , and  $\text{CuAg}_4$  clusters may also be septamers; however, that remains to be proven. (Also, recent theoretical calculations by Arratia-Perez and Malli do not support the proposed Jahn-Teller distortion of  $\text{Ag}_5$  from a trigonal bipyramidal structure (104).)

We have convincing experimental evidence that the cluster composed of seven silver atoms has the structure of a pentagonal bipyramid (Figure III-1) with the single unpaired electron spin predominantly confined to the two axial atoms. This structure is a section of an icosahedron and can be visualized as five slightly distorted tetrahedra meeting at an edge to form a decahedron, thereby having a pentagonal axis. Silver and gold particles of decahedral and icosahedral geometry were first observed by Ino using transmission electron microscopy (105). There has been considerable controversy over the internal strain and the compensating lower surface energy in these so-called "multiply-twinned particles" (MTPs) (106). Ino proposed a critical radius above which the icosahedral form of the particle would transform to the cubooctahedron. The silver septamer then corresponds to the smallest known MTP.

#### Experimental

Silver cluster molecules were formed by the co-condensation of neon (Airco, 99.996% pure) and silver



atoms on a sapphire or copper rod cooled to 4 K via a liquid helium Heli-Tran system. The ESR spectrometer and furnace assembly have also been previously described (79). Silver was vaporized from a silver wire wound on a 1.0 mm diameter tungsten wire resistively heated to about 925 °C, or in the case of isotopically enriched silver powder (99.26% atomic abundance of  $^{109}\text{Ag}$  from Oak Ridge National Laboratories), from a tantalum cell resistively heated to 1290 °C. Temperatures were measured with an optical pyrometer and were not corrected for surface emissivity. Deposition times were of the order of an hour with matrix gas flow rates of 12-18 mmole/hr. The matrices were not very stable and often inadvertently annealed themselves, resulting in the loss of trapped atoms and the formation of silver clusters.

#### ESR Spectra

Figure III-2 shows an ESR spectrum obtained of  $^{109}\text{Ag}$  enriched silver trapped in solid neon at 4 K after an inadvertent annealing in which most of the  $^{109}\text{Ag}$  atom signals near 3000 and 3700 Gauss (107) disappeared. Traces of those signals are seen on the low field lines centered at 3006 G in the Figure.

Figure III-3 shows the ESR spectrum from the same experiment, but before any annealing was done to the matrix. The extremely intense lines at about 3000 G are due to the  $M_I = 1/2$  transition of the  $^{109}\text{Ag}$  atoms. These lines completely

obscure the low field lines of the silver septamer. The other two sets of lines at 3237 G and 3476 G are clearly visible. It is not until the matrix has been annealed strongly (close to the melting point of neon) that the three sets of lines become clear (Figure III-2).

The four groups of lines indicated in Figure III-2 are produced by hyperfine interaction (hfi) of the one unpaired electron with two equivalent  $^{109}\text{Ag}$  ( $I=1/2$ ) nuclei. The hfi is large enough (about 240 G) that the second order effects lead to a small 17 G splitting of the central line (108). Each of the four lines consists of six hyperfine lines separated by 8.7 G with intensity ratios 1:5:10:10:5:1 (to within a few percent) corresponding to a much weaker hfi with five equivalent  $^{109}\text{Ag}$  nuclei. The intensities of the hf pattern in the central group of lines are accounted for as partial overlapping of two groups of six lines to yield eight lines with intensities in the ratio of 1:5:11:15:15:11:5:1 as indicated in Table III-1. Each of the eight central lines was examined on a greatly expanded scale of the magnetic field and at extremely low modulating fields in order to detect any splitting in the individual lines. None was detected. The linewidths in the central group were the same as those in the two outer groups, about 2 G FWHM. It must be reasoned that the second order splitting of 17 G is (fortuitously) almost exactly twice the hf splitting within

Table III-1. Calculated and observed ESR lines (in G) of  $^{109}\text{Ag}_7$  in solid neon at 4 K. ( $\nu = 9.5338$  GHz)

Observed Lines		Calculated Lines	
Relative Intensity <sup>a</sup>	Center of hf Pattern	$ J, M_J\rangle$	
1	2983.9(3)		2983.9
5	2992.5		2992.5
10	3001.4		3001.2
10	3009.9	3005.6 $ 1, 1\rangle$	3009.8
5	3018.6		3018.5
1	3026.8		3027.1
1	3214.0		3214.4
5	3223.0		3223.0
11	3231.6	3236.0 $ 1, 0\rangle$	3231.7/3231.6
15	3240.3		3240.3/3240.2
15	3248.9	3253.2 $ 0, 0\rangle$	3249.0/3248.9
11	3257.6		3257.6/3257.5
5	3266.2		3266.2
1	3274.8		3274.8
1	3462.2		3462.1
5	3470.7		3470.8
10	3479.6		3479.4
10	3488.1	3483.8 $ 1, -1\rangle$	3488.1
5	3469.9		3496.7
1	3505.5		3505.5

<sup>a</sup> Measured intensities are within 5% of those tabulated.

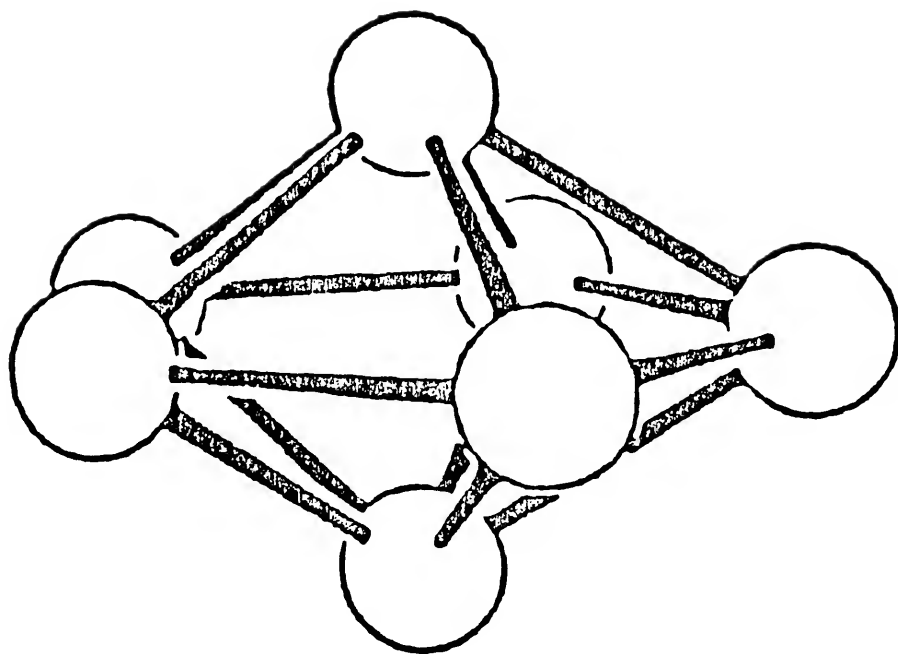


Figure III-1. The pentagonal bipyramid structure ascribed to  $\text{Ag}_7$  in its  $^2\text{A}_2$  ground state. It has  $\text{D}_{5h}$  symmetry with two equivalent atoms along the axis and five equivalent atoms in the horizontal plane.

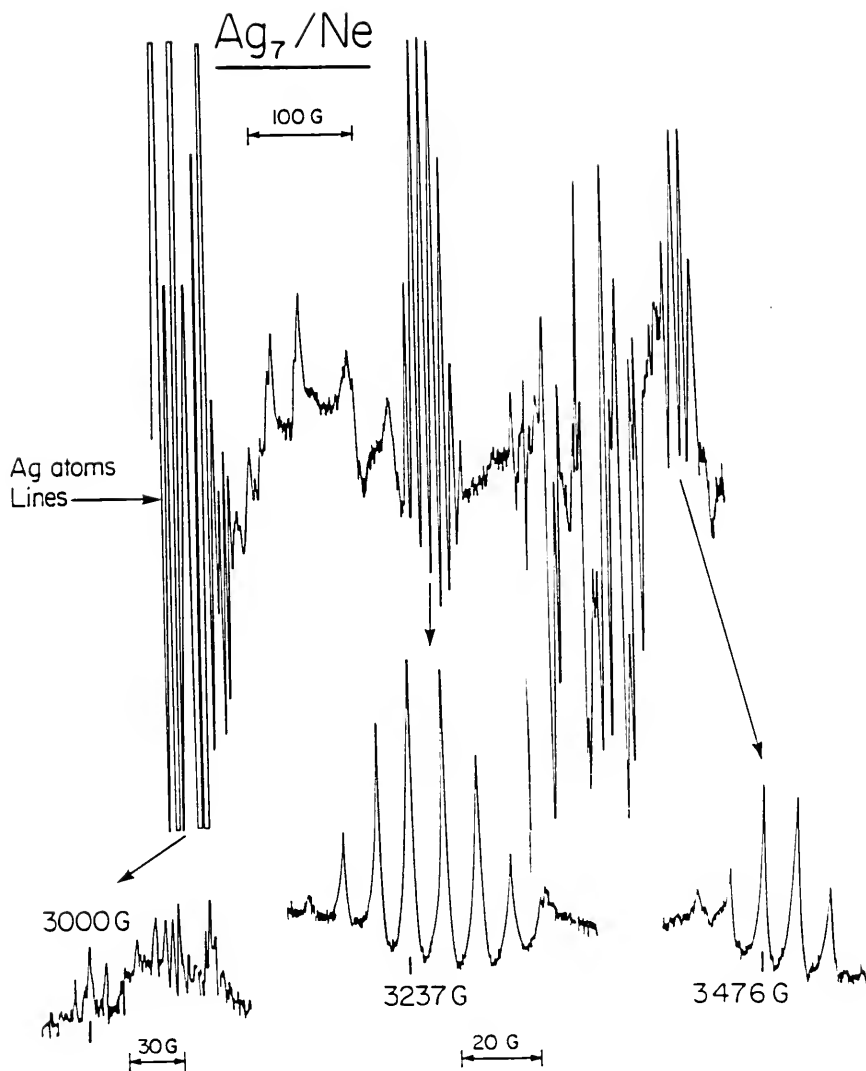


Figure III-2. The ESR spectrum of  $^{109}\text{Ag}$  in solid neon matrix at 4 K ( $\nu = 9.5338$  GHz). The top trace is the overall spectrum, and the bottom traces are expansions of the three regions of interest after annealing. Notice the large intensity of the silver atom lines at 3000 G before annealing.

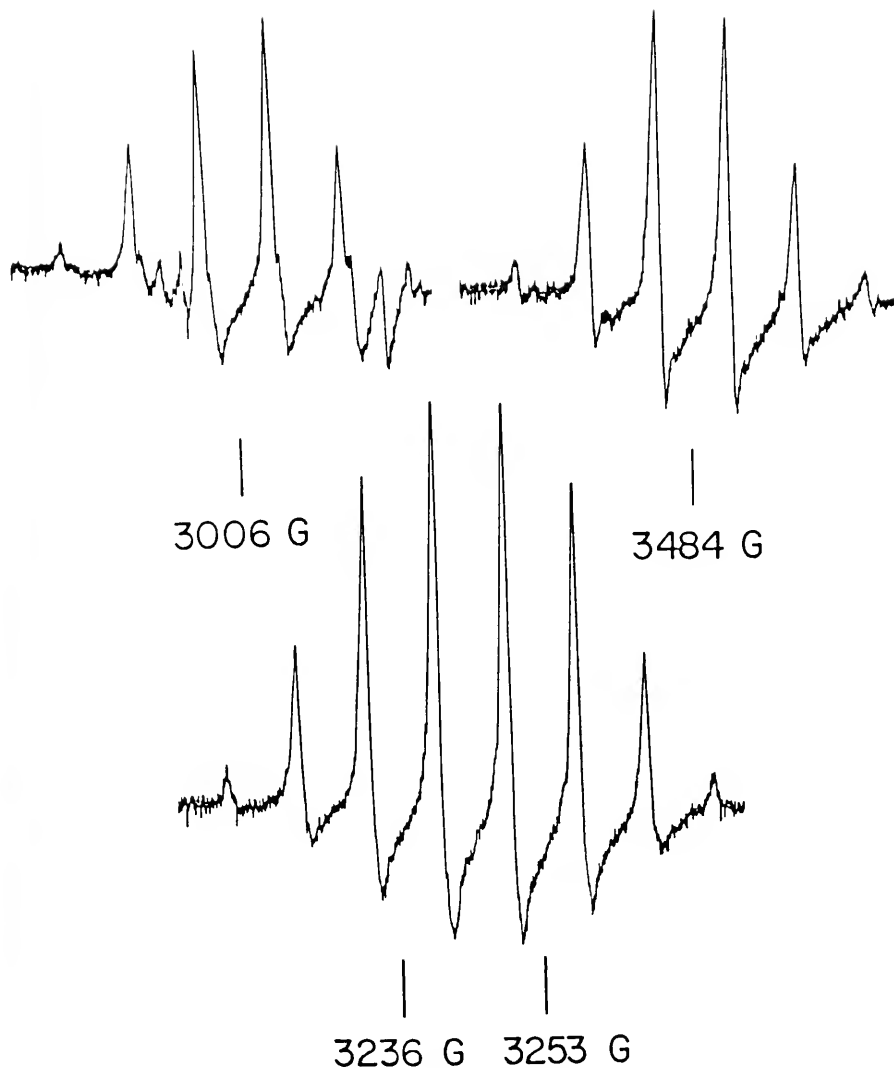


Figure III-3. The ESR spectrum of  $^{109}\text{Ag}_7$  in a solid neon matrix at 4 K ( $\nu = 9.5338$  GHz). The fields indicated are the positions of the four hyperfine lines corresponding to  $|J, M_J\rangle = |1, 1\rangle$ ,  $|1, 0\rangle$ ,  $|0, 0\rangle$ , and  $|1, 1\rangle$  (see Table III-1). The spacing within each of the four 6-line patterns is uniformly 8.7 G. The few extra lines in the background of the lines centered at 3006 G are due to residual  $^{109}\text{Ag}$  atom signals.

the six line pattern. This, in fact, is found to be the case upon detailed analysis of the spectrum.

The spectrum is then assigned to the axial molecule shown in Figure III-1 where the  $\text{Ag}_7$  molecules are randomly oriented in the matrix. The strength and shape of the lines indicate that they correspond to "perpendicular" transitions (24) where the "parallel" components lie up field of each line and were not observed either because of their low intensity or because they were obscured by other ESR lines.

#### Analysis and Discussion

The analysis of the spectrum utilized the axial spin Hamiltonian

$$\begin{aligned} \text{(III-1)} \quad H = & g_{\parallel} \beta H_z S_z + g_{\perp} \beta (H_x S_x + H_y S_y) \\ & + A_{\parallel} S_z J_z + A_{\perp} (S_x J_x + S_y J_y) \end{aligned}$$

where, for two equivalent nuclei with  $I_1 = I_2 = 1/2$ , the appropriate quantum numbers are  $J = |I_1 + I_2|, \dots, |I_1 - I_2|$  and  $M_J = J, J-1, \dots, -J$ . This yields here, for  $S = 1/2$ , an 8 X 8 matrix from which the four observed transitions  $|J, M_J\rangle$  in Table III-I were calculated to better than 0.1 G by varying  $g_{\perp}$ ,  $A_{\perp}$ , and  $A_{\parallel}$ . The reasonable assumption was made that  $g_{\parallel}$  equals  $g_e$  in this axial molecule;  $g_{\parallel} < g_{\perp}$  is indicated by the shapes of the observed perpendicular lines. The hf splittings in the ring of five equivalent atoms of

8.65(5) G was a constant spacing to within the experimental error in the spectrum. It was then used in finding the calculated line positions in the last column of Table III-1. Calculated and observed line positions differ at most by 0.4 G.

The derived magnetic parameters of  $^{109}\text{Ag}_7$  are given in Table III-2. The  $A_{\parallel}(2)$  parameter for the axial atoms has a higher uncertainty because it is derived indirectly from the perpendicular line positions. The s electron spin densities at the axial (2) and ring (5) nuclei are derived from  $A_{\text{iso}}$  values in the usual way by comparison with the free atom  $^{109}\text{Ag}$  values (85). To do this for the ring (5) atoms it was necessary to assume that  $A_{\perp}(5) = A_{\parallel}(5) = A_{\text{iso}}(5)$ ; however, consideration of  $\Delta g_{\perp} = g_{\perp} - g_e$  (see below) indicates that there is unpaired p and/or d electron character on those atoms.

As indicated by the  $\rho_s$  in Table III-2, 65% of the spin is in an (antibonding) orbital on the two equivalent axial atoms in  $\text{Ag}_7$ , just as in  $\text{Na}_7$  and  $\text{K}_7$ . The s character on the five equivalent Ag atoms may arise from spin polarization and could be negative so that it would then total -6.0%. The rest of the spin, about 40%, is then distributed in p and/or d hybridization.

Lindsay, et al., have discussed the electronic properties of the alkali-metal septamers and place the unpaired spin in an  $a_2$  molecular orbital with the next lower



Table III-2. Magnetic parameters and s-electron spin densities for  $^{109}\text{Ag}_7$  cluster in its  $^2\text{A}_2$  ground state.

$g_{\perp}$	2.094 (3)
$g_{\parallel}$	2.0023 <sup>b</sup>
$ A_{\perp}(^{109}\text{Ag}) $ (2)	700 (3) MHz
$ A_{\parallel}(^{109}\text{Ag}) $ (2)	654 (30) MHz
$ A_{\perp}(^{109}\text{Ag}) $ (5)	25.4 (1) MHz
$A_{\text{iso}}(^{109}\text{Ag})$ (2) <sup>c</sup>	685 (12) MHz
$A_{\text{dip}}(^{109}\text{Ag})$ (2) <sup>c</sup>	15 (11) MHz
$\rho_S(^{109}\text{Ag})$ (2)	0.324 <sup>d</sup>
$\rho_S(^{109}\text{Ag})$ (2)	$\pm 0.012^{\text{d,e}}$

<sup>a</sup> (2) and (5) indicate the two equivalent axial and the five equivalent ring atoms, respectively.

<sup>b</sup> Assumed.

<sup>c</sup>  $A_{\perp}$  and  $A_{\parallel}$  have been taken as positive in calculating  $A_{\text{iso}}$  and  $A_{\text{dip}}$  (see ref. 118, page 55). This neglects the sign of the nuclear moment which is negative.

<sup>d</sup>  $\rho_S(i)$  are the s-electron spin densities calculated as the ratio of  $A_{\text{iso}}(i)$  to that of the free atom (2114 MHz (119)).

<sup>e</sup> Assuming  $A_{\perp}(5) = A_{\parallel}(5) = A_{\text{iso}}(5)$ .

filled orbital as  $e_1$ . This Hückel model calculation has been recently discussed in more detail in two separate papers by Wang, George, Lindsay, and Beri (109). Others have made extensive calculations, also justifying pentagonal bipyramid structures (99).

The simplest assumption to account for the observed positive shift in  $\Delta g_{\perp}$  ( $= +0.092$ ) is that it results from spin-orbit coupling of the  ${}^2A_2$  ground state with the low-lying  ${}^2E_1$  excited state produced by exciting one of the four  $e_1$  electrons into the singly-occupied  $a_2$  orbital. Then

$$(III-2) \quad \Delta g_{\perp} \approx (-2\lambda/\Delta E) \langle E_1' | l_X | A_2'' \rangle \langle A_2'' | l_X | E_1' \rangle$$

where  $\Delta E = E_{E_1'} - E_{A_2''}$  and  $\lambda$  is taken as the spin-orbit coupling constant for a 5p electron (about  $615 \text{ cm}^{-1}$ ) (103) and/or for a 4d electron (about  $1800 \text{ cm}^{-1}$ ) (87) on atomic Ag. According to the Hückel model of Lindsay, et al. (109),  $\Delta E = 0.7B = 4000 \text{ cm}^{-1}$  where B for Ag was taken as  $1/8$  (Fermi energy) (97) which is about 0.7 eV (111). Then to estimate the required matrix elements one must consider the MO's formed from s, p, and d electrons in  $D_{5h}$  symmetry. These have been considered in detail for a ring of five Mn atoms (13), and one then deduces that the non-zero matrix elements for the "perpendicular"  $l_X$  operator, involving only the five circumferential silver atoms of  $Ag_7$ , are

$$\langle e_1' (p\pi_y) | l_X | a_2'' (p\pi_z) \rangle = 1$$

and

$$\langle e_1' (d\delta_{z^2 - y^2}) | l_X | a_2'' (d\pi_{xz}) \rangle = 1 \quad (112).$$

Here, at each ring atom, the x axis points toward the center of the ring and the z axis is parallel to the principal five-fold axis of the molecule. The p or d spin density on the central two axial atoms does not yield non-zero matrix elements.

Then to check the reasonableness of the measured  $\Delta g$  via Eq. III-2, one can consider the limiting cases of contribution of either all p character or all d character to the wavefunction, where the coefficient of that AO is  $(0.4)^{1/2}$  in the  $a_2''$  MO. If one also assumes that all such non-s character lies at the ring atoms, then one finds from Eq. III-2 that the fraction of  $p\pi$  character in the  ${}^2E_1'$  excited state must be 0.75. On the other hand, with much larger d-electron spin-orbit coupling the  $d\pi$  fraction drops to the more reasonable value of 0.26 if the unpaired electron is in an s-d hybrid. These are, of course, very crude calculations, meant only to justify the magnitude of the observed  $g_{\perp}$  shift.

The ESR spectrum in Figure III-2 is very similar to that obtained by Howard, et al. (105), when  ${}^{107}\text{Ag}$  was trapped in a deuterated cyclohexane matrix at 77 K, but the small hyperfine splittings are completely resolved here. Those

authors attributed the "superhyperfine" structure to five lines (rather than the six observed here) and assigned their spectrum to  $\text{Ag}_5$  with a distorted trigonal bipyramid structure. However, our derived parameters (corrected to the  $^{107}\text{Ag}$  nuclear moment) are essentially the same as theirs (see Table III-3) except for their "superhyperfine" analysis, so that it is clear that the molecule they were observing is  $\text{Ag}_7$ .

Perhaps of greatest overall interest is the conclusion from this work that Group IA (alkali-metal) and Group IB clusters are closely related. This is emphasized by a comparison of spin densities among the  $\text{M}_7$  cluster, as shown in Table III-4. This is not surprising and confirms the view that both series of atoms may be treated as having one s electron interacting by a suitable pseudopotential with an inner closed shell core.

Table III-3. Comparison of the magnetic parameters of  $^{107}\text{Ag}_7$  (this work) with those of Howard, et al.'s  $^{107}\text{Ag}_5$  cluster.

Parameter	$^{107}\text{Ag}_5$	$^{107}\text{Ag}_7$
	in $\text{C}_6\text{D}_{12}$	in Neon
$g_{\perp}$	2.085	2.094
$A_{\perp}(^{107}\text{Ag}) (2)^c$	201 G	204 G
$A_{\perp}(^{107}\text{Ag}) (5)^c$	5.5 G	7.5 G

<sup>a</sup> Reference 102.

<sup>b</sup>  $A_{\perp}$  values obtained here for  $^{109}\text{Ag}_7$  have been converted to  $^{107}\text{Ag}_7$  values using the ratio  $^{109}\mu/^{107}\mu = 1.1543$ .

<sup>c</sup> (2) and (5) indicate axial and ring atoms, respectively.

Table III-4. Spin densities (s-electron) compared for the  $^2A_2$  ground states of the  $Na_7$ ,  $K_7$ , and  $Ag_7$  clusters.

	$Na_7$	$K_7$	$Ag_7$
$\rho_S (2)^c$	0.374	0.371	0.325
$\rho_S (5)^c$	-0.021	-0.022	$\pm 0.012$

<sup>a</sup> Ref. 98

<sup>b</sup> This work.

<sup>c</sup> (2) and (5) indicate axial and ring atoms, respectively.

CHAPTER IV  
ESR OF METAL SILICIDES

ESR of MnSi and AgSi

Introduction

Silicon has become important in recent years because of the semi-conductor industry, and is also interesting to the chemist as an analogue of carbon. Various small silicon containing molecules have been studied already in this laboratory:  $\text{HSiO}$ ,  $\text{SiH}_3$ ,  $\text{SiCO}$ , and  $\text{Si}_2$  (113,114). We consider here the silicon analogs of transition-metal carbides. A major difference between carbon and silicon atoms, other than the larger nucleus and a closed shell of electrons for silicon, is the availability of empty d orbitals to silicon. Therefore we undertook a study of silicon and various first row transition metals and coinage metals, with special emphasis on the known metal carbide species (115). We were able to isolate only two species which contain only silicon and another metal, which we assign as  $\text{AgSi}$  and  $\text{MnSi}$ .

Experimental

These experiments were carried out in the usual way. The metals were vaporized from tantalum cells using water cooled copper electrodes. Silver ( $I=1/2$ ) (200 mesh powder, 99.9% pure from Aesar) was heated to approximately 1250 °C

and manganese (100%,  $I=5/2$ ) (Spex flakes, metal impurities 100 ppm max.) was heated to approximately 1100 °C. Silicon (95.3%  $I=0$ , 4.7%  $I=1/2$ )(99.9% pure, 20 mesh from Union Carbide) was also vaporized from a tantalum cell at about 1700 °C. The metal vapor was codeposited with argon (Airco, 99.999% pure) which was introduced to the system at a flow rate of approximately 0.1 mmole/hour, and deposited on a sapphire rod at approximately 14 K. All vaporization temperatures reported here are surface temperatures of the cells and have not been corrected for emissivity. Normal deposition times ranged from 45 to 75 minutes. The ESR spectra were taken using a Varian E-Line Century series EPR spectrometer modified to operate with a Bruker BH-15 Field Controller for the manganese work and a Varian VFR-2503 Field Dial for the silver work. The matrices were annealed to various temperatures and pressures without any significant change in the ESR spectrum.

### ESR Spectra

#### AgSi

Two doublets were observed for this molecule. These were due to the two naturally occurring isotopes of silver ( $^{107}\text{Ag}$  51.82%,  $^{109}\text{Ag}$  48.18%) which have slightly different nuclear moments. Lines at 3321 and 3375 gauss were assigned to  $^{107}\text{AgSi}$  and lines at 3317 and 3379 gauss were assigned to  $^{109}\text{AgSi}$  (Figure IV-1). Unfortunately no parallel lines have



been observed for this molecule. The observed perpendicular lines have been fit to within one gauss. We found that  $g_{\perp} = 1.9981$  and  $A_{\perp} = 53.2$  gauss for  $^{107}\text{AgSi}$  and  $A_{\perp} = 61.2$  gauss for  $^{109}\text{AgSi}$  (Table IV-1).

### MnSi

A series of six lines centered at about  $g_{\text{eff}} = 4$  are observed for this molecule (Figure IV-2). Several experiments were done in which the concentration of silicon in the matrix was varied in order to determine whether we were observing MnSi or possibly a larger cluster. The same was done for manganese and the only lines that grew in were due to  $\text{Mn}_2$  and  $\text{Mn}_5$  (13). Higher manganese concentrations caused the signals due to MnSi to decrease and they disappeared altogether at high manganese concentrations. No new lines attributable to a higher-order MnSi cluster were observed. Table IV-2 summarizes the hyperfine parameters for MnSi.

## Analysis and Discussion

### AgSi

From the ESR spectrum the ground state of AgSi has been determined to be doublet sigma. This is consistent with the idea of a  $sd^{10}$  ground state for silver and  $s^2p^2$  ground state for silicon. Because of the small hyperfine splitting due to the silver nucleus, most of the unpaired spin density

Table IV-1. Observed and calculated line positions (in Gauss)  
for AgSi in argon at 14 K. ( $\nu = 9.380$  GHz)

=====

Perpendicular Lines

$M_I(\text{Ag})$	<u>Obsd(2)</u>	<u>Calcd(2)</u>
1/2 (107)	3321	3321
- 1/2 (107)	3375	3375
1/2 (109)	3317	3317
- 1/2 (109)	3379	3378

Derived Parameters

$g_{\perp}$	1.9981
$g_{\parallel}$	2.0023 <sup>a</sup>
$ A_{\perp} $	149 MHz
$ A_{\parallel} $	149 MHz <sup>b</sup>

<sup>a</sup> Assumed equal to  $g_e$

<sup>b</sup> Assumed equal to  $A_{\perp}$

( ) Error in the line positions.

Table IV-2. Observed and calculated line positions (in Gauss)  
for MnSi in argon at 14 K. ( $\nu = 9.380$  GHz)

=====

Perpendicular Lines

<u><math>M_I</math> (Mn)</u>	<u>Obsd(2)</u>	<u>Calcd(2)</u>
5/2	1424	1425
3/2	1513	1513
1/2	1607	1606
- 1/2	1703	1702
- 3/2	1804	1802
- 5/2	1906	1906

( ) Error in the line positions.

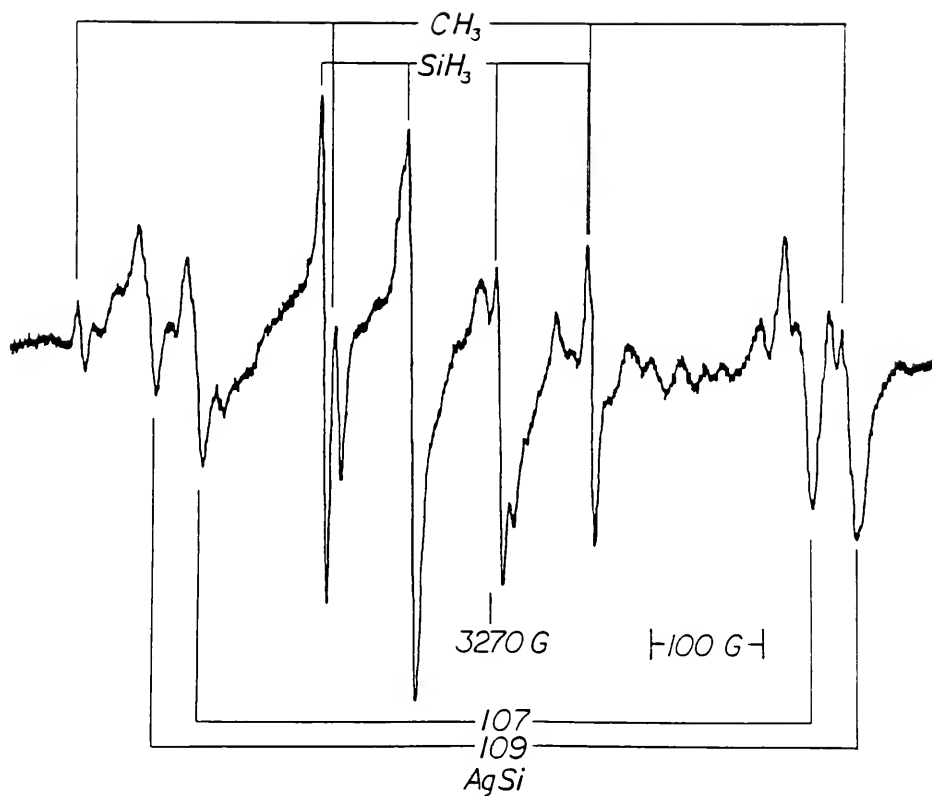


Figure IV-1. The ESR spectrum of AgSi is an argon matrix at 12 K. The line positions of the impurities ( $\text{CH}_3$  and  $\text{SiH}_3$ ) are noted.  $\nu = 9.380 \text{ GHz}$ .

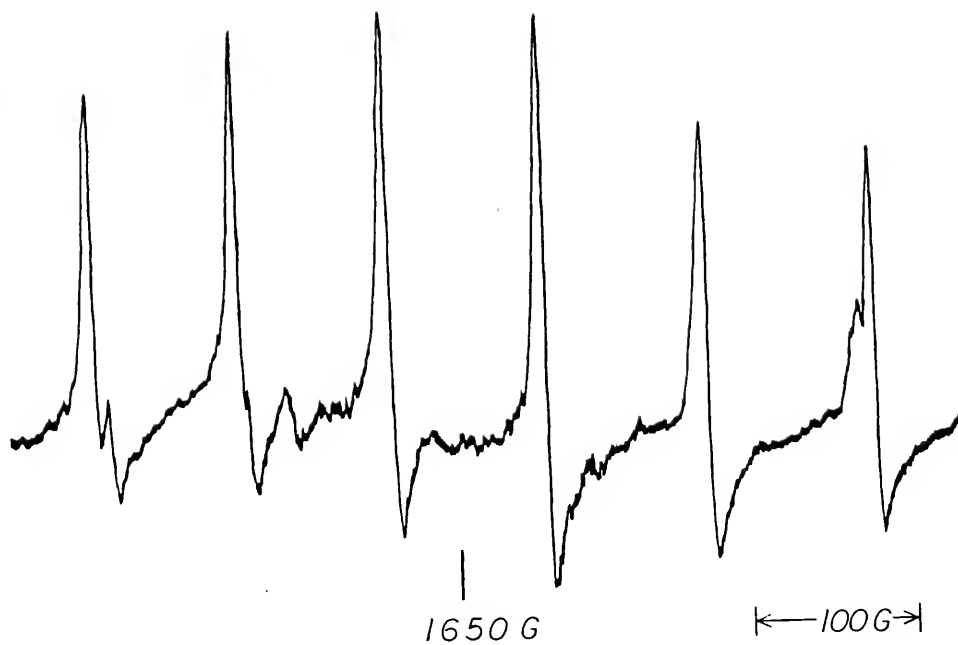


Figure IV-2. The ESR spectrum of MnSi in an argon matrix at 12 K.  $\nu = 9.380$  GHz.

probably resides in a p orbital on the silicon. The hyperfine parameters as well as g were fit for both isotopes. The difference in the hyperfine parameters that arise between the two molecules is due to the fact that the nuclear moments are slightly different for  $^{107}\text{Ag}$  and  $^{109}\text{Ag}$ . The ratio of the hyperfine parameters was found to be approximately equal to the ratio of the nuclear moments. Since no parallel lines were observed, we had three unknowns to fit to only two lines, the two observed lines gave two equations with which to determine the hyperfine parameters. The  $A_{\parallel}$  parameter was assumed to be equal to  $A_{\perp}$  in order to solve the equations. This introduced a certain amount of error into the derived parameters for  $\text{AgSi}$ .

The molecule was fit to a spin Hamiltonian with axial symmetry such as the one below (46),

$$\begin{aligned}
 \text{(IV-1)} \quad H = & gBS_zH_z + KS_zI_z + X_1^-(S^+I_1^+ + S^-I_1^-) \\
 & + X_1^+(S^+I_1^- + S^-I_1^+)
 \end{aligned}$$

which was modified for an  $S = 1/2$  and  $I = 1/2$  system. A 4 X 4 matrix was set up for all of the possible combinations of  $m_I$  and  $m_S$ . This matrix was then diagonalized using a program which fits the hyperfine parameters to an unrotated Hamiltonian similar to (24):

$$\begin{aligned}
 \text{(IV-2)} \quad H = & g_{\parallel} \beta H_z S_z + g_{\perp} \beta (H_x S_x + H_y S_y) \\
 & + A_{\parallel} I_z S_z + A_{\perp} (I_x S_x + I_y S_y)
 \end{aligned}$$

The hyperfine parameters were then adjusted so as to give the best fit to the observed line positions. The calculations were made assuming that  $\theta = 90$  degrees. This assumption was made because of the shapes of the observed lines.

Because no parallel lines were observed, it was not possible to determine an independent value for  $A_{\parallel}$ . This has also made it impossible to determine a value for  $A_{\text{iso}}$  or  $A_{\text{dip}}$ . Without these parameters a value for the spin density on the silver atom cannot be determined.

### MnSi

MnSi was found to have a  $^4\Sigma$  ground state. This implies a double bond between the manganese and the silicon since the atoms have a  $s^2d^5$  and  $s^2p^2$  ground state electron configurations, respectively. If the two unpaired p electrons bonded with two of the unpaired d electrons in manganese, this would leave three unpaired d electrons, which are most likely in  $d\pi(2)$  and a  $d\sigma$  molecular orbitals. Again, no other lines were observed for this molecule. This was either due to their low intensity or the parallel lines were obscured by other lines that occur at 3400 G such as  $\text{SiH}_3$ , which were much more intense.

The molecule was also fit to an axial spin Hamiltonian which was modified for a  $S = 3/2$  and  $I = 5/2$  system. This produces a  $24 \times 24$  matrix which is then diagonalized and fit to the observed lines in order to determine the hyperfine parameters for this molecule. The fitting program utilizes a non-rotated spin Hamiltonian in order to fit the differences of eigenvalues to  $h\nu$  by varying  $g_{\perp}$ ,  $A_{\perp}$ , and  $A_{\parallel}$ . This program was also utilized in determining the errors of the calculated hyperfine parameters. Because we observed six lines for this molecule ( $Mn: m_I = 5/2, \dots, -5/2$ ), we were able to fit the lines to within the experimental error of the lines (2 gauss). The interesting thing to note about this species is the large zero-field splitting of  $2 \text{ cm}^{-1}$  (not so unusual if one remembers that  $MnO$  has a similar  $D$  value (116)).

Since six lines were observed, we had more equations than parameters allowing determination of  $A_{\parallel}$  independent from  $A_{\perp}$ . Even though no parallel lines were observed from which  $A_{\parallel}$  could be directly determined, the calculated value is still adequate for calculating  $A_{iso}$  and  $A_{dip}$ . This allowed us to calculate a value for the spin density of the unpaired electrons on the manganese atom ( Table IV-3 ).

As in the case of  $MnO$  only one set of lines was observed for  $MnSi$ . This makes it difficult to assign an accurate  $g_{\perp}$  and  $D$  value to the molecule since the two values are interdependent on each other. In order to unequivocally determine the parameters, it would have been necessary to



Table IV-3. Hyperfine parameters and calculated spin densities for MnSi in argon at 14 K.  
( $\nu = 9.380$  GHz)

=====

<u>Derived Parameters</u>	
$g_{\perp}$	2.0080
$g_{\parallel}$	2.0023 <sup>a</sup>
$ A_{\perp} $	270 MHz
$ A_{\parallel} $	350 MHz
$A_{iso}$	297 MHz <sup>b</sup>
$A_{dip}$	80 MHz <sup>b</sup>

<u>Spin Densities for Manganese</u>	
$\rho_S$	0.12
$\rho_{2d\sigma}$	1.35

<sup>a</sup> Assumed equal to  $g_e$ .

<sup>b</sup> Assuming that  $A_{\perp}$  and  $A_{\parallel}$  are both positive.

observe a set of high field lines. Unfortunately, as in the MnO case, none have been observed. The parameters  $g_{\perp}$  and D were varied in order to determine their relative effects on each other, as well as to find the best fit for the observed product lines. The final hyperfine parameters are listed in Table IV-3. A zero field splitting of  $2 \text{ cm}^{-1}$  is a reasonable for MnSi when considering other manganese containing molecules (117,118).

### ESR of Hydrogen-Containing

### Scandium-Silicon Clusters

#### Introduction

Clusters of various sizes have been successfully produced with scandium (14,9). In a series of experiments involving first row transition metal carbides ScC was not observed. It was of interest therefore whether a ScSi species could be made. Several attempts were made to produce such a molecule, all of which showed no evidence of the molecule being trapped in an argon matrix. Instead a variety of other molecules containing both silicon and scandium were observed. A typical blank involving only scandium produced signals which were apparently due to a  $\text{Sc-H}_2\text{O}$  molecule which has been observed by other workers (119). A typical silicon blank usually yields several species containing silicon such

as  $\text{SiH}_3$ ,  $\text{SiCO}$ , and  $\text{Si}_2$  (113,115). When silicon and scandium were codeposited into an argon matrix several sets of new bands appeared.

### Experimental

Standard methods for producing the metal containing argon matrices were used in this series of experiments. The scandium and silicon metals were vaporized from a furnace flange onto which two tantalum cells were mounted on separate sets of electrodes, so that it was possible to heat the cells to different temperatures. The scandium (100%,  $I=7/2$ ) (Alfa Products, 99.9% pure metal shavings) was vaporized from a 40 mil tantalum cell at about 1265 °C. The deposition temperature for the scandium was rather critical since too high a temperature would produce scandium clusters which tended to obscure the product lines, and a temperature that was too low would fail to yield any product lines at all. Silicon (95.3%  $I=0$ , 4.7%  $I=1/2$ ) (99.9% pure, 20 mesh from Union Carbide) was vaporized from a tantalum cell at about 1700 °C. The matrix gas (argon, Airco, 99.9996% pure) was flowed in at the rate of about 12 to 18 mmole/hour. The sapphire rod was kept at about 14 K during the experiment utilizing an Air Products Displex closed cycle refrigeration system. The matrix was analyzed using a Varian E-line Century EPR modified to operate with a Bruker BH-15 Field Control unit. Utilizing this type of a set up we were able

to reduce the uncertainty in our line positions to about 2 Gauss. Deposition of the matrix usually took about 60 minutes.

### ESR Spectra

#### HScSiH<sub>n</sub>

The ESR signal attributed to this molecule consists of a set of eight doublets centered at 3530 G (Figure IV-3). Unfortunately not all eight lines are clearly visible. Three of the lines (3400G, 3470G, and 3699G) (Figure IV-3) are almost completely obscured. The lines are only visible when the flat surface of the rod is parallel to the pole faces of the magnet (Figure IV-4). The lines almost completely disappeared when the matrix was slightly annealed (Figure IV-5). This indicates that the molecule is highly oriented within the matrix trapping site. We were therefore able to identify those lines which were overlapping or very close to other lines. The doublets were only observed when both silicon and scandium were codeposited. The set of 8 lines is listed in Table IV-4, the center of the doublet was used to fit each of the lines. A list of the parameters calculated for this molecule can be found in Table IV-5. It was not possible to resolve any hyperfine structure due to silicon. Therefore n could not be determined accurately.

Table IV-4. Observed and calculated line positions (in Gauss) for  $\text{HScSiH}_n$  in argon at 14 K.  
 $(\nu = 9.380 \text{ GHz})$

=====

Perpendicular Lines

<u><math>M_I(\text{Sc})</math></u>	<u>Obsd(2)</u>	<u>Calcd(2)</u>
7/2	3204	3204
5/2	3265	3265
3/2	3330 <sup>a</sup>	3330
1/2	3398 <sup>a</sup>	3398
- 1/2	3469	3469
- 3/2	3543	3543
- 5/2	3620 <sup>a</sup>	3620
- 7/2	3699	3699

<sup>a</sup> Not possible to assign a line position from the spectrum because of a large number of other lines in the same region

( ) Error in the line positions.

Table IV-5. Hyperfine parameters and calculated spin densities for  $\text{HScSiH}_n$  in argon at 14 K.  
 $(\nu = 9.380 \text{ GHz})$

=====

<u>Derived Parameters</u>	
$g_{\perp}$	1.9386
$g_{\parallel}$	2.0023 <sup>a</sup>
$ A_{\perp} $	192 MHz
$ A_{\parallel} $	345 MHz
$A_{\text{iso}}$	243 MHz <sup>b</sup>
$A_{\text{dip}}$	51 MHz <sup>b</sup>

<u>Spin Densities for Scandium</u>	
$\rho_s$	0.09
$\rho_{3d\sigma}$	0.74

<sup>a</sup> No parallel lines were observed, so  $g_{\parallel}$  was set equal to 2.0023.

<sup>b</sup> Assuming that  $A_{\perp}$  and  $A_{\parallel}$  are both positive.

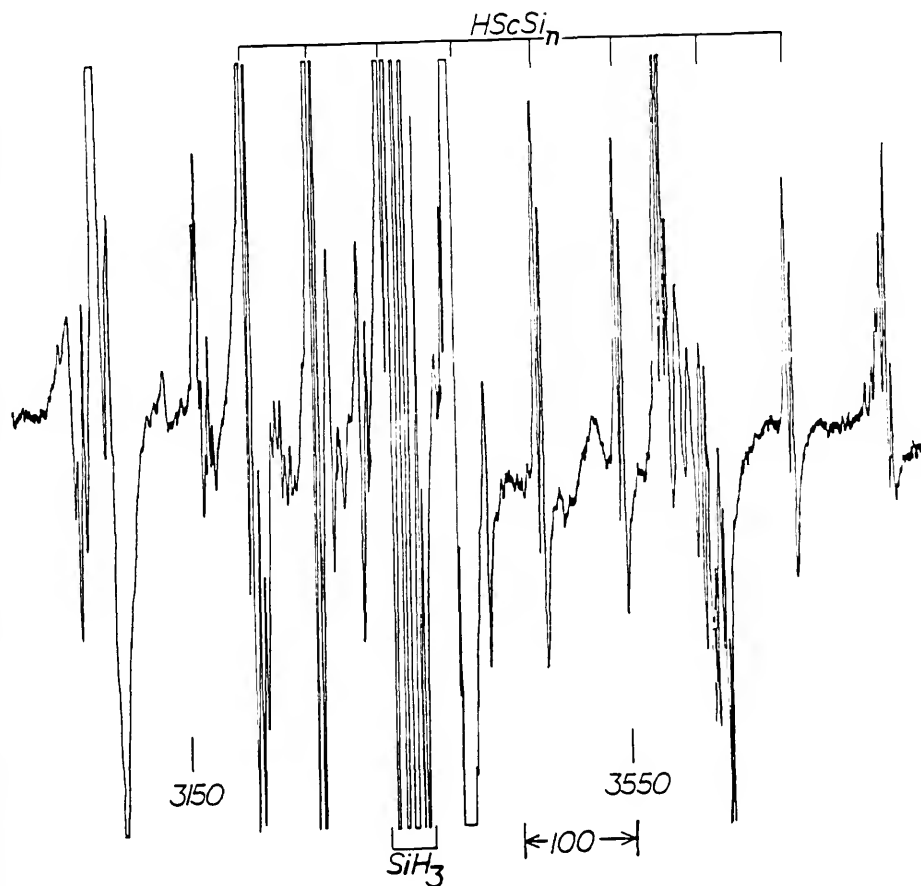


Figure IV-3. The ESR spectrum of Sc codeposited with Si into an argon matrix at 12 K. The eight sets of doublets are shown for  $HScSiH_n$ .  $\nu = 9.380$  GHz.

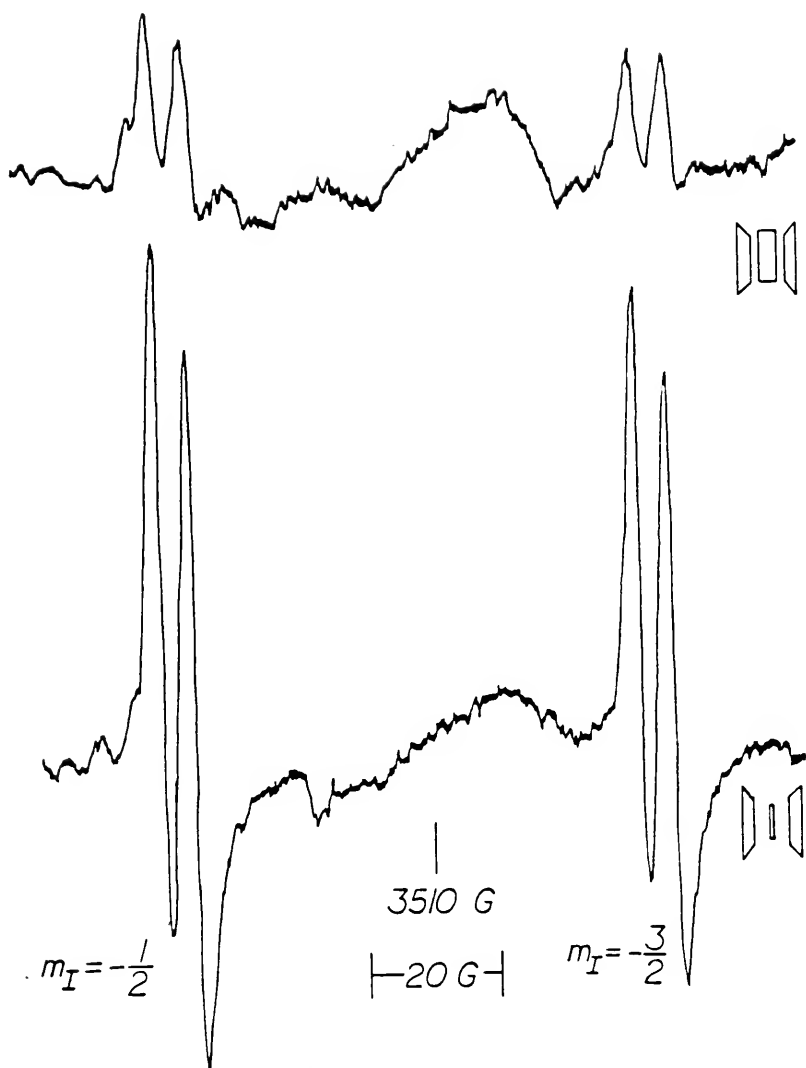


Figure IV-4. The  $m_I = -1/2$  and  $-3/2$  transitions for  $\text{HScSiH}_n$  at 12 K. Two different rod orientations are shown. The top is with the rod parallel to the field and the bottom trace is for the rod perpendicular to the field.  $\nu = 9.380$  GHz.



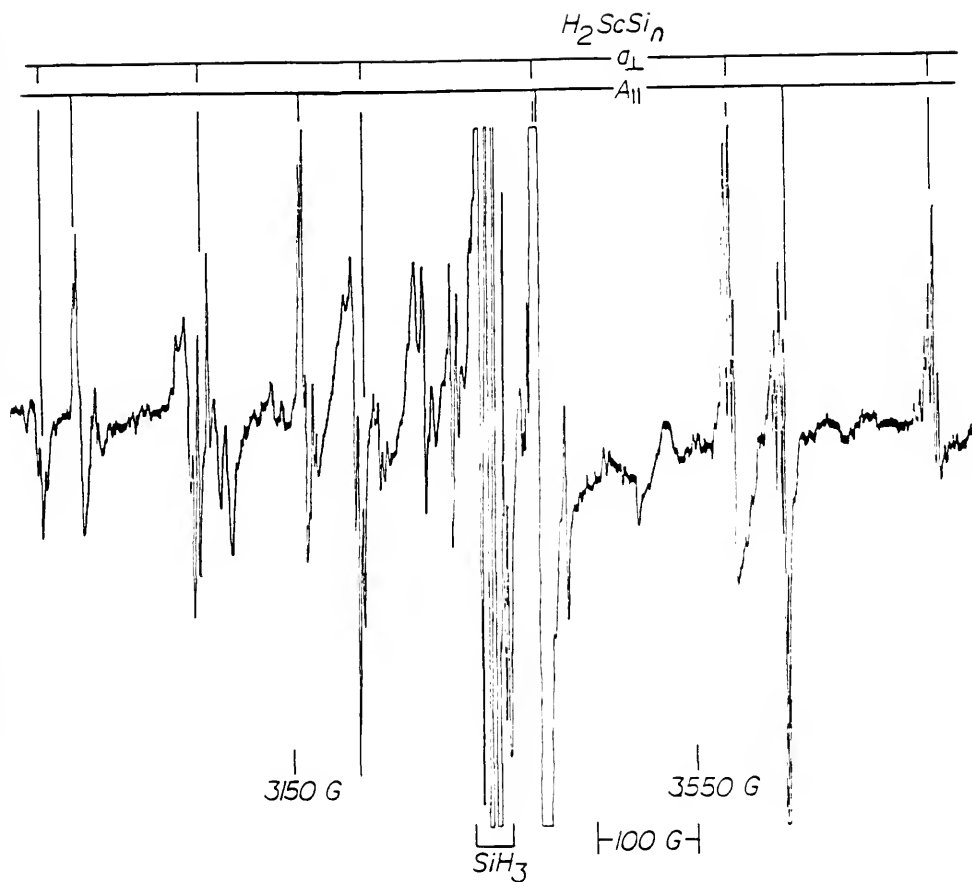


Figure IV-5. The ESR spectrum in the  $g=2$  region after annealing a matrix containing both Si and Sc ( $\nu = 9.380$  GHz). The doublets due to  $HScSiH_n$  have disappeared. The only remaining lines are due to impurities and  $H_2ScSiH_n$  (noted).

H<sub>2</sub>ScSiH<sub>n</sub>

Four sets of eight triplets were also observed when scandium and silicon were codeposited into an argon matrix. Seven of the four sets of eight triplets are shown in Figures IV-6 through 9. The 1:2:1 triplet intensity pattern observed is what one would expect for a molecule containing two equivalent hydrogens. Again, lines were obscured by other lines but in this case it occurred in the 3400G region of the spectrum only. These lines were assigned on the basis of belonging to the same molecule (due to the similar triplet structures on all of the lines), but trapped in two different matrix sites. The most intense lines (A) belong to the trapping site of the majority of the H<sub>2</sub>ScSiH<sub>n</sub> molecules, and (a) the weak set of lines which belong to H<sub>2</sub>ScSiH<sub>n</sub> trapped in a secondary site. The first set of lines (A) were most intense when the flat surface of the rod was parallel to the pole faces of the magnet (bottom trace in Figures IV-(6-9)), and the intensity of the lines decreased to almost zero when the rod was turned perpendicular to the pole faces (top trace in Figures IV-(6-9)). A second, somewhat less intense set of lines due to the (A) site, were observed growing in when, upon turning the rod, the other lines disappeared. This set of triplets also exhibited broader linewidths than the most intense set of (A) lines, and the lines were assigned as the parallel lines for the (A) site. Line positions for the perpendicular and parallel lines of (A) can be found in Table

IV-6. Both sets of lines were centered at approximately  $g = 2$ . The large change in intensities upon rotating the rod indicates that the molecule being observed is highly oriented in the matrix. ESR parameters for this molecule were calculated and can be found in Table IV-7.

Two other sets of triplets (a) were also observed in the experiments with silicon and scandium. These were significantly weaker than the first set and can be seen close to the (A) lines in Figures IV-(6-9). The perpendicular lines showed some orientation but not to the extent of the first set. The parallel lines were much weaker and broader and observed only when the rod was perpendicular to the pole faces of the magnet. The parallel and perpendicular line positions for (a) can be found in Table IV-8. These lines were also centered around  $g = 2$ , but were found within the highly oriented molecule's hyperfine splitting (Figures IV-(6-9)). The hyperfine parameters for (a) site can be found in Table IV-9. As expected, they are just slightly different than those found in Table IV-7.

#### Analysis and Discussion

##### HScSiH<sub>n</sub>

The set of eight doublets have been fit using a 16 X 16 matrix developed for an unrotated spin Hamiltonian. The variables  $g_{\perp}$ ,  $A_{\parallel}$ , and  $A_{\perp}$  were fit. The  $g_{\parallel}$  parameter was set equal to  $g_e$  which is equal to 2.0023. Because no parallel

Table IV-6. Observed and calculated line positions (in Gauss) for  $\text{H}_2\text{ScSiH}_n$ , the (A) site, in argon at 14 K. ( $\nu = 9.380$  GHz)

=====

Perpendicular Lines

<u><math>M_I(\text{Sc})</math></u>	<u>Obsd(2)</u>	<u>Calcd(2)</u>
7/2	2733	2733
5/2	2877	2877
3/2	3035	3035
1/2	3206	3206
- 1/2	3391 <sup>a</sup>	3391
- 3/2	3589	3589
- 5/2	3802	3801
- 7/2	4027	4026

Parallel Lines

<u><math>M_I(\text{Sc})</math></u>	<u>Obsd(2)</u>	<u>Calcd(2)</u>
7/2	2516	2515
5/2	2720	2720
3/2	2935	2934
1/2	3159	3159
- 1/2	3394 <sup>a</sup>	3394
- 3/2	3638	3638
- 5/2	3893	3893
- 7/2	4157	4158

<sup>a</sup> Not possible to assign a line position from the spectrum because of a large number of other lines in the same region.

( ) Error in line positions.

Table IV-7. Hyperfine parameters and calculated spin densities for  $\text{H}_2\text{ScSiH}_n$ . site (A), in Argon at 14 K. ( $\nu = 9.380$  GHz)

<u>Derived Parameters</u>	
$g_{\perp}$	1.9695
$g_{\parallel}$	1.9983
$ A_{\perp} $	507 MHz
$ A_{\parallel} $	653 MHz
$A_{\text{iso}}$	557 MHz <sup>a</sup>
$A_{\text{dip}}$	48 MHz <sup>a</sup>
<u>Spin Densities for Scandium</u>	
$\rho_{\text{S}}$	0.20
$\rho_{3d\sigma}$	0.70

<sup>a</sup> Assuming that  $A_{\perp}$  and  $A_{\parallel}$  are both positive.

Table IV-8. Observed and calculated line positions (in Gauss) for  $\text{H}_2\text{ScSiH}_n$ , the (a) site, in argon at 14 K. ( $\nu = 9.380$  GHz)

=====

<u>Perpendicular Lines</u>		
<u><math>M_I(\text{Sc})</math></u>	<u>Obsd(2)</u>	<u>Calcd(2)</u>
7/2	2759	2758
5/2	2899	2898
3/2	3051	3050
1/2	3216	3216
- 1/2	3393 <sup>a</sup>	3393
- 3/2	3583	3584
- 5/2	3786	3786
- 7/2	4001	4001

<u>Parallel Lines</u>		
<u><math>M_I(\text{Sc})</math></u>	<u>Obsd(2)</u>	<u>Calcd(2)</u>
7/2	2548	2548
5/2	2745	2746
3/2	2953	2953
1/2	3169	3169
- 1/2	3394 <sup>a</sup>	3394
- 3/2	3630	3630
- 5/2	3874	3874
- 7/2	4127	4127

<sup>a</sup> Not possible to assign a line position from the spectrum because of a large number of other lines in the same region

( ) Error in line positions.

Table IV-9. Hyperfine parameters and calculated spin densities for  $\text{H}_2\text{ScSiH}_n$ , site (a), in Argon at 14 K. ( $\nu = 9.380$  GHz)

<u>Derived Parameters</u>	
$g_{\perp}$	1.9703
$g_{\parallel}$	1.9985
$ A_{\perp} $	489 MHz
$ A_{\parallel} $	631 MHz
$A_{\text{iso}}$	536 MHz <sup>a</sup>
$A_{\text{dip}}$	47 MHz <sup>a</sup>

Spin Densities for Scandium

$\rho_{\text{S}}$	0.19
$\rho_{3d\sigma}$	0.69

<sup>a</sup> Assuming that  $A_{\perp}$  and  $A_{\parallel}$  are both positive.

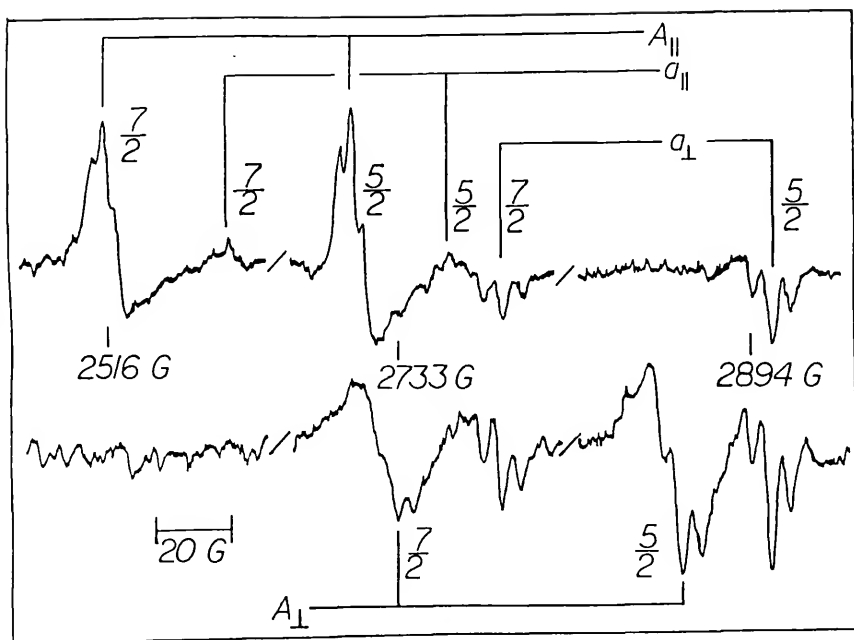


Figure IV-6. The ESR spectrum ( $m_I = 7/2$  and  $5/2$ ) for  $\text{H}_2\text{ScSiH}_n$  in argon at 12 K after annealing to about 30 K. The top trace is for the rod perpendicular to the field and the bottom trace is for the rod parallel to the field.  $\nu = 9.380$  GHz.



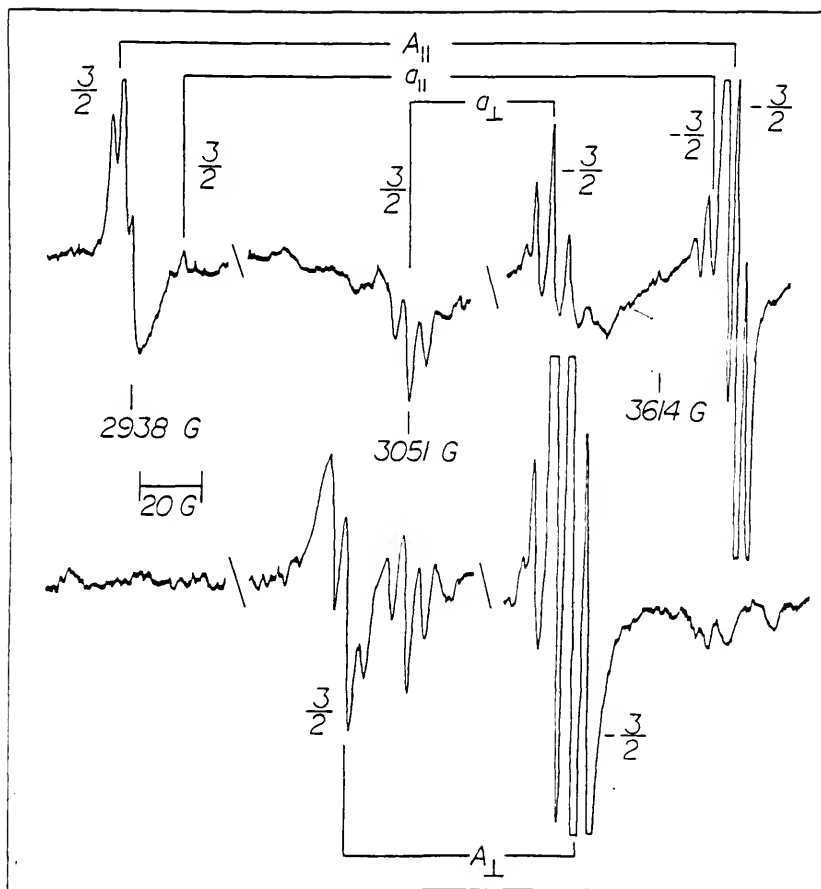


Figure IV-7. Same as Figure IV-6 except the  $m_I = 3/2$  and  $-3/2$  transitions are shown.

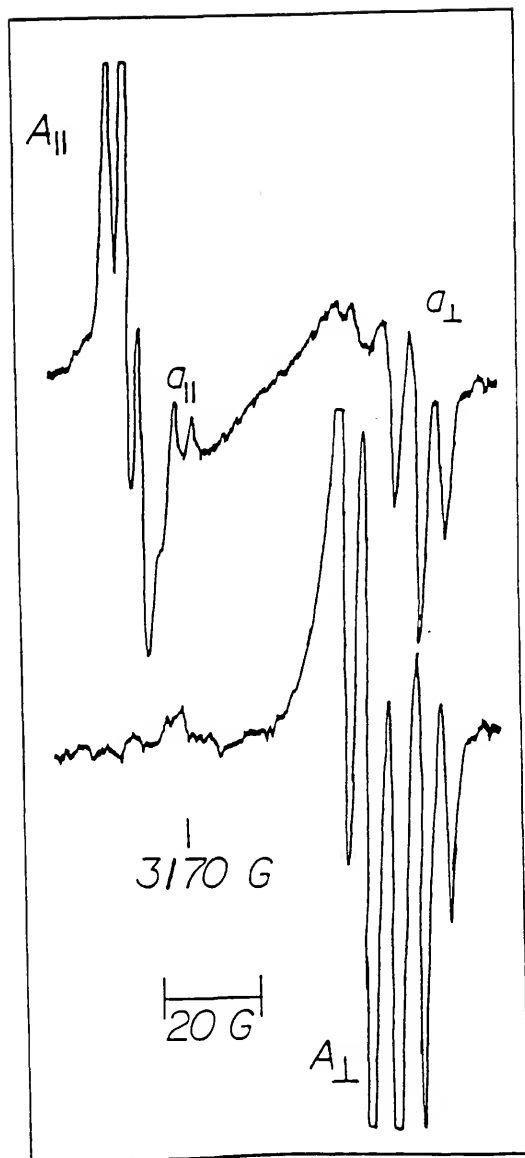


Figure IV-8. Same as Figure IV-6 except the  $m_I = 1/2$  transition is shown.

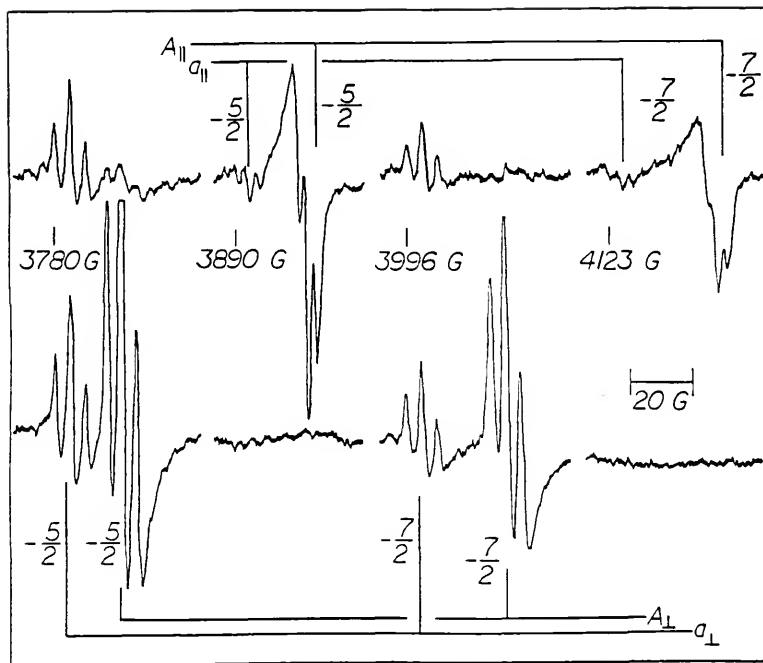


Figure IV-9. Same as Figure IV-6 except the  $m_I = -5/2$  and  $-7/2$  transitions are shown.

lines were directly observed.  $A_{\parallel}$  was fit indirectly by varying the parameters with  $\theta = 90$  degrees. This causes somewhat more uncertainty in  $A_{\parallel}$  than is found in either  $A_{\perp}$  or  $g_{\perp}$ .

It was found that  $g_{\perp}$  is equal to 1.9386 which is somewhat lower than  $g_e$ . This indicates that some spin-orbit coupling with a low lying excited state is probably occurring. The 5 G splitting which is observed between the doublets is consistent with what others have found for hydrogen attached to metal atoms (120).

#### $H_2ScSiH_n$

Two sets of eight triplets have been observed in these experiments. Both sets were fit using a 16 X 16 eigenvalue matrix which was diagonalized in order to fit the hyperfine parameters to the observed lines. The center line in each of the triplet patterns was used in the fitting routine since the observed triplet was most likely due to two equivalent hydrogens attached to a scandium. This is an acceptable approximation since the center of the triplet pattern should be close to where the transition would occur for the scandium hyperfine without any interaction due to the spin of the hydrogen nucleus. Both sets were fit to within 1 G of the observed (center) line positions (for those lines which were not obscured by other transitions or in the case of weak lines, specifically the (a) parallel lines, by the background noise).

For the most intense set of lines (A),  $g_{\perp}$  was found to be equal to 1.9695. Because a set of parallel lines was observed, it was possible to calculate  $g_{\parallel}$  independently from the perpendicular lines. The  $g_{\parallel}$  parameter was calculated by leaving  $A_{\perp}$  and  $A_{\parallel}$  unchanged from the calculation of  $g_{\perp}$ , but changing the value of  $\theta$  to 0 degrees. From this calculation  $g_{\parallel}$  was found to be equal to 1.9983. Assuming that  $A_{\perp}$  and  $A_{\parallel}$  were positive, we found  $A_{iso} = 557$  MHz and  $A_{dip} = 48$  MHz. The unpaired spin density  $\rho_S$  on the scandium was found to be 0.33.

That the majority of the molecules formed are so highly oriented is somewhat unusual. When a matrix is deposited, the trapped species are generally randomly oriented, and there is not such a dramatic change in the ESR spectrum when the rod is turned. But this type of trapping has been observed by other workers (13). Because of the large intensity of the orientation sensitive lines, it seems that the majority of the  $H_2ScSiH_n$  molecules are trapped with their axes perpendicular to the plane of the deposition surface. The lines are a bit broader than one would expect for a single type of trapping site. Also very weak perpendicular lines can be observed for only the strongest perpendicular lines when the rod is parallel to the pole faces of the magnet. This would seem to indicate that the molecules are trapped not exactly perpendicular to the surface but rather a

random selection of molecules would trace out a conical surface with the apex pointing toward the deposition surface.

The second set of eight triplets (a) would appear to belong to  $H_2ScSiH_n$  molecules which have been trapped out parallel to the deposition surface. This is indicated by the reduction of intensity of the perpendicular lines when the rod is turned and the weak appearance of the parallel lines. Both sets of lines show the characteristic triplet pattern one would expect for two equivalent hydrogen atoms. Because of this and since only parallel and perpendicular lines are observed, the molecule attains a pseudo linear configuration as far as the ESR was concerned.

Hydrogen containing scandium compounds have been studied previously by other workers (119,120). Both  $H_2Sc$  and  $Sc-H_2O$  have been reported by Knight and coworkers. Of interest is that  $Sc-H_2O$  can be observed by directly vaporizing scandium out of a tantalum cell as was found by Weltner and coworkers when they produced discandium (9). Adding that to the knowledge that scandium easily adsorbs water, it is possible that when scandium metal chips are vaporized not only scandium atoms make up the vapor composition, but also hydrated scandium atoms are present in the vapor. When this is mixed with hot silicon atoms, it is very possible that the hydrated scandium species become hydrogenated silicon-scandium species, as is observed in these experiments.

The other possibility in forming these hydrated scandium silicides is an insertion of a scandium atom into a silane like molecule. Several workers have reported this type of a mechanism for organic molecules, usually methane (121-126). Many first row transition metals have been reported to form an insertion product with methane. The activation of methane in a matrix has also been reported for group VI elements Al, Ga, and In (121). In the case of aluminum trapped in a methane matrix the insertion occurs at 10 K. If the matrix is photolyzed, the aluminum atom picks up a second hydrogen from a different methane molecule forming  $H_2AlCH_3$ . With at least two possible methods of forming hydrogen containing scandium silicides, we turn to the ESR spectra for help in determining what is happening in these experiments.

The exact structures of the two molecules is unclear. It is obvious from the experimental work that the molecules contain both silicon and scandium and the ESR spectrum presents a clear indication of how many hydrogens are attached to the scandium end of the molecule. What can not be determined is whether any hydrogens are attached to the silicon. For  $HScSiH_n$  we know that  $n$  cannot equal zero since that would result in either a singlet or triplet ground state for the molecule. The ESR spectra indicate that the molecule has a doublet ground state. This necessitates that  $n$  be odd. In all experiments involving silicon there is always present

in the ESR spectrum transitions due to  $\text{SiH}_3$ , which indicates the presence of silane (ESR invisible) in the matrix. With the knowledge that metal atoms can insert into methane, it seems reasonable that scandium could insert into a silane molecule. This would form  $\text{HScSiH}_3$  which is a doublet molecule.

The other set of observed lines are those of a molecule which contains one scandium atom, most likely a single silicon atom, and at least two hydrogen atoms attached to the scandium. We also know from the ESR spectrum that  $\text{H}_2\text{ScSiH}_n$  is a doublet molecule. This puts a limit on what values of  $n$  are valid. If  $n$  is odd, the molecule will have either a singlet or triplet ground state. In order for the molecule to have a doublet ground state  $n$  needs to be even or zero. This can be envisioned as occurring via two possible pathways. The simplest is a silicon reacting with a scandium attached to two hydrogen atoms to produce  $\text{H}_2\text{ScSi}$ . Even though this is an obvious method because of scandium's hydrophilic nature, no  $\text{H}_2\text{Sc}$  is observed in the spectrum, which means that the silicon has to be directly involved in the reaction process. Because  $\text{SiH}_3$  is present in the matrix, it is also possible that a scandium hydride molecule (ESR invisible) inserts into a  $\text{SiH}_3$  radical to form  $\text{H}_2\text{ScSiH}_2$ . Because  $\text{HSc}$  has a singlet ground state, it is impossible to determine if any is present in our matrices.



Determining the number of hydrogens attached to the silicon was not possible in these experiments since the natural abundance of  $^{29}\text{Si}$  ( $I=1/2$ ) is only about 4.5%, and therefore hyperfine splittings due to silicon were not observed. Unfortunately because of the presently exorbitant price of the silicon 29 isotope, we were not able to run any experiments with this isotope. This also made it impossible for us to rule out the possibility of more than one silicon in this molecule. In the experiments typically only a small amount of  $\text{Si}_2$  is observed. The intensity of the observed  $\text{Si}_2$  line in the experiments with both silicon and scandium was not significantly different when compared to the experiments where only silicon was deposited into an argon matrix at equivalent deposition temperatures. This seems to indicate that a species containing scandium and two or more silicones is very unlikely.

## CHAPTER V CONCLUSION

Matrix isolation has been utilized along with two spectroscopic techniques to establish the electronic ground states as well as the structures of a variety of metal carbonyls and metal clusters. The ground state of VCO was found to be  $^6\Sigma$ . This means that the molecule contained five unpaired electrons. Since the ground state of vanadium contains only three unpaired d electrons it became obvious that in order to form the monocarbonyl, promotion of an s electron into a d orbital was necessary. Even though this bit of information was mute in the study of CrCO, it became important when analyzing the negative results of the MnCO studies.

From the literature it seemed obvious that these types of molecules could be produced for all of the first row transition metals (91). That MnCO could not be observed in either ESR or FTIR was therefore thought at first to be an anomaly of the experiment. Other workers had made tentative assignments in the IR for the molecule (92). Upon closer examination the assigned stretching frequency for CrCO proved wrong by over  $100\text{ cm}^{-1}$  and the assignment for MnCO could not

be reproduced under a large variety of experimental conditions. What became obvious from our experimental work was that  $\text{Mn}_x\text{CO}$  was rather easily formed. Upon analyzing the ESR data from the VCO experiments it became obvious why  $\text{MnCO}$  could not be produced under our experimental conditions. Promotion of one of the 4s electrons in manganese into a d orbital was not possible because of the promotion energy (over  $22,000\text{cm}^{-1}$ ). Combining the negative results obtained from the  $\text{MnCO}$  experiments with the information obtained from the ESR experiments with VCO, allowed development of a reasonable explanation of how the monocarbonyls for the first row transition metals were formed. The explanation is reasonable in that it fits in well with the known properties of these metals, and further experimental evidence provided by other researchers confirms our hypothesis.

A major reason for attempting to gain an understanding of the bonding of metal carbonyls is the light such work may shed on catalysis. Many catalytic systems contain metals bound to carbonyls. We know that these species aid in reducing the activation energy of many types of reactions but unfortunately very little is known about the bonding of these molecules. With work such as this, a fundamental understanding has been gained of the interactions between the metal and the carbonyl.

Metal clusters are also thought to be important in catalytic activity. Again, many metal clusters are known to

have catalytic activity but a fundamental understanding of what is occurring on a molecular level is lacking. Studying silver clusters seemed to be an obvious choice because of the variety of its applications in chemistry, its ease of vaporization (about 1200 °C), its low nuclear spin ( $S=1/2$ ), and the availability of the 109 isotope of silver (with reasonable purity and at a reasonable cost).

We were able to isolate and identify a silver cluster containing seven atoms. From the ESR spectrum it was possible to determine both the ground state ( $^2\Sigma$ ) of the cluster as well as the structure (pentagonal bipyramidal) of the molecule. It had been thought that metals which contained an unpaired s electron with the remainder of the orbitals either completely empty or completely filled (such as the Group IA and Group IB metals) should have similar properties (97-105). Our study of the silver septamer gave results that correlated well with those found for the septamers of several Group IA metals. A pentamer for silver had been reported in the literature but no pentamers for any of the Group IA metals have been observed. Upon closer examination of the ESR data it became apparent that the reported pentamer was actually the septamer. This was shown by comparison of the hyperfine parameters and spin densities determined for  $\text{Ag}_7$  and those reported for the pentamer.

It is somewhat strange that only the silver septamer was observed in our experimental work. One would have

expected the smaller clusters of silver to be present also. We found that  $\text{Ag}_7$  was formed only after annealing the matrix. It remained even after the matrix had been strongly annealed (close to the melting point of the matrix). This shows that we were dealing with a very stable molecule. It is possible that the other clusters were simply not stable enough to be trapped in the neon matrix. The transitions due to the smaller clusters may also have been obscured by the very intense lines due to silver atoms (which disappear after annealing the matrix) or by transitions due to impurities in the matrix such as  $\text{CH}_3$ .

Since  $\text{Ag}_7$  was not observed immediately after the matrix had been deposited, it was reasonable to assume that it was not formed during the vaporization of the metal. Strong signals due to silver atoms were however observed. It was therefore assumed that the vapor consists predominantly of atoms and possibly a few dimers (which are ESR invisible). The nucleation in this case seemed to occur not in the vapor but rather in the condensed phase of the matrix. And after the matrix had been annealed several times only the most stable molecule(s) survived. In this case it was  $\text{Ag}_7$ .

Further work was done with silver and with first row transition metals codepositing them with silicon in order to form clusters. This proved successful in only two cases,  $\text{MnSi}$  and  $\text{AgSi}$ . We had some success with scandium forming hydrogen containing silicon-scandium clusters. The problems

encountered with this work exemplifies exactly how little cluster formation is understood. In situations where the carbide had been formed (115) we were not able to form the silicide, even though the properties of carbon and silicon should be similar since they are both Group IVA elements. It became apparent that this was not the case. Why other species were not observed is difficult to ascertain. It is possible that there were clusters formed but their ground states were such that they were not observable via ESR spectroscopy. We were able to isolate AgSi and determine that the molecule has a  $^2\Sigma$  ground state which indicates that there is a single bond between the silver and the silicon. In experiments where manganese and silicon were codeposited manganese hyperfine was observed and assigned to MnSi which was found to have a  $^4\Sigma$  ground state. This indicated that the species was doubly bonded.

For scandium, clusters were observed that also contained hydrogen. Whether a bare scandium-silicon molecule is possible is unclear. What we were able to determine was the number of hydrogens on the scandium from the splitting on the scandium hyperfine lines. The ground states of these molecules have also been determined. Both were found to be  $^2\Sigma$  molecules. One had a single hydrogen attached to the scandium and the other molecule had two hydrogens attached to the scandium end of the molecule.

From these experiments we were able to determine the structures and ground states of several metal carbonyls and metal clusters. In isolating and indentifying these species we have been able to further our understanding of small metal containing molecules as well as correct previous misconceptions. We have been able to develop a basic understanding of how the first row transition metal monocarbonyls are formed. We were also able to add to the growing body of evidence that supports the theory that the properties of the alkali metals are similar to the coinage metals, substantiating the belief that a closed shell of electrons can be considered as an empty shell would be, thus simplifying theoretical calculations on larger molecular systems. With this work we have laid the ground work for studies in several areas. The other coinage metals, copper and gold need to be investigated to see if they also conform to the theory. We were able to finally explain why certain metal carbonyls of the first row transtion metals can not be observed. This work needs to be pushed on so as to encompass the other transition metals (second and third row) even though the difficulties in vaporizing these metals can be considerable.

# REFERENCES

1. E. Whittle, D. A. Dows, and G. C. Pimentel, J. Chem. Phys., 22, 1943 (1954).
2. Discussion with W. Weltner, Jr., and R. J. Van Zee.
3. S. Mitchell and G. A. Ozin, J. Amer. Chem. Soc., 100, 6776 (1978).
4. M. Moskovits, D. P. DiLella, A. C. S. Symp. Ser. 179.
5. K. J. Zeringue, J. ShakhEmampour, J. C. Rivoal, and M. Vala, J. Chem. Phys. 78, 2231 (1983); R. S. Drago, "Physical Methods in Chemistry," W. B. Saunders Co., Philadelphia, 1977.
6. K. Jansson and R. Scullman, J. Mole. Spectrosc., 61, 299 (1976).
7. W. C. Easley and W. Weltner, Jr., J. Chem. Phys., 52, 197 (1970).
8. W. R. M. Graham, K. I. Dismuke, and W. Weltner, Jr., Astrophys. J., 204, 301 (1976).
9. L. B. Knight, Jr., R. J. Van Zee, W. Weltner, Jr., Chem. Phys. Lett. 94, 296 (1983).
10. M. Moskovits, D. P. DiLella, V. Limm, J. Chem. Phys., 80, 626 (1984).
11. W. Weltner, Jr., R. J. Van Zee, Ann. Rev. Phys. Chem., 291-327 (1984).
12. P. R. R. Langridge-Smith, M. D. Morse, G. P. Hansen, R. E. Smalley, A. J. Merer, J. Chem. Phys., 80, 593 (1984).
13. C. A. Baumann, R. J. Van Zee, S. V. Bhat, W. Weltner, Jr., J. Chem. Phys. 78, 190 (1983).



14. L. B. Knight, Jr., R. W. Woodward, R. J. Van Zee, W. Weltner, Jr., J. Chem. Phys. 79, 5820 (1983).
15. J. Bernholc, J. C. Phillips, J. Chem. Phys., 85, 3258 (1986).
16. R. M. Ziff, E. D. McGrady, P. Meakin, J. Chem. Phys., 82, 5269 (1985).
17. G. W. Mulholland, R. D. Mountain, J. Chem. Phys., 84, 4109 (1986).
18. J. Bernholc, J. C. Phillips, Phys. Rev. B, 33, 7395 (1986).
19. J. Diefenbach, T. P. Martin, J. Chem. Phys., 83, 4585 (1985).
20. M. E. Geusic, M. D. Morse, S. C. O'Brien, R. E. Smalley, Rev. Sci. Instrum., 56, 2123 (1985).
21. L. A. Bloomfield, M. E. Geusic, R. R. Freeman, W. L. Brown, Chem. Phys. Lett., 121, 33 (1985).
22. M. V. Smoluchowski, Z. Phys. Chem., 92, 129 (1917).
23. H. W. Kroto, J. R. Heath, S. C. O'Brien, R. F. Curl, R. E. Smalley, Nature, 318, 162 (1985).
24. W. Weltner, Jr., "Magnetic Atoms and Molecules," Van Nostrand Reinhold Co. Inc., New York, 1983.
25. A. Carrington and A. D. McLachlan, "Introduction to Magnetic Resonance," Harper and Row, New York, 1967.
26. A. Abragam and B. Bleaney, "Electron Paramagnetic Resonance of Transition Ions," Dover Publications, Inc., New York, 1980.
27. J. E. Wertz and J. R. Bolton, "Electron Spin Resonance: Elementary Theory and Practical Applications," McGraw-Hill, New York, 1972.
28. R. F. Ferrante, Ph.D. Thesis, University of Florida, 1977.
29. K. I. Dismuke, Ph.D. Thesis, University of Florida, 1975.
30. K. D. Bowers and J. Owen, Reports Progr. Phys., 18, 304 (1955).

31. R. L. Morehouse, J. J. Christiansen, W. Gordy, J. Chem. Phys., 45, 1747 (1966).
32. A. Abragam and M. H. L. Pryce, Proc. Roy. Soc., 205A, 135 (1951).
33. E. Fermi, Z. Physik, 60, 320 (1930).
34. E. Wasserman, L. Barash, and W. A. Yager, J. Am. Chem. Soc., 87, 2075 (1965).
35. B. Bleaney, Proc. Phys. Soc. (London), A63, 407, (1950).
36. B. Bleaney, Phil. Mag., 42, 441 (1951).
37. R. H. Sands, Phys. Rev., 99, 1222 (1955).
38. J. W. Searl, R. C. Smith, and S. J. Wyard, Proc. Phys. Soc., 74, 491 (1959).
39. B. Bleaney, Proc. Phys. Soc., A75, 621 (1960).
40. F. K. Kneubuhl, J. Chem. Phys., 33, 1074 (1960).
41. J. A. Ibers and J. D. Swalen, Phys. Rev., 127, 1914 (1962).
42. L. B. Knight, Jr., W. C. Easley, and W. Weltner, Jr., J. Chem. Phys., 54, 1610 (1971).
43. W. Low, "Paramagnetic Resonance in Solids, Supplement 2," Academic, New York (1960).
44. L. D. Rollman and S. I. Chan, J. Chem. Phys., 50, 3416 (1969).
45. L. S. Singer, J. Chem. Phys., 23, 379 (1955).
46. P. H. Kasai, J. Chem. Phys., 49, 4979 (1968).
47. J. M. Brom, C. H. Durham, Jr., and W. Weltner, Jr., J. Chem. Phys., 61, 970 (1974).
48. R. Aasa, J. Chem. Phys., 52, 3919 (1970).
49. W. V. Sweeney, D. Coucouvanis, and R. E. Coffman, J. Chem. Phys., 59, 369 (1973).
50. R. D. Dowsing and J. F. Gibson, J. Chem. Phys., 50, 294 (1969).

51. Ira N. Levine, "Molecular Spectroscopy," John Wiley and Sons, New York, 1975.
52. Milton Orchin and H.H. Jaffe, "Symmetry, Orbitals, and Spectra," Wiley-Interscience, New York, 1971.
53. William A. Guillory, "Introduction to Molecular Spectroscopy," Allyn and Bacon, Inc., Boston, 1977.
54. E. B. Wilson, J. C. Decius, and P. C. Cross, "Molecular Vibrations," McGraw-Hill, New York, 1955.
55. J. R. Morton and K. F. Preston, Organometallics, 3, 1386 (1984).
56. D. W. Pratt and R. J. Myers, J. Am. Chem. Soc., 89, 6470 (1967).
57. K. A. Robinson, J. Am. Chem. Soc., 98, 5188 (1976).
58. M. P. Boyer, Y. LePage, J. R. Morton, K. F. Preston, and M. J. Vuolle, Can. J. Spectrosc., 26, 181 (1981).
59. S. W. Bratt, A. Kassyk, R. N. Perutz, and M. C. R. Symons, J. Am. Chem. Soc., 104, 490 (1982).
60. J. A. Howard, J. R. Morton, and K. F. Preston, Chem. Phys. Lett., 83, 226 (1981).
61. L. A. Hanlan, H. Huber, E. P. Kuendig, B. R. McGarvey, and G. A. Ozin, J. Am. Chem. Soc., 97, 7054 (1975).
62. S. A. Fairhurst, J. R. Morton, and K. F. Preston, J. Magn. Reson., 55, 453 (1983).
63. G. A. Ozin, Appl. Spectrosc., 30, 573 (1976).
64. P. H. Kasai and P. M. Jones, J. Am. Chem. Soc., 107, 813 (1985).
65. D. McIntosh and G. A. Ozin, J. Am. Chem. Soc., 98, 3167 (1976).
66. P. H. Kasai and P. M. Jones, J. Phys. Chem., 89, 1147 (1985).

67. T. Lionel, J. R. Morton, and K. F. Preston, J. Chem. Phys., 76, 234 (1982).
68. S. A. Fairhurst, J. R. Morton, and K. F. Preston, Chem. Phys. Lett., 104, 112 (1984).
69. S. F. A. Kettle, J. Chem. Soc. A, 420 (1966); Inorg. Chem. 4, 1661 (1965).
70. R. L. DeKock, Inorg. Chem., 10, 1205 (1971).
71. J. K. Burdett, J. Chem. Soc., Faraday Trans. 2, 70, 1599 (1974).
72. J. K. Burdett, Inorg. Chem., 14, 375 (1975).
73. M. Elian and R. Hoffmann, Inorg. Chem., 14, 1058 (1975).
74. L. Hanlan, H. Huber, and G. A. Ozin, Inorg. Chem., 15, 2592 (1976).
75. H. J. Keller, P. Laubereau, D. Nothe, Z. Naturforsch. B, 24, 257 (1969); H. Haas and R. K. Sheline, J. Am. Chem. Soc., 88, 3219 (1966).
76. T. J. Barton, R. Grinter, and A. J. Thomson, J. Chem. Soc., Dalton Trans., 698 (1978).
77. G. F. Holland, M. C. Manning, D. E. Ellis, and W. C. Trogler, J. Am. Chem. Soc., 105, 2308 (1983).
78. D. G. Schmidding, J. Mol. Struct., 24, 1 (1975); S. Bellard, K. A. Robinson, and G. M. Sheldrick, Acta Crystallogr., Sect. B, 35, 271 (1979).
79. R. J. Van Zee, C. A. Baumann, and W. Weltner, Jr., J. Chem. Phys., 82, 3912 (1985).
80. See ref. 24 for a discussion of the spin Hamiltonian, zero field splitting parameters, and basic references.
81. R. J. Van Zee, R. F. Ferrante, K. J. Zeringue, and W. Weltner, Jr., J. Chem Phys., 75, 5297 (1981).

82. R. L. Belford and M. J. Nilges, "Computer Simulation of Powder Spectra," EPR Symposium, 21st Rocky Mountain Conference, Denver, CO, Aug, 1979; M. J. Nilges, Ph.D. Thesis, University of Illinois, 1981; T. E. Altman, Ph.D. Thesis, University of Illinois, 1981; A. M. Maurice, Ph.D. Thesis, University of Illinois, 1982; E. P. Duliba, Ph.D. Thesis, University of Illinois, 1983.
83. C. E. Moore, Natl. Bur. Stand. Circ., No. 467, (1949).
84. R. L. DeKock and H. B. Gray, "Chemical Structure and Bonding," Benjamin/Cummings, Menlo Park, CA, 1980, Figure 5-43, p 329.
85. J. R. Morton and K. F. Preston, J. Mag. Reson., 30, 577 (1978).
86. B. R. McGarvey, "Transition Metal Chemistry," Vol. 3, Marcel Dekker, New York, 1966, p 118.
87. T. M. Dunn, Trans. Faraday Soc., 57, 1441 (1961).
88. See ref. 86, p 182.
89. P. H. Kasai, E. B. Whipple, and W. Weltner, Jr., J. Chem. Phys., 44, 2581 (1966).
90. H. H. Tippins, Phys. Rev., 160, 343 (1967).
91. see S. B. H. Bach, C. A. Taylor, R. J. Van Zee, M. T. Vala, and W. Weltner, Jr., J. Am. Chem. Soc., 108, 7104 (1986), ref. 1; L. Brewer and J.S. Winn, Faraday Symp. Chem. Soc., 14, 126 (1980).
92. G. A. Ozin, A. Van der Voet, Prog. Inorg. Chem., 19, 137 (1975).
93. H. Huber, E. P. Kundig, G. A. Ozin, A. J. Poe, J. Am. Chem. Soc., 97, 308 (1975).
94. R. J. Van Zee, S. B. H. Bach, W. Weltner, Jr., J. Phys. Chem., 90, 583 (1986).
95. D. M. Lindsay, D. R. Herschbach, and A. L. Kwiram, Mol. Phys., 32, 1199 (1976); D. M. Lindsay, and G. A. Thompson, J. Chem. Phys., 77, 1114 (1982); G. A. Thompson, and D. M. Lindsay, *ibid*, 74, 959 (1981); D. A. Garland, and D. M. Lindsay, *ibid*, 78, 2813 (1983).

96. G. A. Thompson, F. Tischler, and D. M. Lindsay, *J. Chem. Phys.*, 78, 5946 (1983); D. A. Garland, and D. M. Lindsay, *ibid*, 80, 4761 (1984).
97. W. H. Gerber, and E. Schumacher, *J. Chem. Phys.*, 69, 1692 (1978); R. L. Martin, and E. R. Davidson, *Mol. Phys.*, 35, 1713 (1978); J. Flad, H. Stoll, and H. Preuss, *J. Chem. Phys.*, 71, 3042 (1979); P. Fantucci, J. Koucky, and G. Pacchiono, *ibid*, 80, 325 (1984); J. L. Martins, J. Buttet, and R. Car, *Phys. Rev. B*, 31, 1804 (1985).
98. W. Weltner, Jr., and R. J. Van Zee, "The Physics and Chemistry of Small Clusters," edited by P. Jena, B. K. Rao, and S. N. Khanna, Plenum, New York, 1987.
99. See, J. A. Howard, R. Sutcliffe, and B. Mile, *Surf. Sci.*, 156, 214 (1985) for a review.
100. J. A. Howard, K. F. Preston, R. Sutcliffe, and B. Mile, *J. Phys. Chem.*, 87, 536 (1983); J. A. Howard, K. F. Preston, and B. Mile, *J. Am. Chem. Soc.*, 103, 6226 (1981); J. A. Howard, R. Sutcliffe, and B. Mile, *J. Chem. Soc. Chem. Commun.*, 1149 (1983).
101.  $\text{Ag}_3$  is presumably distorted to an acute triangular structure in a solid nitrogen matrix [K. Kernisant, G. A. Thompson, and D. A. Lindsay, *J. Chem. Phys.*, 82, 4739 (1985)].
102. J. A. Howard, R. Sutcliffe, J. S. Tse, and B. Mile, *Chem. Phys. Lett.*, 94, 561 (1983); J. A. Howard, R. Sutcliffe, and B. Mile, *J. Phys. Chem.*, 88, 2183 (1984).
103. J. A. Howard, R. Sutcliffe, and B. Mile, *J. Phys. Chem.*, 87, 2268 (1983).
104. R. Arratia-Perez, and G. L. Malli, *J. Chem. Phys.*, 85, 6610 (1986).
105. S. Ino, *J. Phys. Soc. Jpn.*, 21, 346 (1966); 27, 941 (1969).

106. See, for example, R. Monot, "Physical Latent Image Formation of Silver Halides," edited by A. Balderschi, World Science, Singapore, 1984, pp. 175-94; L. D. Marks, Surf. Sci. 150, 302 (1985), and references given therein, such as J. Buttet and J. P. Borel, Helv. Phys. Acta., 56, 541 (1983); C. Solliard and M. Flueli, Surf. Sci., 156, 487 (1985).
107. P. H. Kasai, and D. McLeod, Jr., J. Chem. Phys., 55, 1566 (1971).
108. R. W. Fessenden, J. Chem. Phys., 37, 747 (1962).
109. Y. Wang, T. F. George, D. M. Lindsay, and A. C. Beri, J. Chem. Phys., 86, 3493 (1987); D. M. Lindsay, Y. Wang, and T. F. George, ibid, 86, 3500 (1987).
110. We are neglecting any Jahn-Teller distortion which such an orbitally degenerate  $^2E$  state can be expected to experience.
111. D. M. Lindsay, (work in progress).
112. See ref. 24, p. 49.
113. R. R. Lembke, R. F. Ferrante, and W. Weltner, Jr., J. Am. Chem. Soc., 99, 416 (1977).
114. R. J. Van Zee, R. F. Ferrante, and W. Weltner, Jr., J. Chem. Phys., 83, 6181 (1985.)
115. R. J. Van Zee, J. J. Bianchini, and W. Weltner, Jr., Chem. Phys. Lett., 127, 314 (1986).
116. R. F. Ferrante, J. L. Wilkerson, W. R. M. Graham, and W. Weltner, Jr., J. Chem. Phys., 67, 5904 (1977).
117. R. J. Van Zee, C. M. Brown, and W. Weltner, Jr., Accounts Chem. Res., 13, 237 (1980).
118. G. W. Ludwig and H. H. Woodbury, "Solid State Physics," Ed. F. Sietz and D. Turnbull, Academic Press, New York, 1962. Vol. 13, pg. 223.
119. L. B. Knight, Jr., to be published (1983).
120. L. B. Knight, Jr., M.B. Wise, T. A. Fisher, J. Steadman, J. Chem. Phys., 74, 6636 (1981).

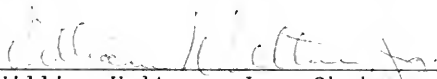
121. K. J. Klabunde and Yasutaka Tanaka, J. Am. Chem. Soc., 105, 3544 (1983).
122. J. G. McCaffrey, J. M. Parnis, G. A. Ozin, and W. H. Breckenridge, J. Phys. Chem., 89, 4945 (1985).
123. J. G. McCaffrey, R. A. Poirier, G. A. Ozin, and I. G. Csizmadia, J. Phys. Chem., 88, 2898 (1984).
124. G. A. Ozin, D. F. McIntosh, and S. A. Mitchell, J. Am. Chem. Soc., 103, 1574 (1984).
125. G. A. Ozin and J. G. McCaffrey, J. Am. Chem. Soc., 104, 1551 (1982).
126. N. J. Turro, Ming-Fea Chow, Chao-Jen Cheung, Chen-Ho Tung, J. Am. Chem. So., 102, 7393 (1980).



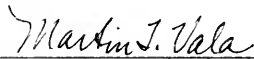
#### BIOGRAPHICAL SKETCH

Stephan Bach was born on November 4, 1959, in Knoxville, Tenn., to Dr. and Mrs. Bernd B. Bach. He graduated with Honors from Anderson High School in Cincinnati, Ohio, in June of 1977. In June of 1983 he graduated from the University of Cincinnati having earned a Bachelor of Science in chemistry, Bachelor of Arts in German literature, and a Certificate in Business Administration. Since August of 1983 he has attended the University of Florida pursuing a course of study leading to a Doctor of Philosophy degree in chemistry.

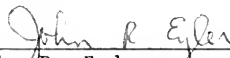
I certify that I have read this study and that in my opinion it conforms to acceptable standards of scholarly presentation and is fully adequate, in scope and quality, as a dissertation for the degree of Doctor of Philosophy.

  
\_\_\_\_\_  
William Weltner, Jr., Chairman  
Professor of Chemistry

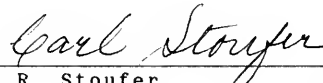
I certify that I have read this study and that in my opinion it conforms to acceptable standards of scholarly presentation and is fully adequate, in scope and quality, as a dissertation for the degree of Doctor of Philosophy.

  
\_\_\_\_\_  
Martin T. Vala  
Professor of Chemistry


I certify that I have read this study and that in my opinion it conforms to acceptable standards of scholarly presentation and is fully adequate, in scope and quality, as a dissertation for the degree of Doctor of Philosophy.

  
\_\_\_\_\_  
John R. Eyler  
Professor of Chemistry

I certify that I have read this study and that in my opinion it conforms to acceptable standards of scholarly presentation and is fully adequate, in scope and quality, as a dissertation for the degree of Doctor of Philosophy.

  
\_\_\_\_\_  
Carl R. Stoufer  
Associate Professor of Chemistry

I certify that I have read this study and that in my opinion it conforms to acceptable standards of scholarly presentation and is fully adequate, in scope and quality, as a dissertation for the degree of Doctor of Philosophy.

  
\_\_\_\_\_  
Jerry W. Williams  
Assistant Professor of Materials  
Science and Engineering

This dissertation was submitted to the Graduate Faculty of the Department of Chemistry in the College of Liberal Arts and Sciences and to Graduate School and was accepted as partial fulfillment of the requirements for the degree of Doctor of Philosophy.

December, 1987

\_\_\_\_\_  
Dean, Graduate School

UNIVERSITY OF FLORIDA



3 1262 08553 5473